

2023
December

Research And
Evaluations In
ENGINEERING

EDITORS

Doç. Dr. Vedat ÇAVUŞ

İmtiyaz Sahibi • Yaşar Hız
Genel Yayın Yönetmeni • Eda Altunel
Yayına Hazırlayan • Gece Kitaplığı
Editörler • Doç. Dr. Vedat ÇAVUŞ

Birinci Basım • Aralık 2023 / ANKARA

ISBN • 978-625-425-416-1

© copyright

Bu kitabın yayın hakkı Gece Kitaplığı'na aittir.
Kaynak gösterilmeden alıntı yapılamaz, izin almadan
hiçbir yolla çoğaltılamaz.

Gece Kitaplığı

Adres: Kızılay Mah. Fevzi Çakmak 1. Sokak Ümit Apt

No: 22/A Çankaya/ANKARA Tel: 0312 384 80 40

www.gecekitapligi.com
gecekitapligi@gmail.com

Baskı & Cilt
Bizim Buro
Sertifika No: 42488

Research And Evaluations In Engineering

December 2023

Editors:
Doç. Dr. Vedat ÇAVUŞ

CONTENTS

CHAPTER 1

STRESS ANALYSIS WITH FINITE ELEMENT METHOD IN THE AXLE OF SINGLE AXLE AGRICULTURAL CARTS

Sümeyye ERDEM, Yusuf DİLAY.....1

CHAPTER 2

DYNAMIC RISK MANAGEMENT IN THE PRIVATE SECTOR: A VBA-ENABLED L-TYPE MATRIX APPROACH

Zehra GÜLTEN YALÇIN, M. Bora AKIN, Mustafa DAĞ.....17

CHAPTER 3

DERIVATION OF COX-VOINOV EQUATION ANALITICALLY FOR THIN LIQUID FILM ON A FLAT SUBSTRATE

Ashı TİKTAŞ.....37

CHAPTER 4

3D MODELING AND SIMULATION OF A RELUCTANCE COIL GUN

Vekil SARI.....55

CHAPTER 5

BANANA FIBER

Suat CANOĞLU, Ayberk ŞİT.....75

CHAPTER 6

PRINT CIRCUIT

Damla SAĞLAM, Sevcan AYTAÇ.....89

CHAPTER 7

**A PRECISION LANDING STUDY ON VERTICAL LANDING
ROCKET WITH NEEDLE-VALVE COLD GAS PROPELLANT
SYSTEM**

Onur DUMAN, Engin DEMİRİYAY,

Umutcan BİLER, Arzum İŞİTAN..... 97

CHAPTER 8

**RECENT TRENDS IN ADDITIVE MANUFACTURING OF
CARBON REINFORCED POLYMER COMPOSITES**

Tuba ÖZDEMİR ÖGE, Mecit ÖGE, Firdevs Banu ÖZDEMİR..... 123

CHAPTER 9

**3D SURFACE PROFILOME TRY AND ITS APPLICATION IN
TRIBOLOGICAL STUDIES**

Tuba ÖZDEMİR ÖGE, Mecit ÖGE, Firdevs Banu ÖZDEMİR..... 135

CHAPTER 10

**ENHANCING CUSTOMER SATISFACTION AND COST
EFFICIENCY: A VALUE ENGINEERING APPROACH TO
IMPROVING THE CHAIR MANUFACTURING PROCESS**

Seymen ÇİFTÇİ, Abdullah Cemil ILCE, Kadir ÖZKAYA..... 147

CHAPTER 11

**SURROGATE MODEL ASSISTED OPTIMIZATION OF
MULTIBAND ANTENNA**

Mehmet Ali BELEN 163



STRESS ANALYSIS WITH FINITE ELEMENT METHOD IN THE AXLE OF SINGLE AXLE AGRICULTURAL CARTS

Sümeyye ERDEM¹
Yusuf DİLAY²

1 Öğr. Gör., Karamanoğlu Mehmetbey Üniversitesi, Teknik Bilimler
Meslek Yüksekokulu, <http://orcid.org/0000-0002-5518-2716>

2 Dr. Öğr. Üyesi, Karamanoğlu Mehmetbey Üniversitesi, Teknik Bilimler
Meslek Yüksekokulu, <http://orcid.org/0000-0002-5365-5137>

INTRODUCTION

Tractor-drawn agricultural carts are indispensable at every stage of agricultural production. They can be single-axle or 2-axle. Single axle agricultural carts are more preferred in mountainous or hilly regions (Acar et al., 2011). The drawbar of single axle agricultural carts is subjected to both tensile and bending stresses. When analyzed under static and dynamic conditions, there is weight transfer to the rear axle of the tractor (Akinci, 1994; Korucu et al., 2003). This increases the dynamic rear axle load of the tractor and changes the towing performance positively. The maximum load capacity of two-axle agricultural carts is higher than single axle ones. They are mostly preferred in non-mountainous regions. In the connection of the tractor to the drawbar, the axle can be forced by the towing force in the axial direction to a large extent. The most critical cross-section for axial or angled towing forces is the wall cross-section corresponding to the centre of the joint hole in the direction perpendicular to the towing direction (Zeytinoğlu, 2006). In this study, the stresses occurring in the axle of a 4-ton, single axle agricultural cart were analyzed by finite element method (Anonymous, 1998). Since the axle considered in the study has square and circular cross-section, it was analyzed separately. In the study, in addition to the axial pulling force, the vertical forces on the tractor's towing ring caused by the agricultural cart load were also taken into account according to the single axle agricultural cart feature. Tensile and shear stresses and safety coefficients were calculated at the critical sections of the axle according to both external forces as axial pulling and vertical reaction forces. In addition, the tensile energy of the axle with circular and square sections and the safety factor due to fatigue of the material were also determined. At the end of the study, analyses were performed and recommendations were made on axle sizing and material selection.

MATERIALS AND METHODS

The research material of the study consists of a circular and rectangular axle used in agricultural carts. The technical dimensions of the solid modelling of the analyzed axle prepared using SolidWorks program are given in Figure 1-2. Structural steel was used as the axle material. Some technical properties of the material are given in Table 1.

Table 1. Axle material properties

Axle (Structural Steel)	Properties
Modulus of Elasticity	200 GPa
Yield Strength	250 MPa
Poisson Ratio	0,3
Density	7850 kg/m ³
Tensile Strength	460 MPa



Figure 1. Technical drawing of circular cross-section axle



Figure 2. Technical drawing of square section axle

The axle parts were modelled in three dimensions using SolidWorks solid model software (Figure 3-4). Then, the stress distributions occurring on the axle were simulated using the finite element package software Ansys Workbench under different loads and operating environments. During the stress analyses, the axle was modelled with all dimensions in order to get as close as possible to the real working environment. Analyses were performed as three-dimensional linear static. The stress analysis results obtained are given as outputs of Ansys Workbench package software. The axle operation was evaluated and simulated for the application conditions.

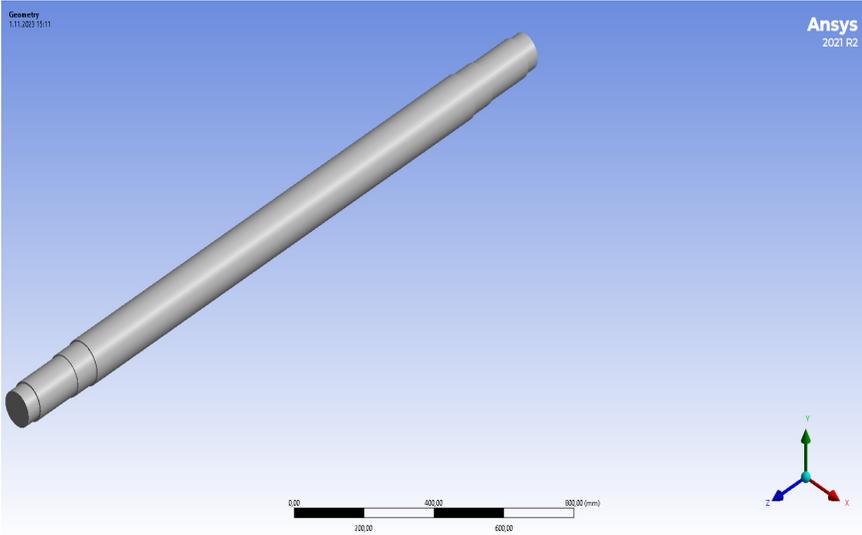


Figure 3. Solid model drawing of circular cross-section axle

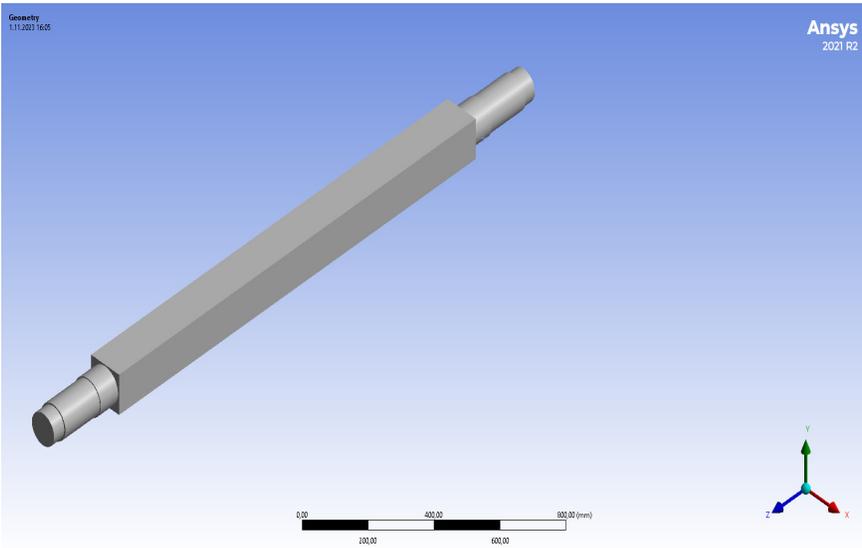


Figure 4. Solid model drawing of a square cross-section axle

In the first step of the analysis process carried out in the simulation environment with the finite element method, meshing of the axle model, in other words, separation of the model into the most appropriate small parts, was performed (Figure 5-6). The meshing is shown in Figure 5 and Figure 6. In the creation of the finite element structure of the axle, the “meshing” functions of Ansys Workbench software were utilized. Then, the element type is determined in the method section. In other words, the

mesh structures to be applied (automatic, tetrahedrons, hex dominant, sweep, multizone, cartezian, etc.) are selected. Mesh density can be increased or decreased. As well as the whole geometry, certain regions can be meshed with different densities by selecting surfaces, lines and points on the geometry. For the axle with circular cross-section, 904,884 total number of elements and 1,252,882 total number of nodes were obtained. For the axis with square cross-section, 1,095,892 total number of elements and 1,513,880 total number of nodes were obtained.

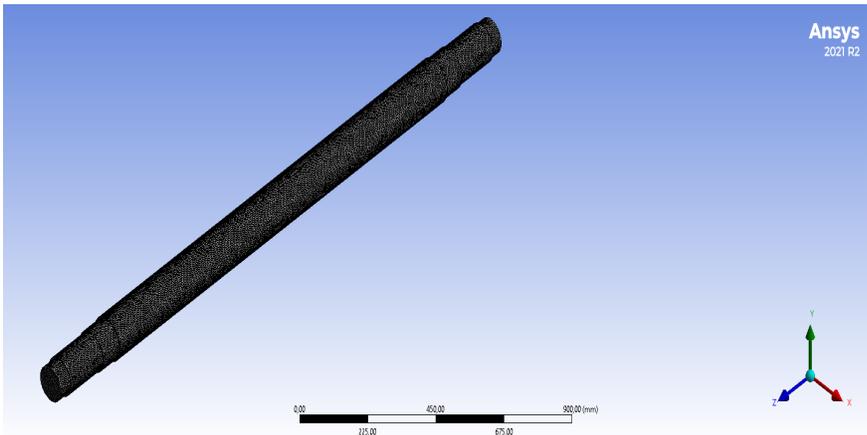


Figure 5. Finite element structure of the circular cross-section axle model

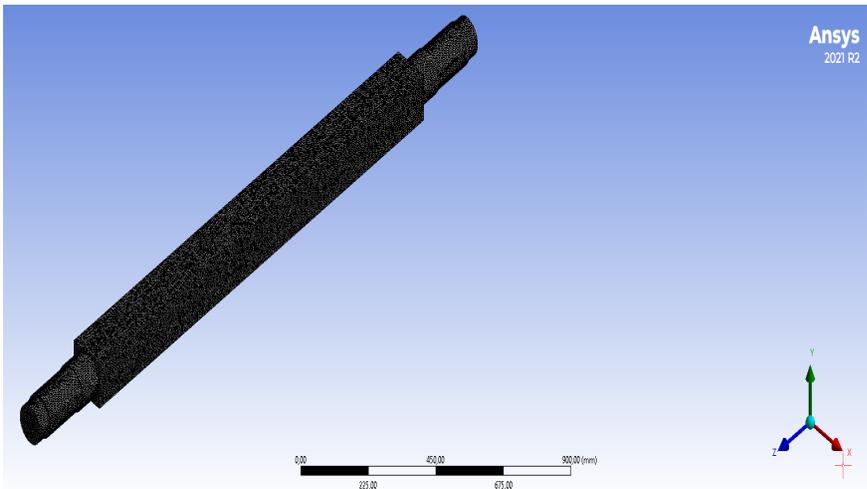


Figure 6. Finite element structure of the square section axle model

The load diagram of the agricultural cart axle is shown in Figure 7.

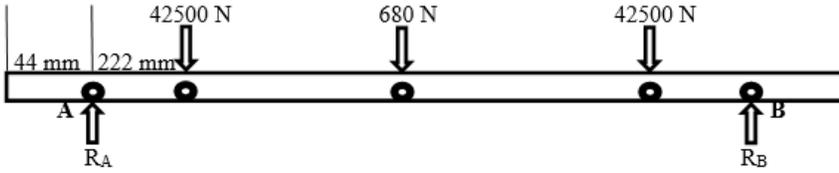


Figure 7. Load diagram of the axle (Terzi et al., 2021).

Figure 8 shows the load diagram applied to the circular cross-section axle. On the surface shown in red, a load of 680 N is applied to point A and 42,500 N is applied to points B and C. Point D, shown in purple, is the fixed support point.

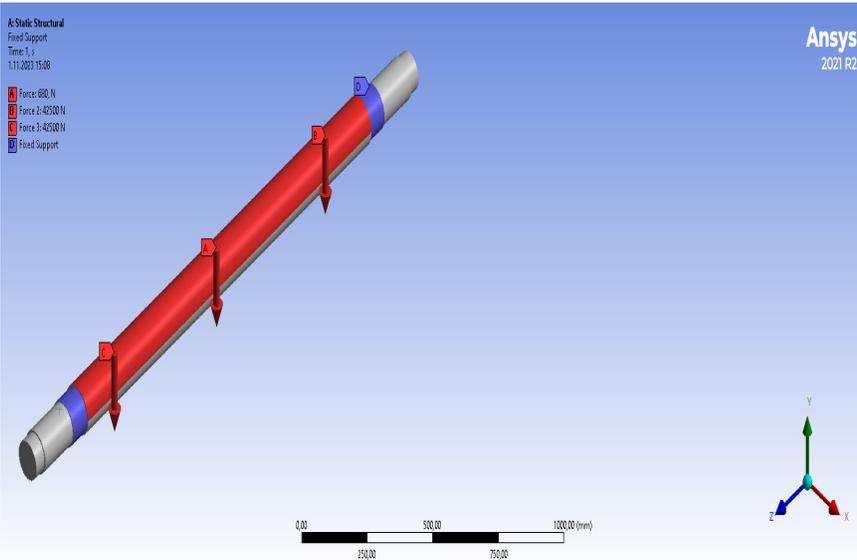


Figure 8. Defining boundary conditions for circular cross-section axle

Figure 9 shows the load diagram applied to the square section axle. On the surface shown in red, a load of 680 N is applied to point A and 42,500 N is applied to points B and C. Point D, shown in purple, is the fixed support point.

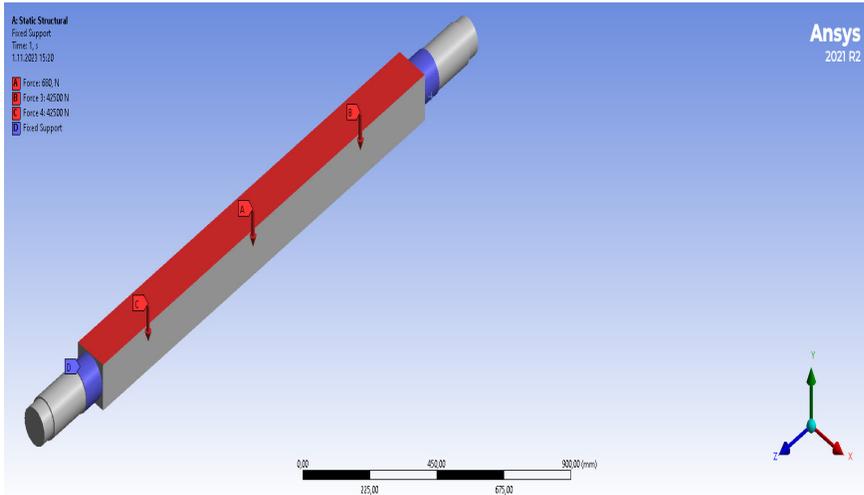


Figure 9. Defining boundary conditions for square section axle

RESEARCH FINDINGS AND DISCUSSION

After the stress analysis solution process, the stress distributions occurring on the axle are given in Figures 10-11. When the structure of the axle is examined, it is seen that the maximum equivalent stress is in the regions where the axle shaft intersects with the support points. The maximum stress value was found to be 124.77 MPa for the axle with circular cross-section and 106.62 MPa for the axle with square cross-section. When these values are evaluated in terms of material, they are below the yield strength. The maximum equivalent stress and the safety coefficients obtained according to the yield strength of the material for Figures 10-11 are given in Table 2. When the equivalent stress values of all structural elements are analyzed, it is seen that the axle operates safely without damage under the application conditions.

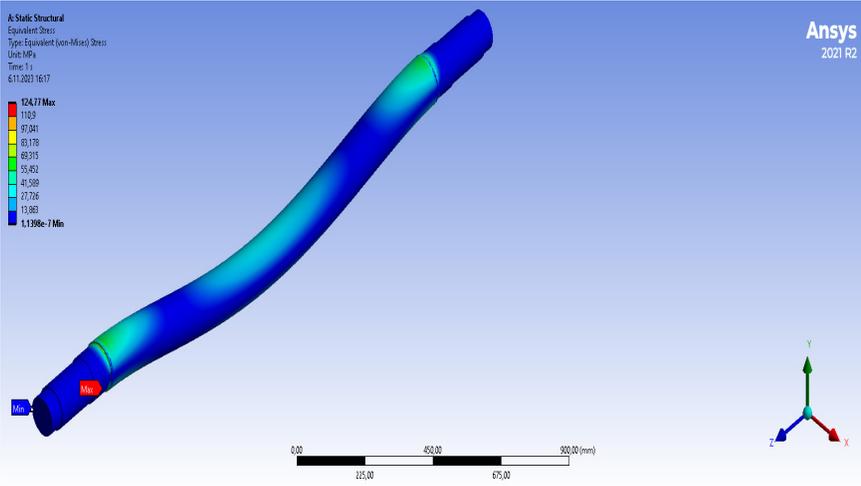


Figure 10. Distribution of equivalent stresses for circular axle

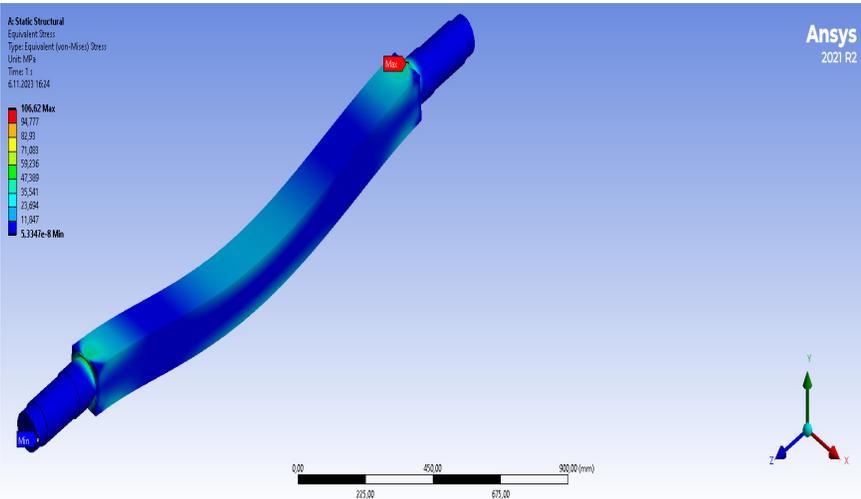


Figure 11. Equivalent stress distributions for square section axle

Table 2. Calculated operational safety coefficients for axle

Axle Cross Section		Material yield strength (σ_{yield}) [MPa]	Max. Equivalent stress (σ_{eq}) [MPa]	Emniyet katsayısı (k_s) [k_s]= $[\sigma_{yield} / \sigma_{eq}]$
Circular Axle	Section	250	124,77	2,00
Square Axle	Section	250	106,62	2,34

In the research, displacement analysis was performed under the effect of stresses applied to the axle. After the analysis, the total displacement values occurring on the axle are given in Figures 12-13. When the structure of the axle is examined, it is seen that the total displacement values are in the middle parts of the axle. The total displacement value was found to be 0.43021 mm for the axle with circular cross-section and 0.28367 mm for the axle with square cross-section. The values obtained according to the displacement analysis for Figures 12-13 are given in Table 3.

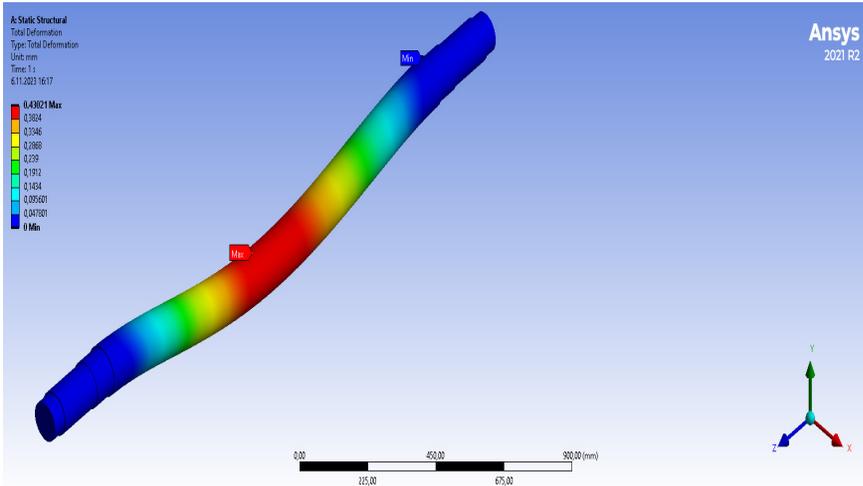


Figure 12. Maximum total displacement distribution for circular axle

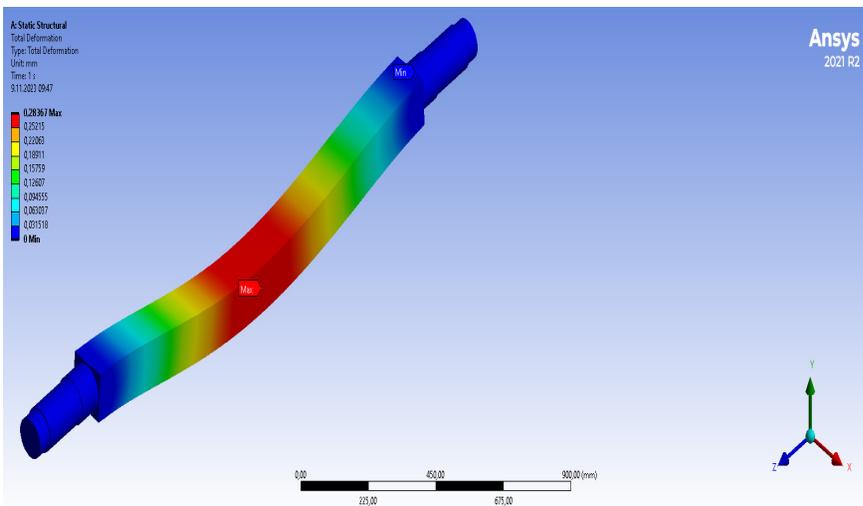


Figure 13. Maximum total displacement distribution for square section axle

Table 3. Calculated displacement values for axle

Axle Cross Section	Displacement Values (mm)
Circular Section Axle	0,43021
Square Section Axle	0,28367

In the analysis, the stress energy values on the axle are calculated and given in Figures 14-15. The blue colour indicates the minimum stress energy and the red colour indicates the maximum stress energy value on the axle. For the axle with circular cross-section, the stress energy value was found to be 2.5348 mJ and for the axle with square cross-section, the stress energy value was found to be 2.3689 mJ. The values obtained according to the stress energy analysis for Figures 14-15 are given in Table 4.

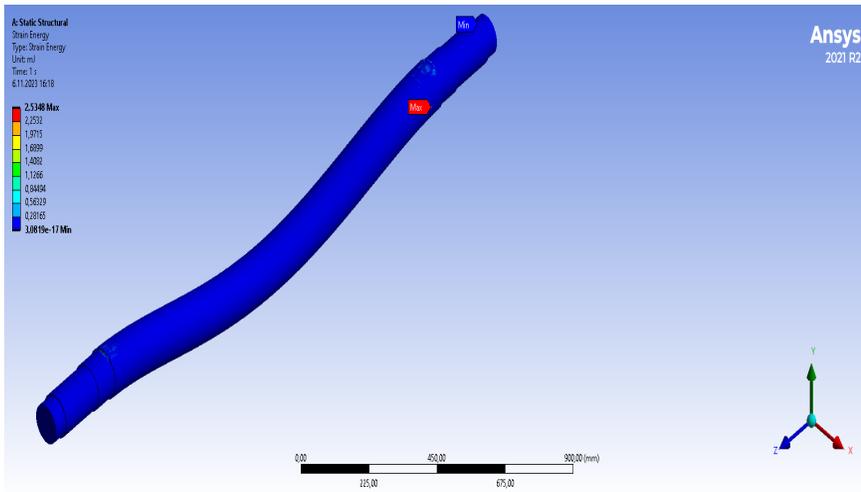


Figure 14. Stress energy distribution for circular cross-section axle

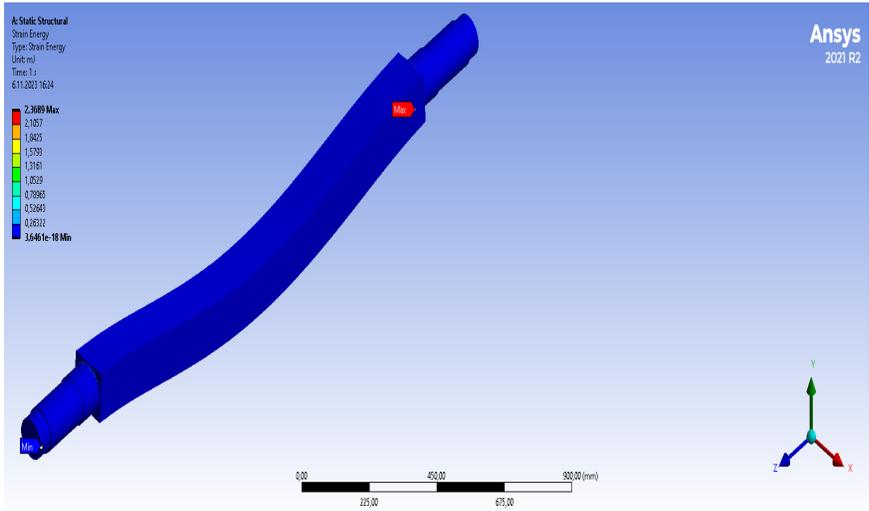


Figure 15. Stress energy distribution for square section axle

Table 4. Stress energy values calculated for the axle

Axle Cross Section	Stress Energy Values (mJ)
Circular Section Axle	2,5348
Square Section Axle	2,3689

In the analysis, the safety factor values on the axle are calculated and given in Figures 16-17. The blue colour indicates the maximum factor of safety and the red colour indicates the minimum factor of safety value on the axle. For the axle with circular cross-section, the maximum factor of safety value is 15 and the minimum value is 0.69089, while for the axle with square cross-section, the maximum factor of safety value is 15 and the minimum value is 0.80845. Safety factor values for Figures 16-17 are given in Table 5.

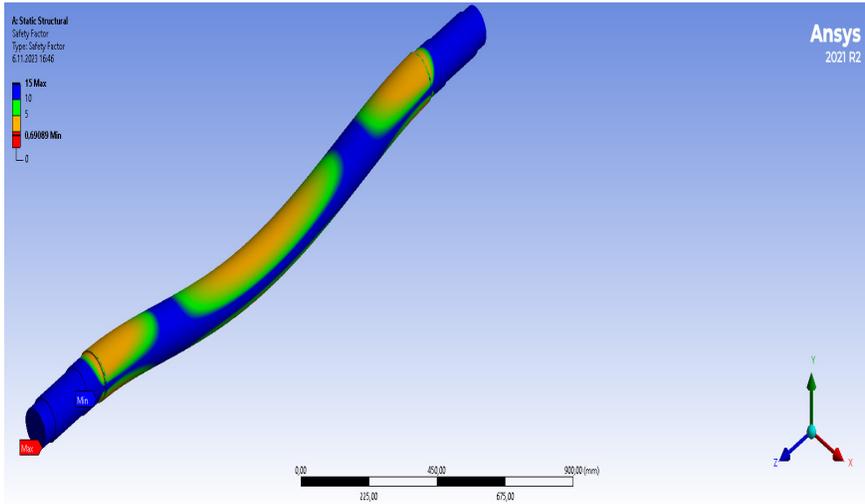


Figure 16. Safety factor value for circular cross-section axle

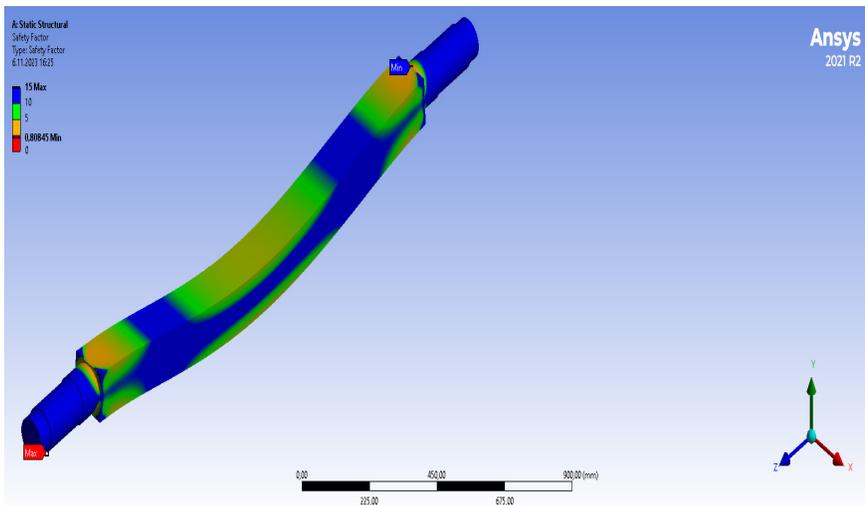


Figure 17. Safety factor value for square section axle

Table 5. Safety factor values calculated for axle

Axle Section	Safety Factor Values
Circular Section Axle	
Maximum	15
Minimum	0,69089
Square Section Axle	
Maximum	15
Minimum	0,80845

CONCLUSION

In this study, three-dimensional solid modelling of the axle was made, stress and displacement analysis of the modelled axle under normal conditions were simulated and the safety factor of the axle was calculated. The results obtained as a result of the analyzes are given below.

- a. For the circular cross-section axle construction, the maximum equivalent stress value was found to be 124.77 MPa at the intersection of the axle shaft with the support points.
- b. For the square section axle construction, the maximum equivalent stress value was 106.62 MPa at the intersection of the axle shaft with the support points.
- c. For the circular cross-section axle construction, the maximum total displacement was found to be 0.43021 mm at the centre of the axle.
- d. For the square section axle construction, the maximum total displacement was found to be 0.28367 mm at the centre of the axle.
- e. The stress energy value for the axle with circular cross section was calculated and found to be 2.5348 mJ.
- f. The stress energy value for the axle with square cross section was found to be 2.3689 mJ.
- g. The maximum safety factor value of the circular cross-section axle was found to be 15 and the minimum safety factor value was found to be 0.69089.
- h. The maximum safety factor value of the square section axle was found to be 15 and the minimum safety factor value was found to be 0.80845.
- i. In the simulation, no damage was found in the construction of the axle. It was determined that the axle element and the materials

used in the structural elements carried the forces applied at different points within the elastic deformation limits.

Strength analysis of the products to be designed with 3D solid modelling techniques and finite element method will minimize the loss of time and material (Değirmencioğlu et al., 2003). In this context, the data obtained in the virtual environment should be interpreted very well before manufacturing and experimental studies should be applied when necessary.

RESOURCES

- Acar, A.İ., Öztürk, R., Güner, M. (2011). Agricultural Tools and Machines, Anadolu University Publications, Yay. No: 2354, Eskisehir.
- Akıncı, İ., (1994). Development of a Computer Aided Measurement System for the Determination of Tractor-Agricultural Machine Energy Relationships and a Research on the Determination of Basic Operational Data in Mechanization Planning. Doctoral Thesis, Çukurova University Institute of Science and Technology (Unpublished), Adana, Turkey
- Değirmencioğlu, A., Yürdem, H., Gülsoylu, E., Çakır, E., Evcim, Ü., Keçecioglu, G., (2003). “Determination of Stresses Under Load in a Three-Socket Plow Roof”, Research Project (Project No: 98 ZRF 046), Ege University, Faculty of Agriculture.
- Korucu, T., Kirişci, V., Selvi, K.Ç. (2003). Principles of Tractor and Machinery Use for Reducing Soil Compaction, 21st National Congress on Agricultural Mechanization, 3-5 September 2003, 172-178, Konya.
- Terzi, İ., Özgüven, M. M., & Altaş, Z. (2021). Use of ANSYS in Agricultural Applications: Agricultural Cart Axle Modeling and Analysis Example. International Journal of Agricultural and Wildlife Sciences, 7(3), 503-514.
- Zeytinoğlu, M. (2006). Stress Analysis of the Drawing Ring of a 3.5 Ton Single Axle Agricultural Cart by Finite Element Method. Journal of Uludag University Faculty of Agriculture, 2(21), 21-24.



DYNAMIC RISK MANAGEMENT IN THE PRIVATE SECTOR: A VBA-ENABLED L-TYPE MATRIX APPROACH

Zehra GÜLTEN YALÇIN¹

M. Bora AKIN²

Mustafa DAĞ³

1 Asst. Prof. Dr. Zehra Gülten Yalçın, Çankırı Karatekin Üniversitesi Kimya Mühendisliği Bölümü Uluyazı Kampüsü Merkez/Çankırı, Orcid: 0000-0001-5460-289X

2 Asst. Prof. Dr. M. Bora Akın Çankırı Karatekin Üniversitesi Kimya Mühendisliği Bölümü Uluyazı Kampüsü Merkez/Çankırı, Orcid: 0000-0003-3841-1633

3 Res. Asst. Dr. Mustafa Dağ Çankırı Karatekin Üniversitesi Kimya Mühendisliği Bölümü Uluyazı Kampüsü Merkez/Çankırı, Orcid: 0000-0001-9540-3475

Introduction

Occupational Health and Safety (OHS) in Türkiye has been incorporated into the framework of Occupational Health and Safety Law No. 6331 since 2012. A primary focus within this legislative context is the undertaking of risk analysis studies, with the objective of preventing work-related accidents and occupational diseases. Occupational Health and Safety, as a scientific discipline, encompasses the identification, recognition, prediction, evaluation, and control of potential hazards within the contemporary workplace (Dinkçi & Akpınar, 2023). This interdisciplinary field mandates a thorough examination of workplace hazards, with a paramount emphasis on the analysis of dual hazards to ensure a secure and healthy working environment for both employees and the surroundings. The responsibility for averting occupational accidents and diseases within a workplace lies with the employer. As stipulated by Law No. 6331, employees are obligated to adhere to all directives outlined within the legal framework. Furthermore, employers are required to assess and mitigate risks present in the workplace, particularly those of elevated magnitude, through the implementation of preventive measures. A study conducted by the International Labor Organization (ILO), as of July 12, 2023, reveals Costa Rica as the foremost country in non-fatal occupational injuries, reporting 9421 incidents per 100,000 workers. Nicaragua and Finland occupy the second and third positions, respectively. Türkiye is situated at the 11th position in this ranking. In terms of occupational fatalities per 100,000 workers, Cuba leads with 25, followed by Burundi and Egypt. Türkiye ranks 15th in this specific list. Remarkably, Seychelles, with 3.1 inspectors per 10,000 employees, emerges as the country with the highest density of inspectors for implementing relevant legislation. Nevertheless, an examination of statistical data unveils a deficiency in the quantity of inspectors, underscoring the necessity to judiciously employ technology for streamlined, punctual, and thorough inspections of enterprises (<https://ilostat.ilo.org/topics/safety-and-health-at-work/>). Notably, Türkiye has garnered international distinction for its meticulous compilation and provision of statistical data pertaining to occupational accidents (Ersoy, 2022).

In a study spanning the years 2010 to 2019, the Social Security Institution (SSI) in Türkiye disclosed that data pertaining to work accidents and occupational diseases had not been reported to the SSI. A subsequent investigation in 2018 underscored the industries with the highest incidence of work accidents, revealing construction and metal production sectors as predominant. On a sectoral analysis, the study discerned that the construction and metal production industries exhibited elevated rates of work accidents. However, upon closer scrutiny of accident probability rates, the mining sector emerged as the sector with the highest probability. Notwith-

standing this finding, the study accentuated that the construction industry consistently maintained the foremost position in terms of fatalities resulting from work accidents (Derin & Şahin, 2022).

Table 1: *Occupational Injuries, Occupational Deaths, and Inspectors by Country* (<https://ilostat.ilo.org/topics/safety-and-health-at-work/>)

Country	Non-fatal Occupational Injuries (per 100,000 workers)	Occupational Deaths (per 100,000 workers)	Number of Inspectors (per 10,000 employees)	Country	Non-fatal Occupational Injuries (per 100,000 workers)	Occupational Deaths (per 100,000 workers)	Number of Inspectors (per 10,000 employees)
Costa Rica	9.421	9.7	0.6	Malaysia	578	3.8	0.3
Nicaragua	4.891	8		Iceland	553	1.5	
Finland	4.025	0.7	1.3	Croatia	549	2.9	1.1
Argentina	3.310	3.2	0.2	Ireland	526	1.8	0.3
Chile	3.142	3.1	0.9	Zimbabwe	480	9.5	1
France	2.931	2.5	0.8	Hungary	464	1.8	0.7
Pakistan	2.691			Poland	453	1.4	0.9
Uruguay	2.654	3.7	0.6	Lithuania	436	4.3	0.9
Denmark	2.565	1.3		Cyprus	420	3.8	0.5
Mexico	2.529	7.7	0.1	Philippines	417	9.6	0.2
Türkiye	2.459	6.3	0.3	Barbados	388	0.8	1.4
Spain	2.347	1.9	1.1	Singapore	386	1.1	1.2
Belgium	2.314	0	0.6	Slovakia	359	1.5	1.1
Portugal	2.260	2.7	0.7	Latvia	301	5.1	2
Switzerland	2.108	1.1	1.4	Japan	266	1.5	0.5
Réunion	1.989	2.3		Mauritius	198	0.6	2.9
Macau, China	1.891	6.9	2.7	Ukraine	166	7.6	0.8
Slovenia	1.868	1.9	0.9	Seychelles	165	4.8	3.1
Israel	1.660	1.4	0.5	Bahrain	109	0.6	0.3
Germany	1.505	0.7	1.4	Greece	105	0.9	
Luxembourg	1.461	1.7		Russian Federation	102	6	
Austria	1.417	2.4	0.7	Republic of Moldova	84	4.8	0.4
Italy	1.413	3.4		Bulgaria	77	3.7	1
Canada	1.408	5.1	0.1	Occupied Palestinian	74	1	0.8
Brazil	1.374	7.4	0.3	Romania	71	2.6	1.9
Guadeloupe	1.349	6.8		Belarus	52	2.6	0.4

New Zealand	1.200	2.3	0.2	Norway	48	1.1	1.2
Hong Kong, China	1.188	6.8	0.5	Kazakhstan	42	4.3	
French Guiana	1.057	0		Armenia	29	4.2	1.1
Cuba	1,017	25	0.8	El Salvador	29	0.1	0.5
Netherlands	997	0.3		Uzbekistan	27	5.8	0.2
Belize	978	0.9	1.4	Georgia	26	2.7	0.3
United States	900	5.3	0.1	Kyrgyzstan	22	4.1	
Australia	899	1.6		Qatar	21	5.9	1.3
Malta	863	3	0.3	Mongolia	20	3	0.7
Thailand	762	5.3	0.2	Azerbaijan	16	3	0.5
Czechia	745	2.3	1	Sri Lanka	14	0.8	0.6
Burundi	707	13.8		Myanmar	12	3.2	0.1
United Kingdom	692	0.8	0.3	New Caledonia	6	7	
Sweden	689	0.8	0.5	Colombia	4	0	0.4
Egypt	670	10.7		Panama	2	0.2	0.6
Estonia	593	2	0.7				

In accordance with Article 15 of the Occupational Health and Safety Law, the law mandates employers to conduct health checks. As outlined in this article, employers are obliged to request employees to undergo health surveillance at specified intervals. This requirement applies when employees commence a new job, experience a job change, or return to work following a work accident, occupational disease, or extended absence due to health reasons. The timing of health surveillance is contingent upon the nature of the employee's work, the characteristics of the job, and the hazard class of the workplace. The Ministry establishes the regular intervals for health surveillance (İncekara, 2020).

It is incumbent upon employers to bear the expenses incurred during the health surveillance process, along with the costs associated with the assessment of findings and the treatment of employees (Karahmetoğlu, 2022).

The integral process of risk assessment is systematic and involves the identification of hazards, as well as the analysis and control of risks. Both qualitative and quantitative methodologies are employed in studies aimed at recognizing hazards within a workplace. Subsequent efforts focus on mitigating high-risk factors through the implementation of preventive actions (<https://safetyculture.com/topics/risk-assessment/>)

Risk assessment is alternatively defined as the thorough examina-

tion and delineation of the risk emanating from a hazard, coupled with an evaluation of whether the implemented measures effectively diminish these risks to levels deemed acceptable. The origins of risk assessment in the realm of occupational safety can be traced back to 1950, marking the inception of studies dedicated to this critical aspect of working life. The methodologies employed for risk assessment have undergone evolution over the years, adapting to specific applications and objectives. Research endeavors in this domain encompass a spectrum of activities, ranging from the containment of accidents to the exploration and development of alternative risk assessment methods (Karakurt, Hekimoğlu & Güneri, 2021).

Risk analysis methods

Various risk analysis methods are employed in different contexts to assess and manage potential hazards. Notable methods include Hazard and Operability (HAZOP), Fault Tree Analysis (FTA), Fine Kinney Method, Check List, Cause and Effect Analysis, L Type Matrix, and Multivariate X Type Matrix Diagram (Oturakci & Dağsuyu, 2017; Usanmaz & Köse, 2020).

Among these methodologies, the L Type Matrix, specifically the 5x5 risk matrix, stands out as one of the most commonly utilized methods in businesses. This matrix is particularly employed to ascertain cause-effect relationships in the context of risk analysis. The L Type Matrix involves grading and measuring both the probability of an event occurring and the severity if the event transpires. The risk value is then calculated by multiplying the selected values from the severity and probability table (Ulu & Arısoy, 2024). This structured approach facilitates a comprehensive assessment of risks and aids in making informed decisions for risk mitigation and management.

In the surveyed literature, it was observed that certain studies incorporated simulation programs employing diverse risk analysis methods. Notably, some investigations utilized a combination of Analytical Hierarchy Process (AHP) and Artificial Neural Networks (ANN) methods (Türker & Evidence, 2020). Additionally, a study by Cürebal and Eren (2021) integrated AHP and TOPSIS methods for evaluation purposes.

In a noteworthy study conducted by Öztürk, Güngör, and Lepki in 2016, a decision-making system tailored for the logistics sector was established using Microsoft Excel. The development of the necessary tables in MS Excel involved the design of forms and the creation of interfaces using Visual Basic Applications (VBA). These designed forms and interfaces not only render the solution path user-friendly but also enhance its comprehensibility. Furthermore, the matrices established within the tables contrib-

ute to the practicality of data storage applications in this decision-making system. This integrated approach not only demonstrates the versatility of risk analysis methods but also showcases the adaptability of these methods across different sectors and applications.

Simulation Modeling Using VBA in MS Excel Program

In numerous studies, it has been observed that diverse simulation programs are employed, with specialized programs developed to suit specific contexts. This trend extends to the field of occupational health and safety, where simulation programs tailored for the unique demands of the discipline have been created (Tedonchio, Nadeau, Boton, & Rivest, 2022).

Given the considerable expense associated with simulation software, there is a notable preference for more cost-effective alternatives. Particularly, Visual Basic for Applications (VBA) is favored over Microsoft Excel due to its affordability and widespread use. While MS Excel is a widely used platform, the cost analysis of simulation software often makes VBA a more economical choice (Bejinariu, Darabont, Cazac, & Chiriac, 2023). VBA, allowing for code writing within the program, can function as simulation software when coupled with MS Excel. The process involves recording input data for the simulation model in MS Excel using VBA. Parameters identified as variables are then encoded in the program, culminating in the creation of a simulation model. The outcomes of the simulation can be conveniently displayed in tables or graphs within MS Excel. The preference for using VBA in MS Excel is notable among businesses seeking rapid and efficient results, owing to its highly practical and user-friendly interface (Uluskan & Yusuf, 2020).

In the present study, a meticulous assessment of a 5x5 Matrix diagram, specifically the L Type Matrix, was conducted. The focus of this evaluation centered on scrutinizing cause-effect relationships within a workplace dedicated to the production of steel doors. Notably, Visual Basic for Applications (VBA) was employed to facilitate the systematic analysis and interpretation of data within this matrix diagram. This approach allowed for a comprehensive exploration of the intricate cause-and-effect dynamics pertinent to the production environment, offering a tailored and efficient means of examining the potential risks associated with steel door manufacturing. The utilization of VBA provided a versatile and user-friendly platform, streamlining the process of evaluating the 5x5 Matrix and contributing to the overall effectiveness of the risk assessment in the workplace.

Risk Assessment Decision Matrix:

The risk assessment matrix, recognized as one of the most prevalent methodologies, was originally devised to fulfill the requisites outlined in the system security program, specifically denoted as the US Military standard MIL_STD_882-D. Serving as a fundamental approach to risk evaluation, this matrix offers a systematic framework for assessing and managing risks within various contexts. Matrix diagrams, constituting an essential component of the risk assessment matrix, operate as evaluative tools adept at scrutinizing the relationships between two or more variables. This method provides a structured means to analyze and comprehend the intricate interdependencies among diverse elements, thereby enhancing the effectiveness of risk assessment efforts (Lafçı and Öztekin, 2020).

L Type Matrix

The 5x5 Matrix diagram, commonly referred to as the L Type Matrix, holds a particular significance in the evaluation of cause-effect relationships. Its straightforward design makes it an ideal choice for analysts conducting risk analysis independently. This method proves particularly useful in businesses where prompt identification of imminent dangers and the immediate implementation of precautions are imperative. The application of the 5x5 Matrix involves a systematic process wherein the probability of an event occurring and the severity of its consequences are assessed and graded (Ersoy, & Kaya 2019).

The risk score is then calculated by multiplying the assigned probability (as per Table 1) with the degree of harm (as per Table 2). The resulting value is then cross-referenced in the matrix, as illustrated in Table 3. This formulaic approach, expressed as:

$$\text{Risk Score} = \text{Likelihood} \times \text{Degree of Harm}$$

serves as an effective means of quantifying and categorizing risks within the matrix, providing a tangible metric for further analysis and decision-making (Table 1).

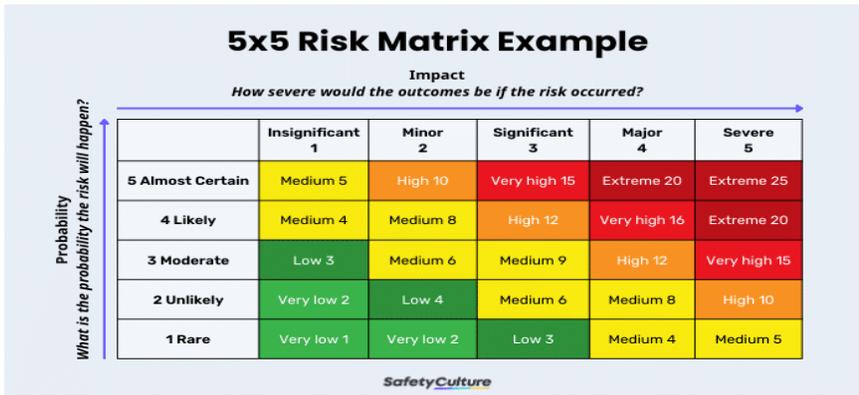
Table 1. Table for determining the probability of an event occurring

PROBA-BILITY	RATING STEPS FOR THE LIKELIHOOD OF EMERGENCE
(1)	Remote possibility
(2)	Low probability (once a year)
(3)	Possible
(4)	Often (once or several times a month)
(5)	Very often (constant-almost every day)

Table 2. Table for determining the degree of damage of an event

CONCLUSION	RATING
(1)	Requires first aid (no loss of working hours)
(2)	Requires first aid, requires outpatient treatment (no lost workdays)
(3)	Minor injury
(4)	Serious injury
(5)	Death

Table 3. Risk Scores



The interpretation of this value is imperative, and subsequent decisions regarding the appropriate course of action should be made. Table 4 provides comprehensive information regarding the recommended actions corresponding to the obtained results. Precautionary measures are implemented commencing from the highest level of risk (Şahin, & Vapur, 2021)

Table 4. Risk scores matrix

CONCLUSION	ACTION
Intolerable Risks (25)	The commencement of work is contingent upon the mitigation of identified risks to a level deemed acceptable. In the event of an ongoing activity, an immediate cessation is mandated. Should risk reduction prove unattainable despite concerted efforts, the initiation of the activity must be precluded.
Significant Risks (15,16,20)	The initiation of work is contingent upon the reduction of identified risks, with an imperative for immediate cessation of ongoing activities if such risks are extant. In cases where the risk pertains to the ongoing work, expeditious measures are to be implemented, and consequent to these interventions, a determination regarding the continued pursuit of the activity should be reached.

Moderate Risks (8,9,10,12)	Initiation of activities aimed at reducing identified risks is recommended. It is important to note that the implementation of risk mitigation measures may necessitate a considerable duration.
Tolerable Risks (2,3,4,5,6)	While the elimination of identified risks may not necessitate the introduction of additional control processes, it remains imperative to uphold existing controls. Vigilant supervision is essential to ensure the ongoing maintenance of these controls.
Minor Risks (1)	The planning of control processes and the documentation of activities for the elimination of identified risks may not be requisite in certain instances.

Assessment of Result Acceptability Values

After the implementation of mitigation measures, it is essential to reassess the identified risk by determining a new risk score. This process involves completing the relevant form once again, as stipulated by Yemişçioglu and Şimşek (2023).

The study employed Visual Basic for Applications within the MS Excel program for interface programming. This facilitated the L-type Matrix Risk Assessment of a facility through a user-friendly interface, allowing direct data entry into the programmed system. This approach not only streamlines the risk assessment process but also eliminates the need for traditional paperwork, thereby enhancing efficiency. The interface comprises two layers. The first layer involves entering the initial evaluation data for the facility. The second layer functions as a platform for inputting post-mitigation evaluation data, allowing for a comprehensive view of the assessment process and the effectiveness of risk preventive measures.

Input Interface for Initial Review Data

In the initial layer, pertinent information, including the identification of hazards following the initial facility inspection, the corresponding risk, probability, frequency, and impact values associated with each hazard, as well as the recommended mitigation measures and details regarding the individual responsible for corrective actions, are inputted (refer to Figure 1). The functionality of the data entry process is facilitated through a designated 'Save' command button incorporated into the form.

Figure 1. *The interface for inputting data during the initial on-site inspection*

The identification of hazards and corresponding risks labeled as ‘Danger’ and ‘Risk,’ respectively, is facilitated through the use of ComboBoxes. Similarly, ComboBoxes are employed for selecting precautions and entering responsible parties. A dedicated ‘Data’ page has been devised to capture ComboBox data, allowing for the seamless integration of ready-made data into the form. This approach is designed to establish consistency in the definitions of these categories. Notably, the user-friendly interface enhances accessibility, as evidenced by the feature wherein entering a letter in the ComboBox prompts the display of data from the ready-made list starting with that letter (see Figure 2).

L TYPE RISK ASSESSMENT REPORT

FIRST INVESTIGATION | LAST INVESTIGATION

SECTION/ACTIVITY: GENERAL

HAZARD SOURCE: WATER HEATER | BOSCH

HAZARD: ELECTRIC SHOCK

RISK: BURNING | INJURY | DEATH

POSSIBILITY: 5 x INTENSITY: 5 = RISK SCORE: 25

DEADLINE: 7.12.2023

RECOMMENDATIONS/PRECAUTIONS TO BE TAKEN

ELECTRICAL CABLES WILL BE PROTECTED AGAINST MECHANICAL FACTORS

PEOPLE WHO WILL BE AFFECTED: [Dropdowns]

PEOPLE RESPONSIBLE FOR THE PROCESS: [Dropdowns]

SELECT PHOTO

SAVE

PATH AND TITLE OF PHOTO

Figure 2. Facilitating the retrieval of ‘Danger’ data by entering letters

The risk value is computed through the automatic multiplication of probability, frequency, and impact values. This computation is triggered automatically upon any change in the relevant data’s TextBox objects. Subsequently, the risk level derived from this calculation is programmed to be automatically populated into the TextBox objects for decision and deadline data (see Figure 3). Notably, an ‘image’ feature is specifically employed to include a visual representation reminiscent of the identified danger.

L TYPE RISK ASSESSMENT REPORT

FIRST INVESTIGATION | LAST INVESTIGATION

SECTION/ACTIVITY: GENERAL

HAZARD SOURCE: WATER HEATER | ARÇELİK

HAZARD: ELECTRIC SHOCK

RISK: BURNING | INJURY | DEATH

POSSIBILITY: 5 x INTENSITY: 5 = RISK SCORE: 25

DEADLINE: 7.12.2023

RECOMMENDATIONS/PRECAUTIONS TO BE TAKEN

- ELECTRICAL CABLES WILL BE PROTECTED AGAINST MECHANICAL FACTORS
- FIRE EXTINGUISHER WILL BE AVAILABLE
- INSTRUCTIONS WILL BE PREPARED
- SUFFICIENT AND SUITABLE FIRE EXTINGUISHERS WILL BE PROVIDED
- TRAINING

PEOPLE WHO WILL BE AFFECTED: VISITORS | CHEF | EMPLOYEE

PEOPLE RESPONSIBLE FOR THE PROCESS: AUTHORIZED ELECTRICIAN | CHEF | EMPLOYER | FACTORY MANAGER | MACHINE OPERATOR



C:\Users\mbora\Downloads\WhatsApp Image 2023-11-07 at 11.33.34.jpeg

SELECT PHOTO

SAVE

Figure 3. The finalized form resulting from data entry in the initial review layer

Upon completion of data entry, pressing the save button appends the information from the objects to the first available blank line on the MS Excel Analysis page. Consequently, each entry is recorded on a new line (refer to Figure 4).

No	Hazard Source	Hazard	Risk	Possibility	Severity	Risk Score	Recommendations / Precautions to be taken	People who will be affected	People responsible for the process	Deadline	Periodicity	Risk Index	Relevant Regulation
1	GENERAL ARÇELİK	WATER HEATER	ELECTRIC SHOCK	BURNING, INJURY, DEATH	5	25	ELECTRICAL CABLES WILL BE PROTECTED AGAINST MECHANICAL FACTORS. FIRE EXTINGUISHER WILL BE AVAILABLE. INSTRUCTIONS WILL BE PREPARED. SUFFICIENT AND SUITABLE FIRE EXTINGUISHERS WILL BE PROVIDED. TRAINING	VISITORS, CHEF, EMPLOYEE..	AUTHORIZED ELECTRICIAN, CHEF, EMPLOYER, FACTORY MANAGER, MACHINE OPERATOR	7.12.2023			

Figure 4. Transferring data to MS Excel

Final Examination Data Input and Comparative Analysis with Initial Data

A command button labeled ‘Update’ has been designated to retrieve data from the initial review in the last review layer. Through the functionality embedded in this button, the program automatically retrieves the first set of data that has not undergone the final analysis from the MS Excel sheet. Subsequently, the user is prompted to enter their conclusive assessment in the ‘Rating of the risk after the measures are taken’ section (refer to Figure 5).

L TYPE RISK ASSESSMENT REPORT ✕

FIRST INVESTIGATION | LAST INVESTIGATION

No: 1 **Deadline:** 7.12.2023 UPDATE

Section / Activity: GENERAL -
ARCELİK

Hazard Source: WATER HEATER

Hazard: ELECTRIC SHOCK

Risk: BURNING, INJURY, DEATH

Possibility	Intensity	Risk Score
5	x 5	= 25

Recommendations/Precautions To Be Taken

ELECTRICAL CABLES WILL BE PROTECTED AGAINST MECHANICAL FACTORS FIRE EXTINGUISHER WILL BE AVAILABLE INSTRUCTIONS WILL BE PREPARED SUFFICIENT AND SUITABLE FIRE EXTINGUISHERS WILL BE PROVIDED TRAINING

People who will be affected: VISITORS, CHEF, EMPLOYEE, ,

People responsible for the process: AUTHORIZED ELECTRICIAN, CHEF, EMPLOYER, FACTORY MANAGER, MACHINE OPERATOR

RATING OF THE RISK AFTER TAKING PRECAUTION




C:\Users\mbora\Downloads\WhatsApp Image 2023-11-07 at 11.33.35.jpeg

POSSIBILITY	INTENSITY	RISK SCORE
<input style="width: 30px;" type="text" value="1"/>	x <input style="width: 30px;" type="text" value="5"/>	= <input style="width: 30px;" type="text" value="5"/>

RELEVANT REGULATIONS

REGULATION NUMBER 11

SELECT PHOTO

SAVE

Figure 5. *The conclusive evaluation layer*

In this section, subsequent to the input of probability and severity parameters, the system automatically retrieves the risk score. A designated textbox is provided to reference regulations or offer explanations regarding the corrective actions taken (refer to Figure 6). The ‘Update’ button facilitates the uploading of the previously captured image from the specified file path. The ‘Save’ CommandButton, programmed to execute a specific procedure, ensures that the latest data is appended adjacent to the retrieved information, thereby finalizing the evaluation process. At this juncture, users have the option to select and upload a photograph from the final inspection, offering a clear visual representation of the changes made (see Figure 7).

L TYPE RISK ASSESSMENT REPORT ✕

FIRST INVESTIGATION | LAST INVESTIGATION

No: 1 **Deadline:** 7.12.2023 UPDATE

Section / Activity GENERAL -
ARCELİK

Hazard Source: WATER HEATER

Hazard: ELECTRIC SHOCK

Risk: BURNING, INJURY, DEATH

Possibility Intensity Risk Score

5 x 5 = 25

Recommendations/Precautions To Be Taken

ELECTRICAL CABLES WILL BE PROTECTED AGAINST MECHANICAL FACTORS FIRE EXTINGUISHER WILL BE AVAILABLE INSTRUCTIONS WILL BE PREPARED SUFFICIENT AND SUITABLE FIRE EXTINGUISHERS WILL BE PROVIDED TRAINING

People who will be affected: VISITORS, CHEF, EMPLOYEE, ,

People responsible for the process: AUTHORIZED ELECTRICIAN, CHEF, EMPLOYER, FACTORY MANAGER, MACHINE OPERATOR

RATING OF THE RISK AFTER TAKING PRECAUTION




C:\Users\mbora\Downloads\WhatsApp Image 2023-11-07 at 11.33.35.jpeg

POSSIBILITY

INTENSITY

RISK SCORE

1 x 5 = 5

RELEVANT REGULATIONS

REGULATION NUMBER 11

SELECT PHOTO

SAVE

Figure 6. The visual representation of the last review layer subsequent to data entry

When the 'Fetch' button is activated, the initial examination data that has not undergone prior evaluation is retrieved, awaiting assessment and subsequent saving. Upon completion of the saving process, the report's visual depiction in the MS Excel program is illustrated in Figure7.

No	Activity	Hazard Source	Hazard	Risk	Possibility	Likelihood	Risk Score	Recommendations / Precautions to be taken	People who will be affected	People responsible for the process	Deadline	Feasibility	Intensity	Risk Score	Relevant Regulation
1	GENERAL ARÇELİK	WATER HEATER	ELECTRIC SHOCK	BURNING, INJURY, DEATH	5	5	25	ELECTRICAL CABLES WILL BE PROTECTED AGAINST MECHANICAL FACTORS FIRE EXTINGUISHER WILL BE AVAILABLE INSTRUCTIONS WILL BE PREPARED SUITABLE AND SUITABLE FIRE EXTINGUISHERS WILL BE PROVIDED TRAINING	VISITORS, CHEF, EMPLOYEE,	AUTHORIZED ELECTRICIAN, CHEF, EMPLOYER, FACTORY MANAGER, MACHINE OPERATOR	7.12.2023	1	5	5	REGULATION NUMBER 11

Figure 7. The MS Excel visual representation obtained post-saving

RESULT

Within the operational domain of a steel door manufacturing enterprise, a rigorous risk assessment was systematically executed, employing a 5x5 Matrix diagram, specifically emphasizing the scrutiny of cause-effect relationships. This meticulous evaluation was particularly focused on sections where both low and high risks are deemed permissible. Broadly encompassing the workplace environment, comprehensive risk studies were conducted in diverse areas such as “Smoking in the workplace,” “Electrical installations and electrical machines,” “Fire,” “Electric cables,” “Tea stove,” “Manual handling of heavy goods,” “Service vehicles,” “Utilization of hand tools,” “Circular saw,” “Operation of a clamping machine,” “Operation of a press brake,” “Electric welding processes,” “Plasma Powermax 30 operation,” “Operation of a band saw,” “Stationary drill,” and “Gas welding machine.”

Risk assessments were further extended to specific working sections, culminating in the identification of potential sources of danger. The risks associated with these hazards were delineated as follows: “Fire at work, leading to death and injury,” “Contact with sockets using wet hands, resulting in electric shock,” “Fire, injury, and material damage due to burning, potentially leading to death,” “Overturning of the stove, resulting in burns, injury, and potential fatality,” “Traffic accidents, potentially resulting in death and injury,” “Cable failure of power tools, potentially leading to death and injury,” “Machine cables operating without protection, posing risks of injury and fatality,” “Injury and death due to lack of grounding,” “Working without machine protectors, posing risks of injury and death,” “Misplacement of the chassis required for the welding machine, resulting in potential electric shock,” “The arm of the welding machine lacking insulation, posing risks of electric shock,” “Defective machine cables, posing

risks of injury or death,” “Utilizing a tube with a malfunctioning pressure gauge, posing risks of explosion, injury, and death,” “Leaving hand tools connected to electrical plugs, posing risks of injury and death,” and “Inappropriate behavior during travel, posing risks of traffic accidents, death, and injury.”

The initial risk score of 25 prompted the implementation of requisite precautions and studies in areas approaching the danger threshold, ultimately resulting in a commendable reduction of the risk value to 5. Notably, during the ongoing risk assessment process, the designated expert is equipped with a portable device for document and photograph acquisition in the field. Leveraging the MS Excel 2016 program, the Visual Basic for Applications (VBA) methodology has been instrumental in obviating the necessity for the expert to carry physical documents and a camera simultaneously. This technological integration streamlines field operations, enabling the expert to conduct assessments with enhanced ease and efficiency, carrying only a tablet.

REFERENCES

1. Bejinariu, C., Darabont, D. C., Burduhos-N., D. P., Cazac, A. M., & Chiriac-Moruzzi, C. (2023). Considerations regarding the application of the occupational injury and illness risk assessment method at workplaces/workstations, in relation to the ISO 45001 Standard. *Sustainability*, 15(3), 2121.
2. Derin, H., & Şahin, L. (2022). Inspection in terms of occupational health and safety in Turkey, an evaluation of the years 2010-2018. *Social Science Development Journal*. 7(33), 516-526. <http://dx.doi.org/10.31567/ssd.745>
3. Dinkçi, Ö., & Akpınar, T. (2023). Evaluation of labor inspection in Türkiye in the context of occupational health and safety). *Balkan & Near Eastern Journal of Social Sciences (BNEJSS)*, 9(3).
4. Ersoy, H. H. T. (2022). Occupational health and safety of domestic workers in Türkiye. *Yıldırım Beyazıt Law Journal*, 1545-1586.
5. Ersoy, S., & Kaya, E. Ç. (2019). A public university food engineering laboratories risk analysis application. *Gümüşhane University Journal of Health Sciences*, 8(4), 411-423.
6. İncekara, Ç. Ö. (2020). Occupational health and safety management system in a business operating in the energy sector. *Mehmet Akif Ersoy University Journal of Applied Sciences*, 4(1), 152-177.
7. Karahmetoğlu, A. (2022). Basic dynamics and application area of the occupational health and safety system in the Republic of Türkiye. *International Western Black Sea Journal of Social Sciences and Humanities*, 6(2), 123-147.
8. Lafçı, Ö., & Öztekin, A. (2020). Risk assessment of sea rescue activities on search/rescue ships using L type matrix method. *Journal Home-Page*, 3(2), 66-78.
9. Oturakci, M., & Dağsuyu, C. (2017). Fuzzy fine-kinney method and its application in risk assessment. scholar.archive.org
10. Öztürk, Z. K., Güngör, K., & Lepki, B. (2016). A decision support system for multi-purpose door assignment problems in the logistics industry. *Journal of Engineering Sciences and Design*, 4(1), 21-29.
11. Tedonchio, C. T., Nadeau, S., Botton, C., & Rivest, L. (2022). Digital mock-ups as support tools for preventing risks related to energy sources in the operation stage of industrial facilities through design. *Results in Engineering*, 16, 100690
12. Türker, M. ve Kanit R. (2020). Prediction of the severity of occupational accidents in the building production process with the pre-informed artificial learning method, *Konya Journal of Engineering Sciences*, 8(4) 943-956, doi:10.36306/konjes.764952

13. Ulu, Ö. G. M., & Arısoy, Ö. G. B. (2024). Evaluation of employees who require special policies in terms of occupational health and safety. *Journal of Health and Social Welfare Research*, 4(1), 113-125.
14. Uluskan, M., & Yusuf, B. Ö. C. Ü. (2020). Risk analysis review and decision support system design for calibration periods of measuring devices. *Eskişehir Osmangazi University Faculty of Engineering and Architecture Journal*, 28(2), 174-193.
15. Usanmaz, D., & Ercan, K. Ö. S. E. (2020). Statistical analysis of two different methods for chemical research laboratory risk assessment. *International Journal of Engineering Research and Development*, 12(2), 337-348.
16. Yemişçioğlu, Ş., & Şimşek, Z. (2023). Evaluation of a student dormitory in terms of fire risk using the L-type matrix method. *Journal of Dicle University Institute of Science and Technology*, 12(2), 251-267.
17. <https://ilostat.ilo.org/topics/safety-and-health-at-work>
18. <https://safetyculture.com/topics/risk-assessment/>



DERIVATION OF COX-VOINOV EQUATION ANALITICALLY FOR THIN LIQUID FILM ON A FLAT SUBSTRATE

Aslı TİKTAŞ¹

¹ Araştırma Görevlisi, Kırşehir Ahievran Üniversitesi, asli.tiktas@ahievran.edu.tr,

ORCID No: 0000-0003-3685-5134

1.DERIVATION of COX-VOINOV EQUATION ANALYTICALLY

1.1. Problem Description and Using Lubrication Equations

We evaluate thin liquid film on a flat substrate in a two dimensional Cartesian coordinate system of x and y which represents locations of parallel and perpendicular to flat substrate, respectively. Also in this configuration configuration velocity components in x and y direction, density of the liquid, viscosity of the liquid, surface tension of the liquid is denoted as $u(y)$, $v(x)$, ρ , μ , γ , respectively and we assume that precursor film approximation or else which remove singularity problems is not used. Because height of thin film is bigger than 100 nanometer, so if we use no slip condition at the substrate and no-shear stress condition at liquid-air interface, singularity problems can be neglect due to 100 nanometer thin film height is needed for formation of effective intermolecular attractions which cause singularity problems such as van der Waals forces.

We can use mass conservation equation and Navier-Stokes equation both in x direction from the fluid mechanics. These equations are:

$\frac{\partial \rho}{\partial t_*} + \rho \left(\frac{\partial u_*}{\partial x_*} + \frac{\partial v_*}{\partial y_*} \right) = 0$	(1.1.1)
$\rho \left(\frac{\partial u_*}{\partial t_*} + \frac{\partial u_*}{\partial x_*} u_* + \frac{\partial u_*}{\partial y_*} v_* \right) = - \frac{\partial p_*}{\partial x_*} + \rho g_x + \mu \left(\frac{\partial^2 u_*}{\partial x_*^2} + \frac{\partial^2 u_*}{\partial y_*^2} \right)$	(1.1.2)

In these equations, star terms express dimensional variables and if we want to obtain nondimensional form of these equations, we must use relation of dimensional and nondimensional variables with proper length, velocity and pressure scales. This relation can be expressed in that:

$x_* = xx_s$	(1.1.3)
$u_* = uu_s$	(1.1.4)
$p_* = pp_s$	(1.1.5)
$t_* = tt_s = t \frac{x_s}{u_s}$	(1.1.6)

where subscript s expresses scales for length, velocity and pressure, nondimensional variables defined as not included any subscript. If we put these terms into the equation (1.2), we obtained these equations:

$\rho \left(\frac{\partial(uu_s)}{\partial(tt_s)} + \frac{\partial(uu_s)}{\partial(xx_s)}uu_s + \frac{\partial(uu_s)}{\partial(yy_s)}vv_s \right) = -\frac{\partial(pp_s)}{\partial(xx_s)} + \rho g_x + \mu \left(\frac{\partial^2(uu_s)}{\partial(x^2 x_s^2)} + \frac{\partial^2(uu_s)}{\partial(y^2 y_s^2)} \right)$	(1.1.7)
$\left(\frac{\partial(uu_s)}{\partial(tt_s)} + \frac{\partial(uu_s)}{\partial(xx_s)}uu_s + \frac{\partial(uu_s)}{\partial(yy_s)}vv_s \right) = -\frac{1}{\rho} \frac{\partial(pp_s)}{\partial(xx_s)} + g_x + \nu \left(\frac{\partial^2(uu_s)}{\partial(x^2 x_s^2)} + \frac{\partial^2(uu_s)}{\partial(y^2 y_s^2)} \right)$	(1.1.8)

where ν is the kinematic viscosity of the fluid..

$\frac{\partial u}{\partial t} \frac{u_s}{x_s} + \frac{\partial u}{\partial x} u \frac{u_s^2}{x_s} + \frac{\partial u}{\partial y} v \frac{u_s v_s}{y_s} = -\frac{1}{\rho} \frac{p_s}{x_s} \frac{\partial p}{\partial x} + g_x + \nu \left(\frac{\partial^2 u}{\partial x^2} \frac{u_s}{x_s^2} + \frac{\partial^2 u}{\partial y^2} \frac{u_s}{y_s^2} \right)$	(1.1.9)
$\left(\frac{\partial u}{\partial t} + \frac{\partial u}{\partial x} u + \frac{\partial u}{\partial y} v \frac{v_s x_s}{u_s y_s} \right) = -\frac{1}{\rho} \frac{p_s}{u_s^2} \frac{\partial p}{\partial x} + g_x \frac{x_s}{u_s^2} + \frac{\nu}{x_s u_s} \frac{x_s^2}{y_s^2} \left(\frac{\partial^2 u}{\partial x^2} \frac{y_s^2}{x_s^2} + \frac{\partial^2 u}{\partial y^2} \right)$	(1.1.10)

In equation (1.10), term of $\frac{\nu}{x_s u_s}$ can be defined as inverse of the

Reynolds number. This number is a dimensionless number and proportion of inertial forces to viscous forces. We can represent these forces for this model problem in that:

$F_i = \rho \frac{du}{dt} \cong \rho \frac{u}{x} \cong \rho \frac{u^2}{x}$	(1.1.11)
--	----------

where u is the characteristic droplet velocity, x is the characteristic droplet length and F_i is the representative inertial force.

$F_v = \mu \nabla^2 u \cong \mu \frac{u}{x^2}$	(1.1.12)
--	----------

where F_v is the representative viscous force. So, if we divide inertial force to viscous force, we obtain Reynolds number:

$\text{Re} = \frac{F_i}{F_v} \cong \frac{\rho \frac{u^2}{x}}{\mu \frac{u}{x^2}} \cong \frac{\rho u x}{\mu}$	(1.1.13)
---	----------

Also we can create special assumptions for this model problem, for example smaller characteristic film length and velocity. So there not exist any effect in order to change of the total derivative of characteristic thin film velocity and Reynolds number is small due to smaller velocity and length scales, also we can neglect inertial forces and viscous forces becomes main effective forces for this model problem. If we multiply all sides

of equation (1.1.10) with $\text{Re} \frac{y_s^2}{x_s^2}$, we obtained these equations:

$\text{Re} \frac{y_s^2}{x_s^2} \left(\frac{\partial u}{\partial t} + \frac{\partial u}{\partial x} u + \frac{\partial u}{\partial y} v \frac{y_s}{u_s} \frac{x_s}{y_s} \right) = -\frac{1}{\rho} \frac{p_s y_s^2}{v x_s u_s} \frac{\partial p}{\partial x} + g_x \frac{y_s^2}{u_s v} + \left(\frac{\partial^2 u}{\partial x^2} \frac{y_s^2}{x_s^2} + \frac{\partial^2 u}{\partial y^2} \right)$	(1.1.14)
---	----------

Also in this model problem streamlines parallel to x direction and velocity component of perpendicular direction of flow is much smaller than parallel direction of the flow. Similar situation is valid for length size. So ratio of y length size to x length size becomes smaller. So we can neglect these terms and we modify to equation (1.1.14) according to this:

$-\frac{p_s y_s^2}{\mu x_s u_s} \frac{\partial p}{\partial x} + g_x \frac{y_s^2}{u_s v} + \frac{\partial^2 u}{\partial y^2} = 0$	(1.1.15)
--	----------

Also we can determine pressure scale from the equation (1.1.15) by satisfying nonlinearization in that:

$\frac{p_s y_s^2}{x_s u_s \mu} = 1$	(1.1.16)
$p_s = \frac{x_s u_s \mu}{y_s^2}$	(1.1.17)

If we put these term into the equation (1.1.15), we obtain nondimensional form of the equation (1.1.2):

$-\frac{\partial p}{\partial x} + g_x \frac{y_s^2}{u_s \nu} + \frac{\partial^2 u}{\partial y^2} = 0$	(1.1.18)
--	----------

and if we want to obtain dimensional form of equation (1.1.18), we must use relation of dimensional and nondimensional variables in that:

$x = \frac{x_*}{x_s}$	(1.1.19)
$y = \frac{y_*}{y_s}$	(1.1.20)
$p = \frac{p_*}{p_s}$	(1.1.21)
$u = \frac{u_*}{u_s}$	(1.1.22)

If we put these terms into the equation (1.1.18), we obtain these equations:

$-\frac{\partial \left(\frac{p_*}{p_s} \right)}{\partial \left(\frac{x_*}{x_s} \right)} + g_x \frac{y_s^2}{u_s \nu} + \frac{\partial^2 \left(\frac{u_*}{u_s} \right)}{\partial \left(\frac{y_*^2}{y_s^2} \right)} = 0$	(1.1.23)
$-\frac{\partial p_*}{\partial x_*} + g_x \rho + \mu \frac{\partial^2 u_*}{\partial y_*^2} = 0$	(1.1.24)

So, equation (1.1.2) is converted to equation (1.1.24) by using dimensional analysis and assumptions and similarly if we put relation equation of dimensional and nondimensional variables into the equation (1.1.1), we obtained these equations:

$\frac{\partial \rho}{\partial (tt_s)} + \rho \left(\frac{\partial (uu_s)}{\partial (xx_s)} + \frac{\partial (vv_s)}{\partial (yy_s)} \right) = 0$	(1.1.25)
---	----------

$\frac{u_s}{x_s} \left(\frac{\partial \rho}{\partial t} + \rho \frac{\partial u}{\partial x} + \rho \frac{x_s}{u_s} \frac{v_s}{y_s} \frac{\partial v}{\partial y} \right) = 0$	(1.1.26)
---	----------

We assume that fluid is incompressible and Newtonian, so density of the fluid does not change and if we use this information into the equation (1.1.26), we obtain these equations:

$\rho \left(\frac{\partial u}{\partial x} + \frac{x_s}{u_s} \frac{v_s}{y_s} \frac{\partial v}{\partial y} \right) = 0$	(1.1.27)
---	----------

$\left(\frac{\partial u}{\partial x} + \frac{x_s}{u_s} \frac{v_s}{y_s} \frac{\partial v}{\partial y} \right) = 0$	(1.1.28)
--	----------

$\frac{x_s}{u_s} \frac{v_s}{y_s} = 1$	(1.1.29)
---------------------------------------	----------

$\left(\frac{\partial u}{\partial x} + \frac{x_s}{u_s} \frac{v_s}{y_s} \frac{\partial v}{\partial y} \right) = 0$	(1.1.30)
--	----------

If we put equation (1.1.30) into the equation (1.1.29), we obtain non-dimensional form of equation (1.1.1),

$\left(\frac{\partial u}{\partial x} + \frac{\partial v}{\partial y} \right) = 0$	(1.1.31)
--	----------

and if we want to obtain dimensional form of equation (1.1.31), we must use relation of dimensional and nondimensional variables and if we put these terms into the equation (1.1.31), we obtain these equations:

$\frac{\partial \left(\frac{u_*}{u_s} \right)}{\partial \left(\frac{x_*}{x_s} \right)} + \frac{\partial \left(\frac{v_*}{v_s} \right)}{\partial \left(\frac{y_*}{y_s} \right)} = 0$	(1.1.32)
$\frac{x_s}{u_s} \frac{\partial u_*}{\partial x_*} + \frac{y_s}{v_s} \frac{\partial v_*}{\partial y_*} = 0$	(1.1.33)

If we multiply to all sides of equation (1.1.33) with $\frac{v_s}{y_s}$ and use equation (1.1.31) , we obtain these equations:

$\frac{x_s}{u_s} \frac{v_s}{y_s} \frac{\partial u_*}{\partial x_*} + \frac{y_s}{v_s} \frac{v_s}{y_s} \frac{\partial v_*}{\partial y_*} = 0$	(1.1.34)
$\frac{\partial u_*}{\partial x_*} + \frac{\partial v_*}{\partial y_*} = 0$	(1.1.35)

So equation (1.1.1) is converted to equation (1.1.35) and our new governing equations becomes continuity equation and lubrication equations both in x direction, which are:

$\frac{\partial u_*}{\partial x_*} + \frac{\partial v_*}{\partial y_*} = 0$	(1.1.36)
$-\frac{\partial p_*}{\partial x_*} + g_x \rho + \mu \frac{\partial^2 u_*}{\partial y_*^2} = 0$	(1.1.37)

Also we know that $g_x = 0$, so these equation (1.1.37) convert to:

$\frac{\partial p_*}{\partial x_*} = \mu \frac{\partial^2 u_*}{\partial y_*^2}$	(1.1.38)
---	----------

1.2. Obtaining Velocity Profile and Volumetric Flow Rate Per Unit Depth

We can obtain velocity profile of thin film by integrate to equation (1.1.38) twice with respect to y .

$$\frac{\partial^2 u}{\partial y^2} = \frac{\partial}{\partial y} \left(\frac{\partial u}{\partial y} \right) = \frac{1}{\mu} \frac{\partial p}{\partial x} \quad (1.2.1)$$

$$u(y) = \frac{1}{\mu} \frac{\partial p}{\partial x} \frac{y^2}{2} + c_1 y + c_2 \quad (1.2.2)$$

where c_1 and c_2 are integration constants which can be determined from boundary conditions for velocity. We can use no-slip and no-shear stress boundary conditions.

$$u(y) = 0 \text{ at } y=0 \quad (1.2.3)$$

$$\frac{\partial u}{\partial y} = 0 \text{ at } y = h \quad (1.2.4)$$

$$c_2 = 0 \quad (1.2.5)$$

$$\frac{1}{\mu} \frac{\partial p}{\partial x} h + c_1 = 0 \quad (1.2.6)$$

$$c_1 = -\frac{1}{\mu} \frac{\partial p}{\partial x} h \quad (1.2.7)$$

$$u(y) = \frac{1}{\mu} \frac{\partial p}{\partial x} \frac{y^2}{2} - \frac{1}{\mu} \frac{\partial p}{\partial x} h y = \frac{1}{\mu} \frac{\partial p}{\partial x} y \left(\frac{y}{2} - h \right) \quad (1.2.8)$$

Also we can determine volumetric flow rate per unit depth by integrating velocity profile with respect to y from substrate to liquid-air interface.

$q = \int_0^h u(y) dy = \left[\frac{1}{\mu} \frac{\partial p}{\partial x} \frac{y^2}{2} - \frac{1}{\mu} \frac{\partial p}{\partial x} hy \right] dy$	(1.2.9)
$q = \frac{1}{\mu} \frac{\partial p}{\partial x} \frac{h^3}{6} - \frac{1}{\mu} \frac{\partial p}{\partial x} \frac{h^3}{2} = -\frac{1}{3\mu} \frac{\partial p}{\partial x} h^3$	(1.2.10)

1.3. Relating Capillary Pressure Isotherm and Curvature of Thin Film Surface

We can define liquid-air interface and we can express pressure term in equation (1.2.10) in terms of curvature of the thin film by defining outward normal vector of the thin film surface in that:

$\mathbf{n} = \frac{\nabla(y-h)}{ \nabla(y-h) }$	(1.3.1)
--	---------

where \mathbf{n} is the outward normal vector. Also we can express capillar pressure term in terms of curvature of the thin film surface with neglecting disjoining pressure isotherm in that:

$p^L - p^A = -\gamma \nabla \mathbf{g} \mathbf{n}$	(1.3.2)
$\nabla(y-h) = \left(\frac{\partial}{\partial x} \mathbf{i} + \frac{\partial}{\partial y} \mathbf{j} \right) (y-h)$	(1.3.3)
$\nabla(y-h) = \frac{\partial y}{\partial x} \mathbf{i} - \frac{\partial h}{\partial x} \mathbf{i} + \frac{\partial y}{\partial y} \mathbf{j} - \frac{\partial h}{\partial y} \mathbf{j}$	(1.3.4)

In this equation we know that the liquid-air interface vary with only x location and time, so we apply this information to in this equation, we obtain these equations:

$\nabla(y-h) = -\frac{\partial h}{\partial x} \mathbf{i} + \mathbf{j}$	(1.3.5)
--	---------

and norm of this curl term equates to:

$ \nabla(y-h) = \sqrt{\left(\frac{\partial h}{\partial x}\right)^2 + 1}$	(1.3.6)
---	---------

So, unit normal vector equates to:

$\mathbf{n} = \frac{\mathbf{j} - \frac{\partial h}{\partial x} \mathbf{i}}{\sqrt{1 + \left(\frac{\partial h}{\partial x}\right)^2}}$	(1.3.7)
--	---------

if we apply dot product of this term and nabla, we obtain these results:

$\nabla \mathbf{g} = \left(\frac{\partial}{\partial x} \mathbf{i} + \frac{\partial}{\partial y} \mathbf{j} \right) \cdot \mathbf{g} \left(\frac{-\frac{\partial h}{\partial x}}{\sqrt{1 + \left(\frac{\partial h}{\partial x}\right)^2}} \mathbf{i} + \frac{1}{\sqrt{1 + \left(\frac{\partial h}{\partial x}\right)^2}} \mathbf{j} \right)$	(1.3.8)
$\nabla \mathbf{g} = \frac{\partial}{\partial x} \left(\frac{-\frac{\partial h}{\partial x}}{\sqrt{1 + \left(\frac{\partial h}{\partial x}\right)^2}} \right) + \frac{\partial}{\partial y} \left(\frac{1}{\sqrt{1 + \left(\frac{\partial h}{\partial x}\right)^2}} \right)$	(1.3.9)

In this equation second term of the right hand side equates to zero because upper boundary of the interface vary with only x location and time.

$\nabla \mathbf{g} = \frac{\partial}{\partial x} \left(\frac{-\frac{\partial h}{\partial x}}{\sqrt{1 + \left(\frac{\partial h}{\partial x}\right)^2}} \right) = -\frac{\partial^2 h}{\partial x^2} \sqrt{1 + \left(\frac{\partial h}{\partial x}\right)^2} + \frac{1}{2} \left(1 + \left(\frac{\partial h}{\partial x}\right)^2 \right)^{-3/2} \frac{\partial h}{\partial x}$	(1.3.10)
---	----------

If we assume thin liquid film surface has a small slope, so we can modify to this equation in that:

$\frac{\partial h}{\partial x} \rightarrow 0$	(1.3.11)
$\nabla \mathbf{g} = -\frac{\partial^2 h}{\partial x^2}$	(1.3.12)
$p^L - p^A = \gamma \frac{\partial h}{\partial x}$	(1.3.13)
$\frac{\partial p}{\partial x} = \gamma \frac{\partial^3 h}{\partial x^3}$	(1.3.14)
$q = -\frac{1}{3\mu} \frac{\partial p}{\partial x} h^3 = -\frac{1}{3\mu} \gamma \frac{\partial^3 h}{\partial x^3} h^3$	(1.3.15)

1.4. Analytical Solution of Governing Equations and Relating This Solutions with Cox-Voinov Equation

This volumetric flow rate also equal to product of velocity of the thin film and cross sectional area of the flow for per unit depth from the mass conservation in that:

$q = -\frac{1}{3\mu} \frac{\partial p}{\partial x} h^3 = -\frac{1}{3\mu} \gamma \frac{\partial^3 h}{\partial x^3} h^3$	(1.4.1)
--	---------

$q = -\frac{1}{3\mu} \frac{\partial p}{\partial x} h^3 = -\frac{1}{3\mu} \gamma \frac{\partial^3 h}{\partial x^3} h^3 = uh$	(1.4.2)
$\frac{u\mu}{\gamma} h = \frac{h^3}{3\mu} \mu \frac{\gamma}{\gamma} \frac{\partial^3 h}{\partial x^3}$	(1.4.3)
$Ca = \frac{u\mu}{\gamma}$	(1.4.4)

where Ca is the capillary number and this number is proportion of viscous forces to surface tension forces.

$3Cah = h^3 \frac{\partial^3 h}{\partial x^3}$	(1.4.5)
$\frac{\partial^3 h}{\partial x^3} = \frac{3Ca}{h^2}$	(1.4.6)
$h(x) = x\theta(x)$	(1.4.7)

If we assume that dynamic contact angle vary with x slowly and we can neglect derivative terms.

$h'(x) = \theta(x)$	(1.4.8)
$h''(x) = \theta'(x)$	(1.4.9)
$h'''(x) = \theta''(x)$	(1.4.10)

If we put these terms into equation (1.4.6), we obtain this equation:

$\theta'' = \frac{3Ca}{x^2 \theta^2}$	(1.4.11)
$\theta'' \theta^2 = \frac{3Ca}{x^2}$	(1.4.12)

Solution of this equation involves relation of capillary number and dynamic contact angle and Cox&Voinov [1] developed an approximate solution by considering singularity. We consider a curved liquid-air interface and singularity of the substrate at the dynamic contact angle variation with calculating viscous dissipation term and balancing this term product of velocity of the contact line and dynamic force at the contact line from the force balance approach. We can explain origin of the viscous dissipation term briefly. Firstly, we can write Navier-Stokes equations for thin liquid film in that:

$\rho \left(\frac{\partial u}{\partial t} + \frac{\partial u}{\partial x} u + \frac{\partial u}{\partial y} v \right) = -\frac{\partial p}{\partial x} + \left[\frac{\partial}{\partial x} \tau_{xx} + \frac{\partial}{\partial y} \tau_{yx} \right]$	(1.4.12)
---	----------

where τ is stress tensor and can be expressed from constitutive laws from the fluids in that:

$\tau_{ij} = \mu \frac{1}{2} \left(\frac{\partial u_i}{\partial x_j} \right)$	(1.4.13)
--	----------

and we can express viscous force per unit volume from the equation (1.4.12) in that:

$F_{v,i} = \frac{\partial \tau_{ji}}{\partial x_j}$	(1.4.14)
---	----------

Also work rate done by viscosity which is the summation of reduction of the rate of mechanical energy due to frictional forces and work rate done on the fluid body due to acceleration of the surrounding fluids due to frictional forces. This term can be expressed as surface integral of product of the the stress tensor and velocity component in that:

$\frac{dW}{dt} = \iint u_i \tau_{ji} dS_j$	(1.4.15)
--	----------

Volume integral can obtained from this surface integral by enforcing can be converted to volume integral by applying Gauss divergence theorem in that:

They define viscous dissipation term due to effective viscous forces in that

$\frac{dW}{dt} = \iint u_i \tau_{ji} dS_j = \int_V \text{div}(u_i \tau_{ji}) dV$	(1.4.16)
$\frac{dW}{dt} = \int_V \text{div}(u_i \tau_{ji}) dV = \int_V \frac{\partial}{\partial x_j} (u_i \tau_{ji}) dV = \int_V \left(\frac{\partial \tau_{ji}}{\partial x_j} u_i + \tau_{ji} \frac{\partial u_i}{\partial x_j} \right) dV$	(1.4.17)

Reduction rate of mechanical energy term is $\int_V \tau_{ji} \frac{\partial u_i}{\partial x_j} dV$ in equation (1.4.17) and if we evaluate this term, we obtain these equations:

$\int_V \tau_{ji} \frac{\partial u_i}{\partial x_j} dV = \int_V \frac{1}{2} (\tau_{ji} + \tau_{ij}) \frac{\partial u_i}{\partial x_j} dV$	(1.4.18)
$\int_V \tau_{ji} \frac{\partial u_i}{\partial x_j} dV = \int_V \frac{1}{2} \left[\tau_{ij} \frac{\partial u_i}{\partial x_j} + \tau_{ji} \frac{\partial u_i}{\partial x_j} \right] dV$	(1.4.19)
$\int_V \tau_{ji} \frac{\partial u_i}{\partial x_j} dV = \int_V \frac{1}{2} \left[\tau_{ij} \frac{\partial u_i}{\partial x_j} + \tau_{ij} \frac{\partial u_j}{\partial x_i} \right] dV$	(1.4.20)
$\int_V \tau_{ji} \frac{\partial u_i}{\partial x_j} dV = \int_V \frac{1}{2} \tau_{ij} \left(\frac{\partial u_j}{\partial x_i} + \frac{\partial u_i}{\partial x_j} \right) dV = \int_V \mu \left(\frac{\partial u_i}{\partial x_j} \right) \left(\frac{\partial u_i}{\partial x_j} \right) dV$	(1.4.21)
$\int_V \tau_{ji} \frac{\partial u_i}{\partial x_j} dV = \int_V \mu \left(\frac{\partial u_i}{\partial x_j} \right)^2 dV$	(1.4.22)

This viscous dissipation term can be simplified for thin liquid film problem in that:

$\int_V \tau_{ji} \frac{\partial u_i}{\partial x_j} dV = \int_V \mu \left(\frac{\partial u_i}{\partial x_j} \right)^2 dV = \int_0^\infty dx \int_0^h \mu \left(\frac{\partial u}{\partial y} \right)^2 dy$	(1.4.23)
--	----------

In this equation we assume that if x location approaches to infinity,

there exists singularity problem at calculating $\frac{\partial u_i}{\partial x_j}$ term and we attempt to removing this problem a simple way in that:

$\int_0^\infty dx \int_0^h \mu \left(\frac{\partial u}{\partial y} \right)^2 dy = \int_0^\infty dx \int_0^h \left(\frac{u}{h} \right)^2 dy$	(1.4.24)
---	----------

In this equation we assume that term of $\frac{\partial u}{\partial y}$ is equal to proportion of constant contact line velocity to thin film thickness.

$\int_0^\infty dx \int_0^h \mu \left(\frac{\partial u}{\partial y} \right)^2 dy = \int_0^\infty dx \int_0^h \left(\frac{u}{h} \right)^2 dy = \int_0^\infty dx \mu u^2 \int_0^h h^{-2} dy \quad (1.4.25)$
$\int_0^\infty dx \int_0^h \mu \left(\frac{\partial u}{\partial y} \right)^2 dy = \int_0^\infty dx \int_0^h \left(\frac{u}{h} \right)^2 dy = \int_0^\infty dx \mu u^2 \frac{1}{h^2} h = \int_0^\infty dx \frac{\mu u^2}{h} \quad (1.4.26)$

Also if we assume that

$h = x\theta \quad (1.4.27)$

So, equation (1.4.26) can be converted to this equation

$\int_0^\infty dx \int_0^h \mu \left(\frac{\partial u}{\partial y} \right)^2 dy = \int_0^\infty dx \int_0^h \left(\frac{u}{h} \right)^2 dy = \int_0^\infty dx \mu u^2 \frac{1}{h^2} h = \int_0^\infty dx \frac{\mu u^2}{x\theta} = \frac{\mu u^2}{\theta} \int_0^\infty \frac{dx}{x} \quad (1.4.28)$
--

So, right hand side integral requires a cutoff molecular scale length which is order of 10^{-9} and capillary length which is order of 10^{-3} in order to removing singularity problem.

$\int_0^\infty \frac{dx}{x} = \int_a^L \frac{dx}{x} = \ln \left(\frac{L}{a} \right) \quad (1.4.29)$
--

where L is the capillary length and a is the molecular scale length. So, equation (1.4.23) can be converted to this equation:

$\int_V \mathcal{N}_{ji}^* \frac{\partial u_i}{\partial x_j} dV \approx \int_V \left(\frac{\partial u_i}{\partial x_j} \right)^2 dV \int_0^\infty dx \int_0^h \left(\frac{\partial \ddot{u}}{\partial y} \right)^2 dy \frac{\mu}{\theta} \ln \left(\frac{L}{a} \right) \quad (1.4.30)$

Also if we equate viscous dissipation term to product of dynamic force which act on the contact line from the force balance approach at the three phase contact line and velocity of the contact line. Firstly, we can consider dynamic force.

$F = \gamma_{SA} - \gamma_{SL} - \gamma_{LA} \cos \theta_d \quad (1.4.31)$
--

where θ_d is the dynamic contact angle and, γ_{SA} , γ_{SL} and γ_{LA} are surface tension of the solid-air, solid-liquid, liquid-air interfaces respectively. We assume that these surface tensions are remain constant, so dynamic

force is constitute of only term of $\gamma_{LA} \cos \theta_d$.

$F_d = \gamma_{LA} \cos \theta_d$	(1.4.32)
-----------------------------------	----------

where F_d is the dynamic component of the force.

$F_d u = \int_V \tau_{ji} \frac{\partial u_i}{\partial x_j} dV$	(1.4.33)
$\gamma_{LA} \cos \theta_d u = \frac{\mu u^2}{\theta} \ln \left(\frac{L}{a} \right)$	(1.4.34)

Also in this equation we can express \cos term in a simple way by using Taylor expansion with neglecting small order terms in that:

$\cos \theta_d = 1 - \frac{\theta_d^2}{2}$	(1.4.35)
$\gamma_{LA} 1 - \frac{\theta_d^2}{2} u = \frac{\mu u^2}{\theta} \ln \left(\frac{L}{a} \right)$	(1.4.36)
$\gamma_{LA} 1 - \frac{\theta_d^2}{2} = \frac{\mu u}{\theta} \ln \left(\frac{L}{a} \right)$	(1.4.37)
$u = \frac{\gamma_{LA}}{\mu \ln \left(\frac{L}{a} \right)} \theta_d \left(1 - \frac{\theta_d^2}{2} \right) \approx \frac{\gamma_{LA}}{\mu \ln \left(\frac{L}{a} \right)} \frac{\theta_d^3}{2}$	(1.4.38)
$Ca = \frac{\mu u}{\gamma_{LA}}$	(1.4.39)
$Ca = \frac{\gamma}{\mu \ln \left(\frac{L}{a} \right)} \frac{\mu}{\gamma} \frac{1}{2} \theta_d^3$	(1.4.40)

$$\frac{\gamma}{\mu \ln\left(\frac{L}{a}\right)} \frac{\mu}{\gamma} \frac{1}{2} = \text{constant} \quad (1.4.41)$$

$$Ca = \theta_d^3 \text{constant} \quad (1.4.42)$$

So, this relation implies that there exists a linear variation of cube of the dynamic contact angle and capillary number.

2. REFERENCES

- [1] R. G. Cox, “The dynamics of the spreading of liquids on a solid surface. Part 1. Viscous flow,” *J. Fluid Mech.*, 1986.



3D MODELING AND SIMULATION OF A RELUCTANCE COIL GUN

Vekil SARI¹

¹ 1 Asst. Prof.; Sivas Cumhuriyet University, Faculty of Engineering, Department of Electrical and Electronics Engineering, 58140, Sivas, Türkiye; e-mail: vsari@cumhuriyet.edu.tr; ORCID: <https://orcid.org/0000-0001-5963-0179>

1. INTRODUCTION

Today, chemical explosives are used to launch projectiles, rockets and spacecraft. There are some limitations in increasing the speed of these systems. Chemical fuels cannot be reused, so their costs are high. Storage of chemical fuels is dangerous and the chemical reaction is difficult to control. Electromagnetic launchers have been discovered as an alternative to chemical launcher systems (Fair, 1982). The importance of electromagnetic launchers has increased recently due to their many advantages such as high speed, reusability, flexibility and durability. Numerous industries, including the military, nuclear physics, space exploration, and medicine, use electromagnetic launchers..

1.1. Types of Electromagnetic Launchers

There are many types of launchers. Some of these are electromagnetic (EM), chemical, hydrostatic, elastic and gravity. Electromagnetic launchers (EML) can be classified as induction, direct, electro-thermal-chemical (ETC), magnetic, electrostatic and hybrid. This classification is shown in Figure 1.

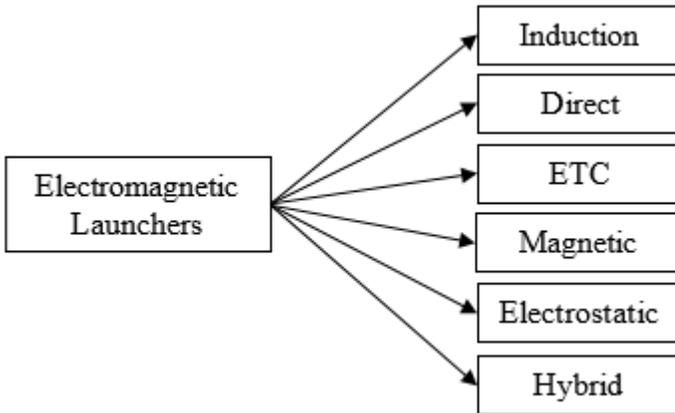


Figure 1. *Classification of Electromagnetic Launchers.*

Rail launchers (RAL) and reluctance launchers (REL) are the most studied EML. RAL are the constant specific force type of the direct class. REL are the variable specific force type of the direct class (Engel, 2017).

1.1.1. Rail Launchers (Rail Gun)

There are typically three different types of RAL based on rail structure: conventional RAL, augmented RAL, and barrel-fed RAL (Yu and Fan, 2010). The most commonly used conventional RAL have two rails and a movable conductive armature that short-circuits these rails. When voltage

is applied to the rails, the conductive armature short-circuits the rails and a current flows through the rails. This current produces a magnetic field. The armature moves with the Lorentz force that occurs as a result of the magnetic field and throws the object to be thrown (Keshtkar et al., 2008).

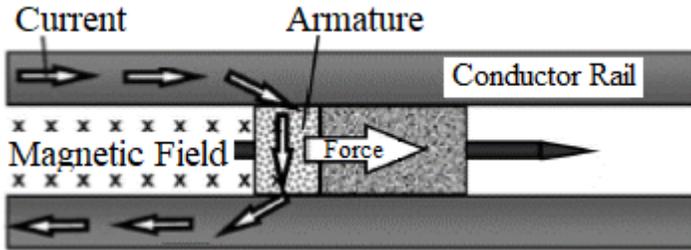


Figure 2. Rail gun.

RAL can reach high speeds (higher than 2000 m/s) and their efficiency can exceed 30% (Lehmann et al., 2006). RAL are large in size. For this reason, it is not portable and must be mounted on a fixed place or vehicle. RAL are mostly suitable for use in land and sea vehicles. The representation of the RAL, also known as the rail gun (Tzeng and Schmidt, 2010), is shown in Figure 2, and the equivalent circuit of the RAL (Zhang et al., 2010) is shown in Figure 3.

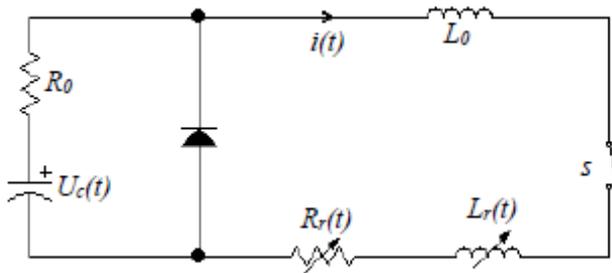


Figure 3. Equivalent circuit of rail gun.

1.1.2. Coil Launchers (Coil Gun)

Another name for coil launchers (CL) is coil gun (CG). In CG, coils are used to launch the object to be thrown. CG may have one coil or multiple coils (Marder, 1993). CG consist of two main parts; mechanical part and electronic part. The mechanical section consists of three subsections.

1. Winding
2. Barrel (the pipe through which the object to be thrown will move)
3. Projectile (The object to be thrown)

In the electronic part, there are power supply and control circuits. When a current flows through the winding, a magnetic field is created around the winding. The object to be thrown is thrown with the effect of this magnetic field. CG can be generally divided into induction coil guns (ICG) and reluctance coil guns (RCG) (Daldaban and Sari, 2016). There are also electromagnetic launchers where induction and REL are used together (Jing et al., 2017).

1.1.2.1. Induction Coil Gun

The projectile launched in ICG is not ferromagnetic, but paramagnetic or diamagnetic. The projectile is not pulled, it is pushed. Therefore, the projectile must stay outside the part of the coil that is intended to be launched. The operation of ICG is related to eddy currents (Slade, 2005). Figure 4 shows the ICG, and Figure 5 shows the equivalent circuit of the ICG.

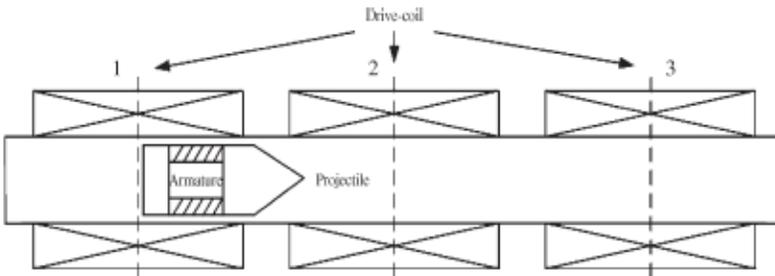


Figure 4. Induction coil gun (Liu et al., 2010).

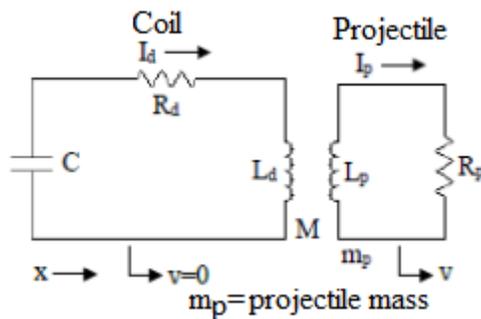


Figure 5. Equivalent circuit of induction coil gun (McKinney and Mongeau, 1984).

1.1.2.2. Reluctance Coil Gun

The operation principle of RCG is similar to reluctance motors (ChaoWei et al., 2008). The projectile to be launched in RCG must be made of ferromagnetic material. The projectile is moved toward middle of the coil by RCG. The projectile cannot be pushed. (Mosallanejad and Shoulaie, 2012). When current flows through the coil, a magnetic field is created. This magnetic field wants to use the projectile as a bridge (due to the magnetic permeability of the ferromagnetic projectile being much higher than air) and therefore pulls the projectile towards the center of the coil. The coil's energy should be cut off and the coil's energy should be absorbed when projectile reaches the middle of the coil. Otherwise, the projectile cannot be thrown or it will be thrown slowly because the projectile will be pulled in the opposite direction and again to the center of the coil. This is the most important point in the design of RCG. The efficiency of the RCG is very dependent on this timing. In multi-stage RCG, energy must be given to the relevant coil according to the position of the projectile, and when the projectile reaches the center of that coil, the energy of that coil must be cut off and the energy in that coil must be absorbed. Sensors can be used to energize and disconnect the coils. These sensors are shown in Figure 6 (Daldaban and Sari, 2014). After the coil is de-energized, a parallel diode can be connected to absorb the energy in the coil. This parallel diode is shown in Figure 7 (Bresie and Andrews, 1991).

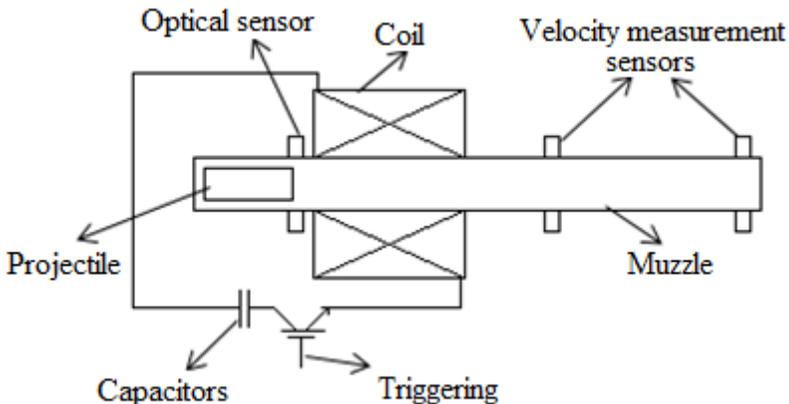


Figure 6. Reluctance coil gun.

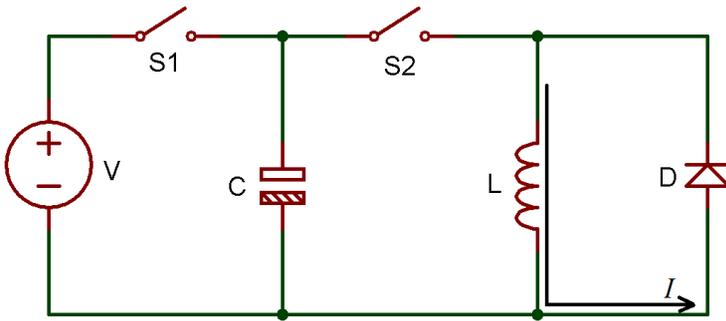


Figure 7. Equivalent circuit of the reluctance coil gun.

Figure 7 shows the equivalent circuit of the RCG. While switch S_2 is open, switch S_1 is closed and the capacitors are charged. Subsequently, the energy within the capacitor is transferred to the coil when switch S_1 is opened and switch S_2 is closed. In order to switch the energy given to the coil, semiconductor circuit elements such as thyristors, transistors, MOSFETs and IGBT, which can operate at high voltages, should be used as switching elements. While the trigger circuits of these semiconductor circuit elements operate at relatively low voltage, the voltage applied to the coil is high. Therefore, these circuit elements must be used with a driver. In addition, a damping circuit should be used to protect against damage that may occur from on and off states. The damping circuit may consist of diode, capacitor and resistor.

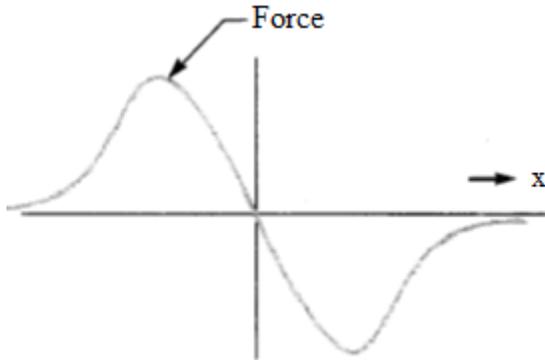


Figure 8. Force applied to the projectile vs distance.

Figure 8 shows the change of the force exerted on the projectile in the REL depending on the distance. Here the zero point is the middle point of the coil. When the projectile passes the midpoint of the coil, the force applied to the projectile is in the opposite direction, that is, the projectile is pulled back to the center of the coil (Bresie and Andrews, 1991).

$$a = \frac{x\mu_0(NI)^2}{2\rho l a I^2} \quad (1)$$

$$x = \mu / \mu_0 - 1 \quad (2)$$

In REL, the acceleration of the projectile can be found with Equation 1 (Chaowei et al., 2008). Here

l = projectile length,

ρ = material density of the projectile

NI = magnetomotive force

l = coil length

Given that the RCG's projectile is ferromagnetic and the B-H curve of the ferromagnetic material is nonlinear, it is difficult to determine the performance of REL. For this purpose, the finite element method (FEM) is used. FEM is an analysis method used to analyze problems that cannot be solved or are difficult to solve with known methods (Daldaban and Sari, 2015). In many previous studies, FEM was used to analyze REL (Daldaban and Sari, 2014; Daldaban and Sari, 2016; Sari and Daldaban, 2019; Chaowei et al., 2008; Yadong et al., 2010; Hou et al., 2012). There are many computer programs that can perform solutions with FEM. The most popular of these is the ANSYS Maxwell program. ANSYS Maxwell may be used to create a three-dimensional model of the REL. and the desired data can be obtained by solving it with FEM.

1.1.3. Hybrid Electromagnetic Launchers

Hybrid launchers are the combination of RAL and CL. Therefore, they have the characteristics of both RAL and CL (Shiyong et al., 2004).

2. VELOCITY MEASUREMENT SYSTEMS

Measuring the velocity of the launched projectile is an important issue regarding EML. As examples of velocity measurement systems; Ultrasonic velocity measurement systems, laser velocity measurement systems and velocity measurement systems using optical sensors can be given. The most used and most sensitive velocity measurement system is the velocity measurement system using optical sensors. In this velocity measurement system, two pairs of optical sensors are placed consecutively on the path of the projectile. If the time the projectile passes through these sensors is measured and the distance between the sensors is divided by this time, the velocity of the projectile can be found (Daldaban and Sari, 2016).

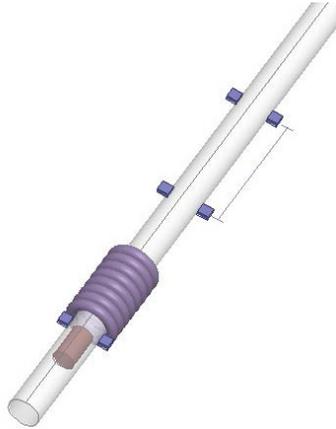


Figure 9. Measurement of projectile velocity with optical sensors.

3. GENERATING A 3D MODEL OF A RCG

Before realizing REL, the FEM model of the REL must be generated and analyzed. This is an important step to solve problems encountered in practice and optimize the system. Before generating the launcher model, the physical dimensions of the launcher (projectile thickness, projectile length, barrel inner and outer diameter, coil length and coil height) must be determined. The diameter and number of turns of the wire used in the coil must be determined, and the dimensions of the coil when it is wound must be determined. Figure 10 provides the launcher's dimensions. Here, the outer diameter of the barrel is 10 mm, the inner diameter of the barrel is 8 mm, the projectile length is 25 mm, the projectile diameter is 7 mm, the coil length is 50 mm, the coil diameter is 28.6 mm and the barrel length is 200 mm.

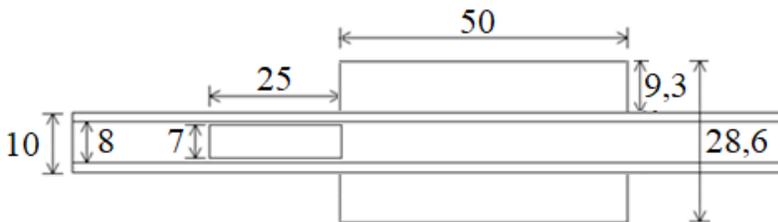


Figure 10. Dimensions of the launcher.

A 3D model of a RCG can be generated using the ANSYS Maxwell program, which can solve with FEM. Initially, after opening the program, click on the “Insert Maxwell 3D Design” section from the “Project” tab or click on the “Insert Maxwell 3D Design” icon. The name “Project1” in the

“Project Manager” section can be changed. A desired name is given instead of “Project1”. In this study, it was named “3D_RF”. To select the solution type, click “Solution Type” from the “Maxwell 3D” tab. Select “Transient” from the window that opens on the screen.

To generate the inside of the barrel, click “Regular Polyhedron” from the “Draw” tab or click the “Draw Regular Polyhedron” box. The starting coordinate, inner radius coordinate, and barrel length coordinate are entered in the coordinate boxes in the lower right corner of the program screen. The Enter key is pressed each time. Segment number is entered. Then click on “RegularPolyhedron1” in the “Model” section, its name can be changed in the “Properties” section, in this study it is entered as “InsideBarrel”. Material is changed in the “Properties” section, “vacuum” is selected by default. Select “air” from the “Edit” section.

To generate the barrel, click “Regular Polyhedron” from the “Draw” tab or click the “Draw Regular Polyhedron” box. The starting coordinate, outer radius coordinate, and barrel length coordinate are entered in the coordinate boxes in the lower right corner of the program screen. The Enter key is pressed each time. Segment number is entered. Then, click on “RegularPolyhedron1” in the “Model” section, its name can be changed in the “Properties” section, in this study it is entered as “Barrel”. Material is changed in the “Properties” section, “vacuum” is selected by default. Select “PVC plastic” from the “Edit” section. If desired, the color of the barrel can be changed by selecting a desired color from the “Color” section in the “Properties” section.

To obtain a hollow tubular barrel, the “InsideBarrel” must be removed from the generated “Barrel”. To do this, “Barrel” and “ InsideBarrel “ in the “Model” section are selected together by holding down the Ctrl key. Then click on the “Subtract” command from the “Boolean” section of the “Models” tab. In this box, there should be “ Barrel” on the left and “ InsideBarrel “ on the right.

In order to model the current flowing through the coil, a rectangle should be generated in the coil cross section on the “YZ” axis and excitation should be given from this rectangle. For this purpose, “YZ” is selected from the “Grid Plane” section in the “Models” tab. From this moment on, the drawings will be relative to the “YZ” axis. From the “Draw” tab, click the “Rectangle” command. Coordinates are entered in the coordinate section in the lower right corner. The Enter key is pressed each time. The model obtained with what has been done so far is shown in Figure 11.

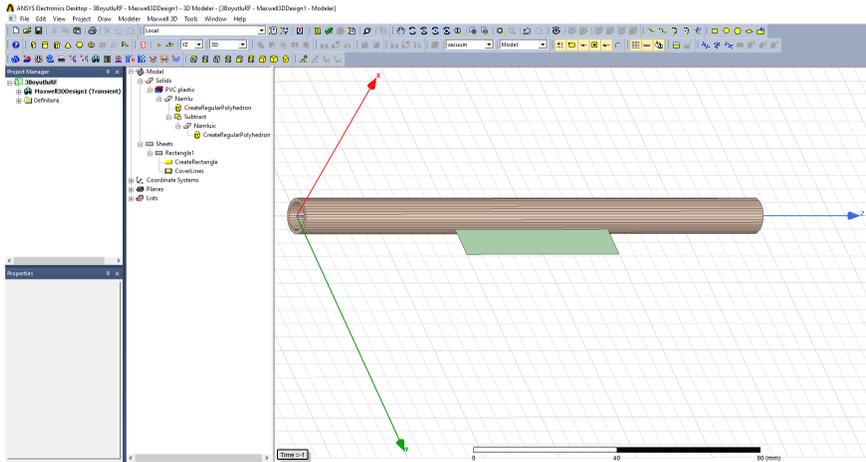


Figure 11. Steps to generate the model.

While “Rectangle1” is selected in the “Model” section, “Copy” and then “Paste” commands are clicked and “Rectangle2” is generated. While “Rectangle2” is selected, click “Around Axis” in the “Sweep” section of the “Draw” tab. Click on the “Z” axis in the opened box. Here, “Angle of sweep” should be 360 degrees. Thus, the coil is generated. Click “Rectangle2” in the “Model” section and its name can be changed in the “Properties” section. Here it has been changed to “Coil”. In the “Properties” section, click on “vacuum” in the “Material” section and select “Copper”. The model obtained with what has been done so far is shown in Figure 12.

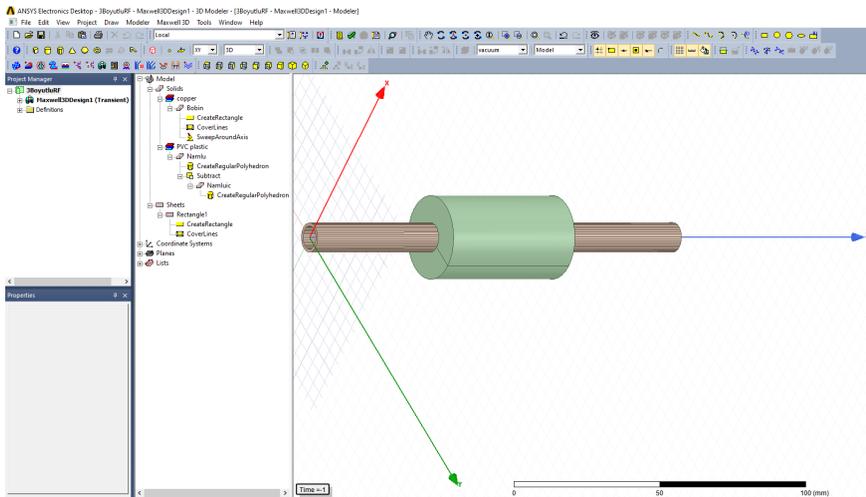


Figure 12. Steps to generate the model.

To generate the projectile, select “XY” from the “Grid Plane” section of the “Models” tab. From now on, plots will be relative to the “XY” axis. From the “Draw” tab, click “Regular Polyhedron” or click the “Draw

Regular Polyhedron” box. The starting coordinate is entered in the coordinate boxes in the lower right corner of the program screen, the radius coordinate of the projectile is entered, and the projectile length coordinate is entered. The Enter key is pressed each time. Segment number is entered. Click on “RegularPolyhedron1” in the “Model” section, change its name in the “Properties” section, and in this study it is entered as “Projectile”. Material is changed in the “Properties” section, “vacuum” is selected by default. A desired ferromagnetic material is selected from the “Edit” section, “steel_1010” is selected here. If desired, the color of the projectile can be changed by selecting a desired color from the “Color” section in the “Properties” section.

To excite the coil, select “Rectangle1” in the “Model” section we generated previously. Then click on “Excitations” from the “Maxwell 3D” tab, then click on “Coil Terminal” from the “Assign” section. The number of coil windings is entered in the “Number of Conductors” section in the window that opens. Right-click on “Excitations” among the project items in the “Project Manager” section and click on “Add Winding” from the menu that opens. In the sections in the window that opens, how the coil will be excited (Voltage, Current), starting current, the value of the voltage to be applied, the resistance and inductance values of the coil are entered. Right-click “Winding1” in the “Project Manager” section and click “Add Terminals” from the menu that opens. Select “Coil Terminal” in the opened box. Thus, the excitation of the coil is completed.

To generate the section where the projectile will move inside the barrel, click “Regular Polyhedron” from the “Draw” tab or click the “Draw Regular Polyhedron” box. The starting coordinate is entered in the coordinate boxes in the lower right corner of the program screen, the movement section radius coordinate is entered, and the movement section length coordinate is entered. The Enter key is pressed each time. Segment number is entered. Click on “RegularPolyhedron1” in the “Model” section, change its name in the “Properties” section, and in this study it is entered as “Band”. Material is changed in the “Properties” section, “vacuum” is selected by default. “air” is selected in the “Edit” section because the projectile will move in the air in the pipe. If desired, the color of the projectile can be changed by selecting a desired color from the “Color” section in the “Properties” section. The model obtained with what has been done so far is shown in Figure 13.

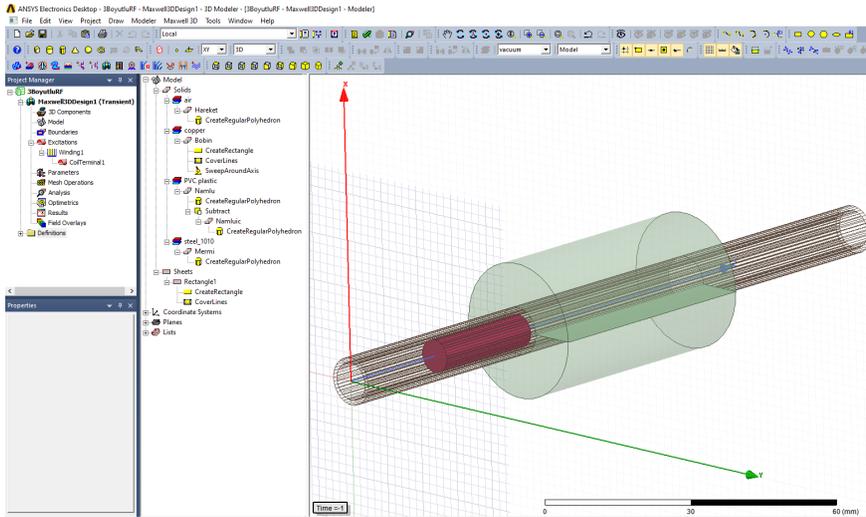


Figure 13. Steps to generate the model.

While “Band” is selected in the “Model” section, right-click on “Model” in the “Project Manager” section, click “Motion Setup” from the menu that opens, then click “Assign Band”. In the “Positive” section of the “Data” tab of the window that opens, the length that the projectile will travel in the barrel is entered. Click “Consider Mechanical Transient” in the “Mechanical” tab, enter the weight of the projectile in the “Mass” section. The program can calculate the weight of the projectile. If desired, the weight of the projectile can be calculated by clicking “Calculate”.

“Coil” is selected from the “Model” section, then “Mesh Operations”, “Assign, Inside Selection” and “Length Based” are clicked on the “Maxwell 3D” tab. In the window that opens, uncheck “Set maximum element length” and tick “Maximum number of additional elements” and write the desired value in front of it.

Select “Projectile” from the “Model” section, then click on “Mesh Operations”, “Assign, Inside Selection” and “Length Based” from the “Maxwell 3D” tab. In the window that opens, uncheck “Set maximum element length” and tick “Maximum number of additional elements” and write the desired value in front of it.

To define the area to be analyzed, click “Box” on the “Draw” tab and enter the analysis boundaries in the coordinate section at the bottom right.

From the “Maxwell 3D” tab, click “Analysis Setup” and then “Add Solution Setup”. The simulation time is entered in the “Stop time” section in the “General” tab of the opened window, and the simulation step time is entered in the “Time step” section. After entering the simulation time in

the “Stop” section of the “Save Fields” tab and the simulation step time in the “Step Size” section, click the “Add to List” button.

To add eddy current loss to the model, click “Excitations” and then “Set Eddy Effects” from the “Maxwell 3D” tab. “Coil” and “Projectile” are ticked in the window that opens. Thus, the eddy current loss in the coil and projectile is added to the model.

From the “Maxwell 3D” tab, click “Validation Check”. All those listed on the right should have a green check mark at the beginning. There are errors in the parts without green markings and these should be corrected. From the “Maxwell 3D” tab, click “Analyze All”. The program simulation runs. Figure 14 shows the final view of the model.

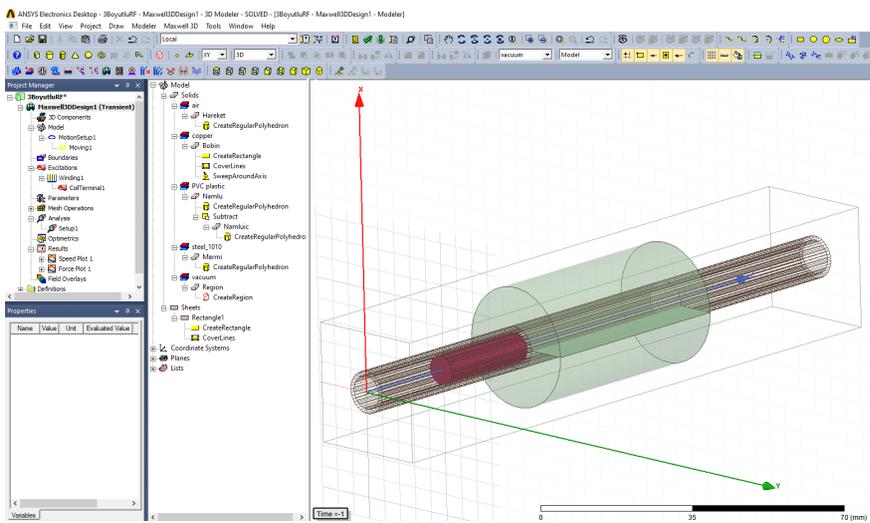


Figure 14. Final version of the model.

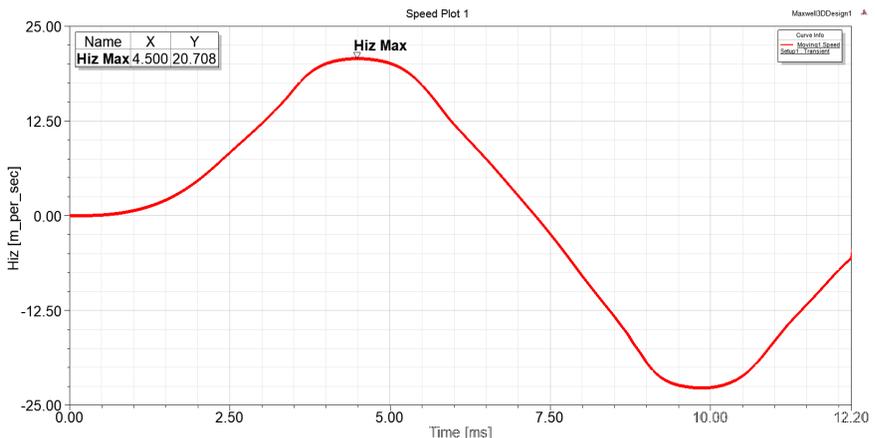


Figure 15. *Projectile velocity change.*

From the “Maxwell 3D” tab, click “Results”, “Create Transient Report”, “Rectangular Plot”. A graph can be drawn by selecting the parameter whose graph you want to draw in the window that opens. For example, for projectile velocity, “Speed” is selected in the “Category” section, and if “New Report” is clicked, the projectile velocity graph screen over time opens. If you want to draw a graph of the force applied to the projectile, click “Results”, “Create Transient Report”, “Rectangular Plot” from the “Maxwell 3D” tab. If “Force” is selected from the “Category” section in the opened window, “Moving1.Force_z” is selected from the “Quantity” section and “New Report” is clicked, a graph of the force applied to the projectile on the Z axis is drawn according to time.

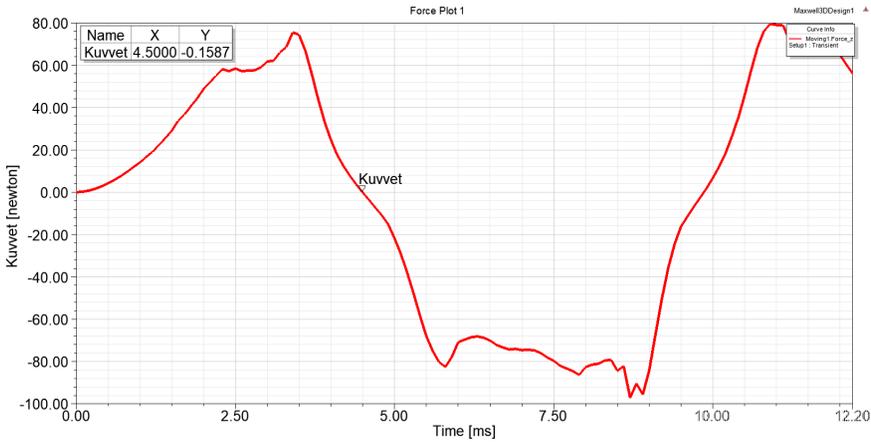


Figure 16. *Change of force applied to the projectile.*

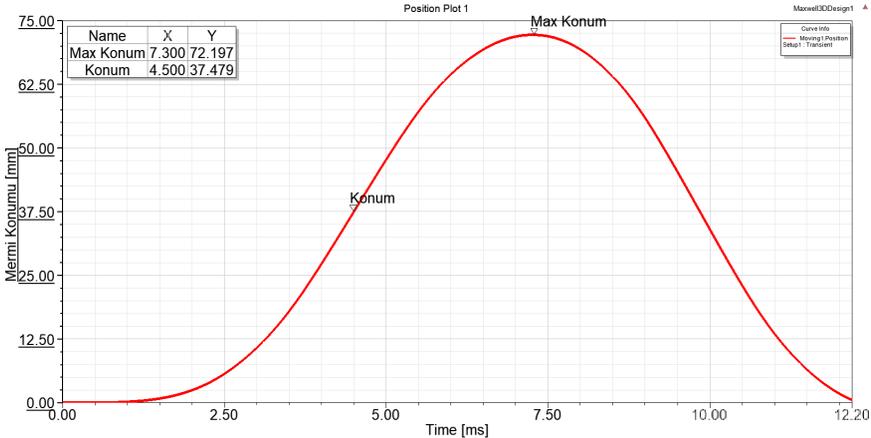


Figure 17. *Change of the projectile position.*

Figure 15 shows the projectile velocity change graph, Figure 16 shows the change graph of the force applied to the projectile, and Figure 17 shows the change graph of the projectile position. When these graphics are examined, the projectile velocity reached its highest value in the 4.5th millisecond with 20.708 m/sec. At this moment, the force applied to the coil is close to zero and the position of the projectile is very close to the middle of the coil, at 37.479 mm (37.5 mm is in the middle of the coil). At the 4.5th millisecond, the energy applied to the coil must be cut off and the energy in the coil must be absorbed, otherwise the projectile 's muzzle velocity will decrease as the projectile will be pulled back to the middle of the coil. As shown in Figure 16, if the energy applied to the coil is not cut off within 4.5 milliseconds, a force acts in the opposite direction on the projectile and the projectile velocity decreases or even becomes negative, as shown in Figure 15. In other words, the projectile is drawn back into the middle of the coil. As shown in Figure 17, the projectile reaches its furthest position at 72.197 mm in 7.3 milliseconds, and from this point onwards its position decreases, that is, it is drawn back into the coil.

The Maxwell program solves the problem by dividing the system into small pieces according to finite element analysis. To see the launcher divided into small pieces, select the relevant part of the launcher, right-click on "Fields Overlays" in the "Project Manager" section, and click on "Plot Mesh" from the menu that opens. Figure 18 and Figure 19 show the launcher divided into small parts.

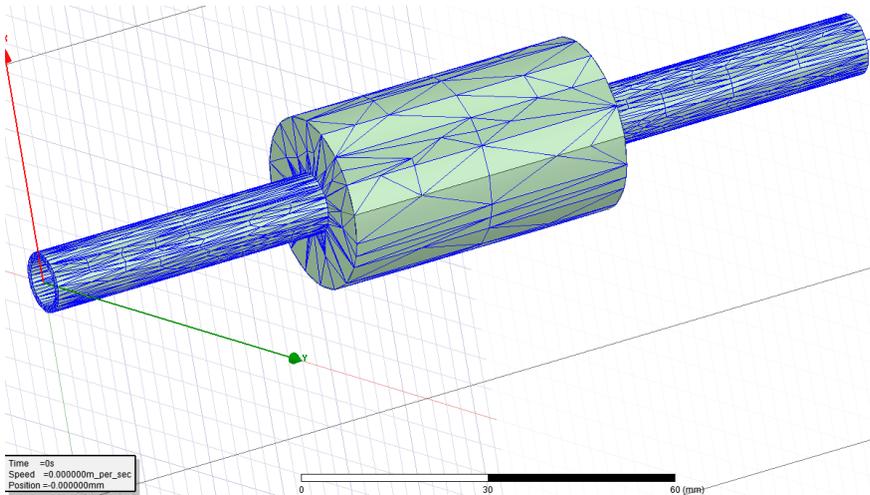


Figure 18. Division of the barrel and coil into small areas according to the finite element method.

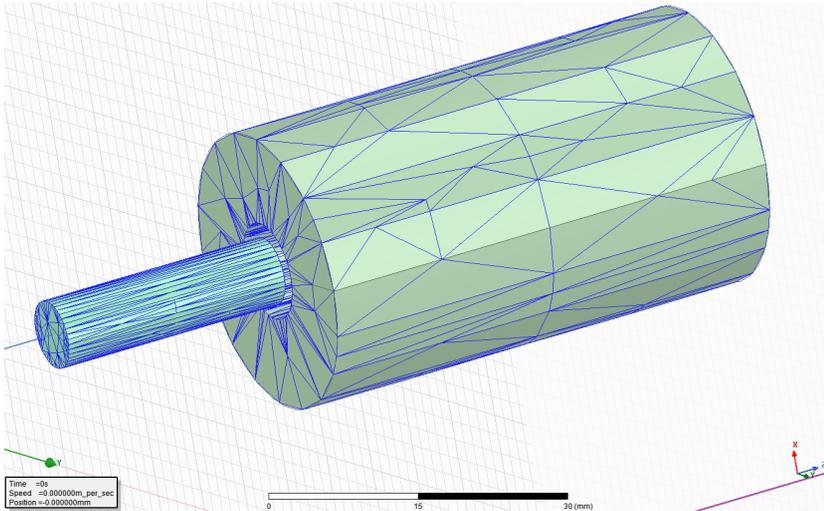


Figure 19. Division of the projectile and coil into small areas according to the finite element method.

The magnetic field examination of the launcher can also be done with the Maxwell program. To do this, right-click on “Field Overlays” in the “Project Manager” section while the part of the launcher that you want to examine is selected or all its components are selected. From the menu that opens, click “Fields”, “B”, “Mag_B”. The time to be examined in the simulation is selected. Figure 20 shows the magnetic field at 1 msec. With the colored scaling on the top left, you can see how much magnetic field is in which part of the launcher. As shown in Figure 20, the magnetic field in the coil is around 0.5 T - 1 T. Figure 21 shows the magnetic field at 4.5 ms. Here the projectile is in the middle of the coil.

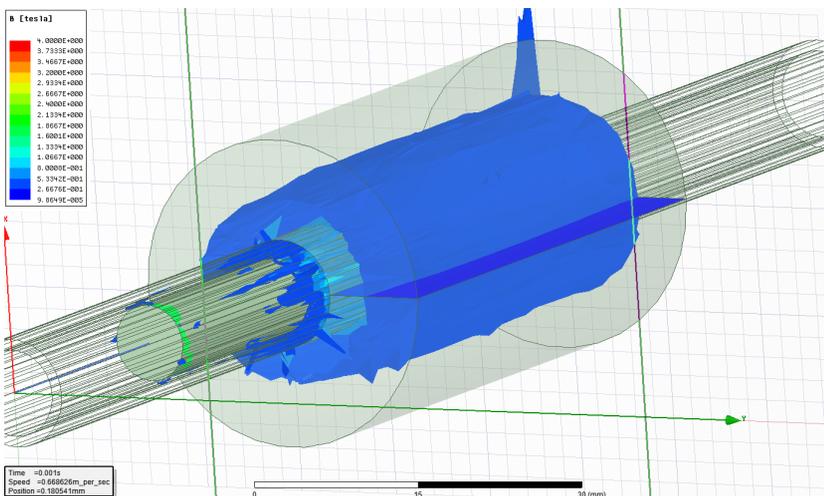


Figure 20. Magnetic field of the launcher at 1 ms.

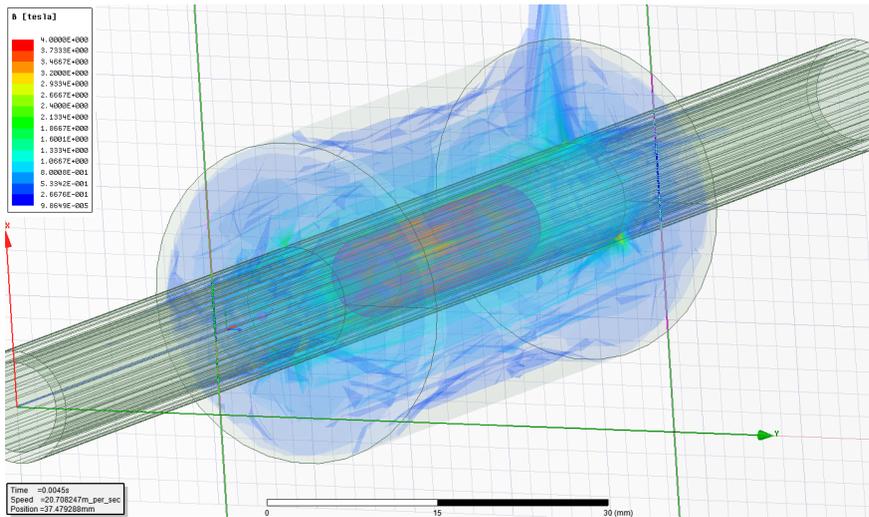


Figure 21. *Magnetic field of the launcher at 4.5 ms.*

4. CONCLUSION

In this study, a 3D model of a REL was generated and the effect of launcher parameters on projectile velocity was examined. At the end of the investigations, it was seen that a launcher with a higher velocity could be obtained by changing the launcher parameters. Choosing the correct parameters of EML is important in terms of projectile velocity and efficiency of the system. If chosen incorrectly, the muzzle velocity of the launcher and the efficiency of the system will decrease.

Optimization studies can be carried out by changing the launcher parameters to increase the launcher's projectile velocity. In previous studies (Daldaban and Sari, 2014) (Daldaban and Sari, 2015) (Sari and Daldaban, 2019), it was examined how projectile material and shape affect projectile speed. It is possible to increase the projectile velocity by changing other parameters. These parameters; It may be the inner and outer diameter of the barrel, the length of the coil, the number of windings, the thickness of the coil wire, and the diameter of the coil. By changing these parameters, optimization can be made without building the launcher, thus saving time and cost can be achieved by determining the parameters of the launcher with the highest velocity.

REFERENCES

- Bresie, D. A., & Andrews, J. A. (1991). Design of a reluctance accelerator. *IEEE Transactions on Magnetics*, 27(1), 623-627.
- Chaowei, Z., Pengshu, D., Xiaojun, D., Sanqun, L., Zhiyuan, L., & Guanghui, Z. (2008, October). Analysis of reluctance coil launcher performance using coupled field-circuit method. In *International Conference on Electrical Machines and Systems*, Wuhan/China, (pp. 4049-4052).
- Daldaban, F., & Sari, V. (2016). The optimization of a projectile from a three-coil reluctance launcher. *Turkish Journal of Electrical Engineering and Computer Sciences*, 24(4), 2771-2788.
- Daldaban, F., & Sari, V. (2015). Bir Relüktans Fırlatıcının Sonlu Elemanlar Yöntemi ile İncelenmesi. *Gazi Üniv. Müh. Mim. Fak. Der.*, 30(4), 605-614.
- Daldaban, F., & Sari, V. (2014, September). Design and implementation of a three-coil linear reluctance launcher. In *16th International Power Electronics and Motion Control Conference and Exposition*, Antalya/Turkey, (pp. 1084-1088).
- Engel, T. G. (2017). Scientific classification method for electromagnetic launchers. *IEEE Transactions on Plasma Science*, 45(7), 1333-1338.
- Fair, H. (1982). Electromagnetic propulsion: A new initiative. *IEEE Transactions on Magnetics*, 18(1), 4-6.
- Hou, Y., Liu, Z., Ouyang, J. M., & Yang, D. (2012, May). Parameter settings of the projectile of the coil electromagnetic launcher. In *16th International Symposium on Electromagnetic Launch Technology*, Beijing/China, (pp. 1-4).
- Jing, B., Liao, T., Jiang, T., Chen, L., & Jia, X. (2017, November). Optimal design and simulation of combined reluctance-induction electromagnetic launcher. In *Progress in Electromagnetics Research Symposium-Fall*, Singapore, (pp. 1377-1381).
- Keshtkar, A., Bayati, S., & Keshtkar, A. (2008, June). Effect of rail's material on railgun inductance gradient and losses. In *14th Symposium on Electromagnetic Launch Technology*, Victoria, BC, Canada, (pp. 1-4).
- Lehmann, P., Reck, B., Vo, M. D., & Behrens, J. (2006). Acceleration of a sub-orbital payload using an electromagnetic railgun. *IEEE transactions on magnetics*, 43(1), 480-485.
- Liu, W., Cao, Y., Zhang, Y., Wang, J., & Yang, D. (2010). Parameters optimization of synchronous induction coilgun based on ant colony algorithm. *IEEE Transactions on Plasma Science*, 39(1), 100-104.
- Marder, B. (1993). A coilgun design primer. *IEEE transactions on magnetics*, 29(1), 701-705.
- McKinney, K., & Mongeau, P. (1984). Multiple stage pulsed induction acceleration. *IEEE Transactions on Magnetics*, 20(2), 239-242.

- Mosallanejad, A., & Shoulaie, A. (2012). A novel structure to enhance magnetic force and velocity in tubular linear reluctance motor. *Turkish Journal of Electrical Engineering and Computer Sciences*, 20(7), 1063-1076.
- Sari, V., & Daldaban, F. (2019). Examination of the effect of different projectile geometries on the performance of reluctance launcher using 3D finite element analysis. *Cumhuriyet Science Journal*, 40(2), 518-526.
- Shiyong, Y., Ying, W., Shanbao, C., Qian, L., Xuqiong, L., & Wei, W. (2004, May). A novel type rail-coil hybrid electromagnetic launcher. In *12th Symposium on Electromagnetic Launch Technology*, Snowbird, UT, USA, (pp. 155-157).
- Slade, G. W. (2005). A simple unified physical model for a reluctance accelerator. *IEEE transactions on magnetics*, 41(11), 4270-4276.
- Tzeng, J. T., & Schmidt, E. M. (2010). Comparison of electromagnetic and conventional launchers based on Mauser 30-mm MK 30-2 barrels. *IEEE Transactions on Plasma Science*, 39(1), 149-152.
- Yadong, Z., Ying, W., & Jiangjun, R. (2010). Capacitor-driven coil-gun scaling relationships. *IEEE Transactions on Plasma Science*, 39(1), 220-224.
- Yu, X., & Fan, Z. (2010). Simulation and two-objective optimization of the electromagnetic-railgun model considering VSEC resistance and contact resistance. *IEEE Transactions on Plasma Science*, 39(1), 405-410.
- Zhang, Y., Ruan, J., & Wang, Y. (2010). Scaling study in a capacitor-driven rail-gun. *IEEE transactions on plasma science*, 39(1), 215-219.



BANANA FIBER

Suat CANOĞLU¹

Ayberk ŞİT²

1 Prof. Dr. Arzu USYAL, Mersin Üniversitesi Eğitim Fakültesi Güzel Sanatlar Eğitimi Bölümü Resim-İş Eğitimi Anabilim Dalı, arzu.guldali@gmail.com, ORCID: 0000-0003-2124-7902

2 Doç. Dr. Emrah UYSAL, Mersin Üniversitesi Eğitim Fakültesi Güzel Sanatlar Eğitimi Bölümü Resim-İş Eğitimi Anabilim Dalı, emrah.33@gmail.com, ORCID: 0000-0003-2565-9533

1. INTRODUCTION

Oil-derived synthetic fibers are a source of confidence in the developing textile industry but these fibers also bring high carbon emissions and environmental problems [1]. Using environmentally friendly fibers in production is one of the effective solutions that can be implemented in the textile industry to protect the environment and minimize global warming [2]. The demand for environmentally friendly fabrics and awareness of environmental problems has increased. Day by day, it is realized that natural resources need to be used more effectively. As a result, there is a great interest in natural fibers today [3].



Figure 1. Banana plant [7]

Banana belongs to the *Musa* genre within the family *Musaceae* [4,5]. It is a monocotyledonous plant that can grow up to approximately 7.5 meters tall [4,6]. Figure 1 shows the banana plant [7].

FAO (Food and Agriculture Organization) crops and livestock products (production) database shows that 124,978,578.48 tons of bananas were produced in 5,336,862 hectares of area in 2021. The highest production was made in Asia, which accounted for 54.4% of the total production. Asia was followed by the Americas, where 25.3% of the production was realized. Production rates were 18.4% in Africa, 1.4% in Oceania and 0.5% in Europe. The country that produced the most bananas (33,062,000 tons) in 2021 was India. Figure 2 shows the production share of bananas by region [8].

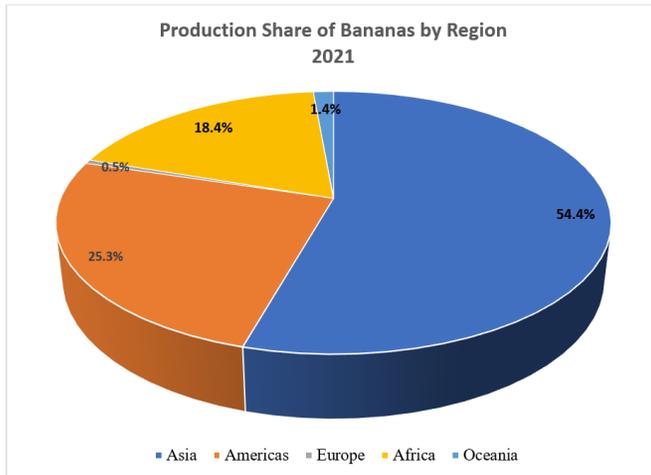


Figure 2. *Banana production share by region [8]*

Growth in banana demand has led to an increase in banana planting areas and banana production. Therefore, a significant amount of waste is generated [9]. After the banana fruit is harvested, plant remains are often left or burned [10,11]. The residual parts of banana plants are a source of fiber [11]. By obtaining fiber through the utilization of wastes, income will be earned and environmental and climate-related impacts caused by the burning process will be reduced [10,1].

This chapter aims to provide information about the extraction, properties, structure and application areas of banana fiber.

2. METHODS OF EXTRACTING BANANA FIBER

There are manual, mechanical, chemical and biological methods to extract banana fibers. Mechanical and chemical methods are more popular than others [11]. These fibers are mostly extracted from the pseudo-stem of banana plants [12]. Banana pseudo-stem allows nutrients to reach fruits from the soil [13].

In the decortication method, which is a mechanical method, the stems of the banana plant are crushed between rollers [9]. After harvesting bananas from the plant, pseudo-stem sheaths are manually split from each other. The sheath is held at one end and fed into the machine. The machine has a drum that rotates at high speed. Banana fibers are separated due to high mechanical action. A combing process is applied to banana fibers to remove remaining pseudo-stem residues. The combed banana fibers are washed and dried in the final stage. The quality of manually extracted fibers is higher but it is an accepted method as it allows large production capacity [14]. Thanks to the use of a decorticator, fiber production improves

by 20-25 times in comparison to manual extraction [9]. Sharp objects are used in manual fiber extraction. Examples of these objects are knives or broken pottery. It is widely used in villages and rural areas. Due to its laboriousness and low production quantity, manual fiber extraction is not preferred in large-scale production. Figure 3 shows the extraction of banana fibers by manual and mechanical methods [14].

Chemical extraction involves different environments such as alkali, acidic, or both [11]. A decrease in the roughness of banana fiber is observed due to the application of NaOH [9]. Although the chemical extraction method has advantages, waste chemicals induce pollution [11].

In the biological digestion process, plant stems are kept in water for several days or weeks to activate microorganisms. Banana fibers can be obtained through the use of enzymes. Enzymes such as pectinase and cellulase are used for this purpose [9].

Xu *et al.* (2015) used mechanical, enzymatic and chemical methods to obtain banana pseudo-stem fibers. It was aimed to evaluate the effects of the used methods on fiber properties. Sodium hydroxide, sulfuric acid, hydrogen peroxide, sodium citrate, protease and pectinase were used in the study. Banana pseudo-stem sheaths were fed into the decorticator. The average tensile strength of the fibers extracted by mechanical method was found as 210 MPa. Higher elongation was detected in banana pseudo-stem fibers extracted by chemical method. The average tensile strength of these fibers was 333 MPa. The average tensile strength of the fibers obtained by the enzymatic method was 235 MPa. Crystallinity index values were determined as 56.6% of fibers obtained by the mechanical method, 60.2% of fibers obtained by the enzymatic method, and 61.2% for fibers obtained by chemical method. Banana pseudo-stem fibers obtained by mechanical method showed the highest Young's modulus. As a result of obtaining fibers with this method, a high amount of short fibers was observed. The color of the fibers obtained by mechanical method was light brown. Banana pseudo-stem fibers obtained by chemical method were found to be white in color and clean. It was observed that the fibers obtained by the enzymatic method were light yellow. The fibers obtained by the chemical method were softer than the fibers obtained by other methods (mechanical, enzymatic) in the study. It was seen that lignin and hemicellulose were highly reduced as a result of enzymatic or chemical treatment. It was declared that the brittle and amorphous structure of hemicellulose and other waxy substances had decreased the strength of banana pseudo-stem fiber. According to thermogravimetric tests, the thermal stability of fibers extracted by chemical method was higher [15].

Mumthas *et al.* (2019) examined the effects of different fiber extraction methods (mechanical, chemical, biological) on banana pseudo-stem fiber. In the study, decortication was used to obtain fiber by mechanical method, sodium hydroxide was used to obtain fiber by chemical method and pectinase enzyme was used to obtain fiber by the biological method. Mechanically obtained banana fiber diameter was higher. Comparing the biological method with the mechanical method, the average fiber strength was higher in the biological method. As a result of the observations, fibrils were damaged during the mechanical fiber extraction process. Removal of lignin in the structure was observed in the biological and chemical extraction process. It was reported that there was no interrelationship between fiber extraction method and fiber extensibility [9].

3. STRUCTURE AND PROPERTIES OF BANANA FIBER

Banana fiber has a lignocellulosic structure [16]. The fiber contains cellulose, hemicellulose, and lignin, as well as other substances like pectin and wax [4]. It was stated that banana fiber contained 63-64% cellulose, 19% hemicellulose, and 5% lignin [17,18]. Elseify *et al.* (2023) announced that banana fiber had a cellulose content of $57.18 \pm 0.27\%$, hemicellulose content of $14.8 \pm 0.24\%$, and lignin content of $4.38 \pm 0.113\%$ [1].

Banana pseudo-stem fiber is a multicellular fiber [6]. Figure 3 shows a cross-sectional view of banana fiber under SEM microscope at 2600x magnification [19].

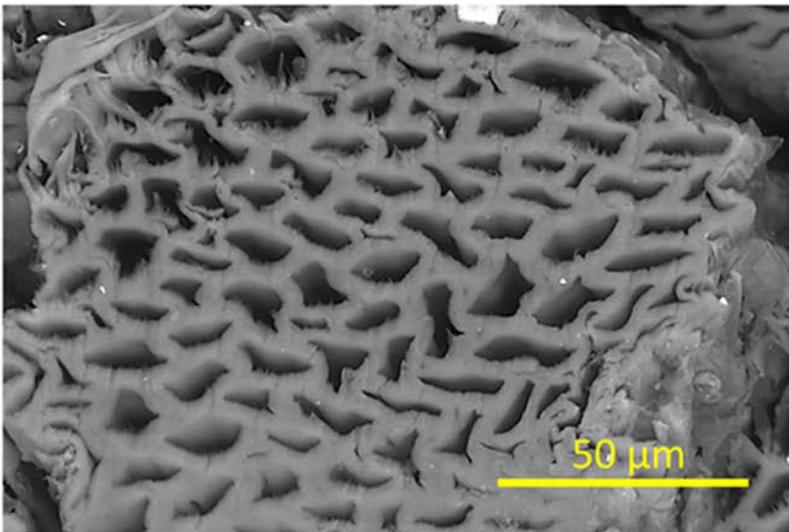


Figure 3. Cross-sectional view of banana fiber under SEM microscope at 2600x magnification [19]

Banana fiber has high mechanical properties and dimensional stability, as well as being environmentally friendly, sustainable and biodegradable [20]. The density of banana fiber was reported to be 1.35 g/cm^3 [17,18,21,22]. Moreover, it was noted that banana fiber had an elongation at break of 5-6%, tensile strength of $550 \pm 6.7 \text{ MPa}$, Young's modulus of 20 GPa, fiber diameter of $120 \pm 5.8 \text{ }\mu\text{m}$, microfibril angle of 11° , lumen size of $5 \text{ }\mu\text{m}$ and moisture content of 10-11% [17,18]. In a study, the breaking tenacity of banana fiber was 30.26 g/tex [23]. In a different study, banana fiber showed a tenacity of $42.8 \pm 6.5 \text{ cN/tex}$ [4]. In a study conducted by Pothan *et al.* (2003), the diameters of 5 different banana fiber samples were in the range of 50-250 μm , Young's modulus was in the range of 27.698-32.703 GPa, tensile strength was in the range of 711-789 MPa, and strain was in the range of 2.4-3.5% [24]. Murali Mohan Rao and Mohana Rao (2007) stated that the tensile strain of banana fiber was 3.36%, average tensile strength was 600 MPa, specific tensile strength was $0.4444 \text{ MPa}/(\text{kg}\cdot\text{m}^{-3})$, average tensile modulus was 17.85 GPa and specific tensile modulus was $13.22 \text{ MPa}/(\text{kg}\cdot\text{m}^{-3})$. They declared that 10.71% moisture was present in banana fiber under normal atmospheric conditions. Banana fiber was described to have an approximately circular cross-sectional shape [21]. Subramanya *et al.* (2017) examined various properties of banana fiber extracted from the pseudo-stem of banana plants grown in Bengaluru, Karnataka, India. The average diameter of the fibers studied was $167 \pm 0.1 \text{ }\mu\text{m}$. The average Young's modulus value of 20 different banana fibers tested was 13 GPa, the average tensile strength value was 161 MPa and the average elongation value was %1.27. As a result of the stress-strain curve obtained; the tensile strength of the fibers was moderate level, elongation percentage of the fibers was low and the fibers had a brittle structure. Weibull Analysis was performed on tensile strength values obtained. Characteristic strength was reported to be 3800 MPa and 22,700 MPa, with a reliability value of 99% and 0.01%, respectively [25]. According to a study, banana fiber had a diameter of $121.4 \pm 5.4 \text{ }\mu\text{m}$, density of $1.28 \pm 0.09 \text{ g/cm}^3$, tensile strength of 377.5 MPa, specific tensile strength of $294.92 \text{ MPa}/(\text{g}\cdot\text{cm}^{-3})$, crystallinity index of 52.36% and elongation of 3.1% [1]. Figure 4 shows a bundle of fibers obtained from a banana plant [7].

Cellulose, hemicellulose, and lignin ratios in banana fiber and properties of banana fiber are reported in Table 1 and Table 2.



Figure 4. Bundle of fibers obtained from banana plant [7]

Table 1. Cellulose, hemicellulose, and lignin ratios in banana fiber

Component	Values
Cellulose (%)	63-64 [17,18,26]; 69.53 [23]; 65 [22]; 57.64 [27]; 57.18±0.27 [1]; 43.6 [4]
Hemicellulose (%)	19 [18,26]; 29.05 [27]; 14.8±0.24 [1]; 14 [4]; 5.1 [23]
Lignin (%)	5 [17,18,22]; 17.83 [23]; 13.30 [27]; 11 [4]; 4.38±0.113 [1]

Banana and sisal fibers contain similar amounts of cellulose and banana fiber has a lower microfibrillar angle. The diameter of banana fiber is smaller than the diameter of sisal fiber. The surface area of fiber per unit area of banana fiber reinforced composite is higher than the surface area of fiber per unit area of sisal fiber reinforced composite. Thanks to this situation, stress can be better transferred to banana fiber from the matrix [17].

Paul *et al.* (2008) applied various chemical treatments to banana fibers. In alkali treatment, two different concentrations of NaOH were used: 2% and 10%. The procedure was carried out for 1 hour. After the process, the fibers were washed with water, and then washed with water containing a low amount of acetic acid. The fibers were finally dried at 70 °C for 3 hours. Fibrillation observed in fibers treated with 10% NaOH was higher than fibrillation observed in fibers treated with 2% NaOH. In the study, pretreatment with NaOH was performed before benzylation. Fiber surface roughness increased as a result of benzylation compared to untreated

ed fiber surface. In addition, the fiber surface exhibited fibrillation. It was stated that the chemical treatment allowed improved contact between the matrix and the fiber [26]. Chemical reactions of banana fiber with various chemicals are shown in Figure 5 [14].

Table 2. Properties of banana fiber

Property	Value
Diameter (μm)	120±5.8 [17,18]; 300-450 [10]; 253.0673 [23]; 200 [4]; 167±0.1 [25]; 125-150 [26]; 121.4±5.4 [1]; 80-250 [22]
Density (g/cm^3)	1.35 [17,18,21,22]; 1.45 [10]; 1.39 [23]; 1.3 [26]; 1.28±0.09 [1]
Tensile Strength (MPa)	550±6.7 [17,18]; 600-750 [26]; 600 [21]; 400-600 [10]; 377.5 [1]; 161 [25]
Specific Tensile Strength [MPa/($\text{g}\cdot\text{cm}^3$)]	444.4 [21] 294.92 [1]
Tensile Modulus (GPa)	20 [17,18]; 29-32 [26]; 17.85 [21]; 16-20 [10]; 12.2 [1]; 13 [25]
Specific Tensile Modulus [MPa/($\text{kg}\cdot\text{m}^3$)]	13.22 [21]
Flexural Modulus (GPa)	2-5 [18]
Crystallinity Index (%)	52.36 [1]
Elongation (%)	5-6 [17,18]; 7-12 [10]; 3.36 [21]; 3.1 [1]; 2.51 [23]; 2-4 [26]; 1.27 [25]; 1.0-3.5 [22]
Microfibrillar Angle (°)	11 [17,18,22]
Lumen Size (μm)	5 [17,18]

Vishnu Vardhini and Murugan (2017) examined the effects of treatment with xylanase and laccase enzymes on banana fiber. Lignin removal increased with increasing enzyme concentration. Lignin was removed in higher amounts with the application of the laccase enzyme. As a result of treatment with xylanase enzyme, hemicellulose removal was higher. It was announced that density, tensile strength, and cellulose ratio had increased to 15% enzyme concentration. It was stated that these values had begun to decrease at 20% concentration. Improvement in cellulose content had a positive effect on the tensile strength of the fiber. Fiber diameter (253.0673 μm) and percentage moisture regain (13.25%) values decreased with increasing applied enzyme concentration from 10 to 15% and also from 15 to 20%. Degradation of fibrils happened as a consequence of treatment with 20% concentration of both enzymes [23].

Ortega *et al.* (2016), subjected banana fibers to enzymatic treatment. Banana fibers were cut into 5 cm lengths before enzymatic treatment. Two enzymatic formulations, Biopectinase M01 and Biopectinase K, were applied to the fibers. The first of these enzymes was made of pectinase and hemicellulose, the second was made of polygalacturonase. In the study, optimum process conditions were achieved by using Biopectinase K enzyme at 45 °C temperature, 4.5 pH for 6 hours with renewing bath after

3 hours. It was declared that the enzymatic treatment provided enhancement in regards to fibrillation and cleanliness of banana fiber. Cleanliness was better after Biopectinase K treatment compared to Biopectinase M01 treatment. Good results were not obtained within 24 hours, 48 hours, and 7 days of treatment and the reason for this was enzyme deactivation. As a result of enzymatic treatment, there was a slight reduction in mechanical properties. An increase in thermal stability was achieved by removing less thermally stable materials from the structure, primarily hemicellulose and pectin. Onset and peak temperatures of untreated banana fibers treated with Biopectinase K enzyme are shown in Table 3 [4].

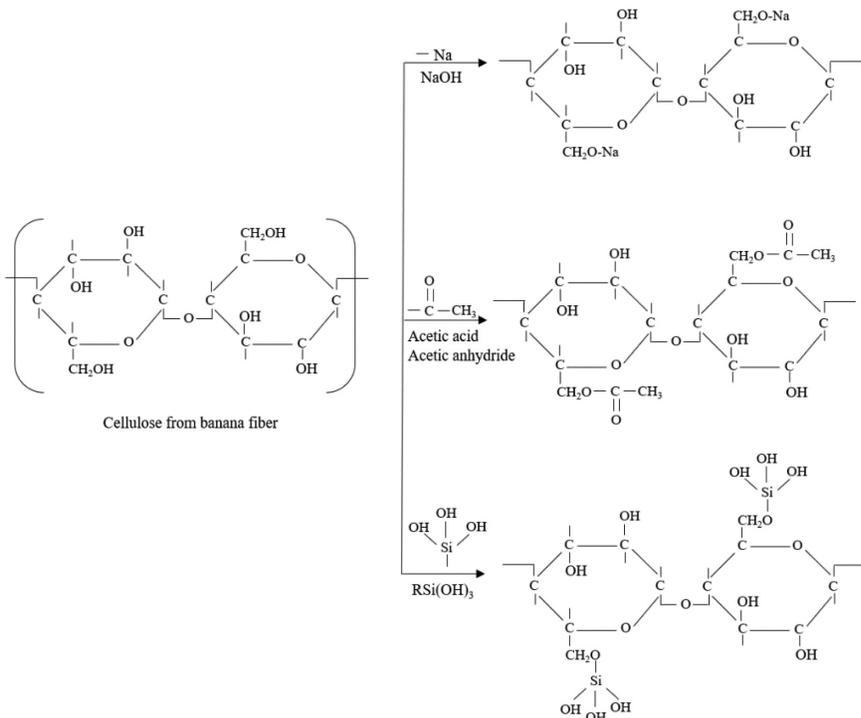


Figure 5. Chemical reactions of banana fiber with various chemicals [14]

Table 3. According to a study conducted by Ortega et al. (2016), the onset and peak temperatures of untreated banana fibers treated with Biopectinase K enzyme for 6 hours with the renewal of the bath after 3 hours at concentrations of 25% and 100% related to fiber weight [4]

Fiber	Onset (°C)	Peak (°C)
Untreated banana fiber	245	280
Banana fiber %25, 6 hours	300	321
Banana fiber %100, 6 hours	290	316

In a study, thermogravimetric analysis of banana pseudo-stem fibers showed that the fibers had 3 main zones of weight loss for fiber samples obtained by mechanical, chemical, and enzymatic methods. Between 45 °C to 100 °C, banana pseudo-stem fibers lost water. The next weight loss was seen between 250 °C to 370 °C. Degradation of non-cellulosic materials (e.g., lignin) occurred in the third weight loss zone. It was expressed that the most challenging component to decompose was lignin [15]. In a different study, it was reported that banana fibers had experienced 4 weight loss steps. The first step of weight loss that occurred was dehydration, the second step was hemicellulose degradation, the third step was cellulose degradation and the fourth step of weight loss was lignin degradation. It was reported that degradation of hemicellulose in banana fiber had occurred at nearly 190 °C. At onset temperature 300 °C, a large weight loss took place in banana fibers [1].

Teli and Valia (2013) applied an acetylation process to banana fiber to increase its ability to absorb oil. It was reported that -OH groups were replaced by acetyl groups and amorphous content increased due to the acetylation process. The hydrophobicity and oleophilicity of acetylated banana fibers increased. The percentage of cellulose in banana fiber decreased as a consequence of the acetylation process. Weight loss at 250 °C was reported as 7.39% in the untreated sample and 10.59% in the acetylated sample. Strong decomposition occurred at 350 °C. The weight loss of untreated banana fiber at this temperature was 35.67%, and the weight loss of acetylated banana fiber was 65.18%. Above this temperature, weight loss happened more slowly. 92.56% weight loss was observed in untreated banana fiber at 550 °C. This value was 99.11% in acetylated banana fiber. The thermal stability of untreated fiber was higher than that of acetylated fiber. It was noted that this situation might occur due to the disintegration of intermolecular interactions throughout the acetylation process [27].

4. APPLICATION AREAS OF BANANA FIBER

Banana fiber can be used as reinforcement material in composites [10]. Banana fiber is used in construction applications such as concrete blocks and compressed soil blocks, automotive applications such as automotive parts, and various composite applications [20]. Banana fiber reinforced composite was used as an under-floor protection trim in automobiles [28]. Radomes used in aerospace and maritime to protect radar antennas are also an example of composite applications of banana fiber [11]. In a study, composite material was manufactured. In the manufacturing steps of the composite material, it is first seen that pseudo-stems are collected. The pseudo-stems were cut and after that, the external layer of the pseudo-stems was removed. Banana fibers were obtained using a decorticator, then the

fibers were washed and dried in the open air. Banana fibers, high density polyethylene, polylactic acid, and anhydride-modified polyethylene were used in biocomposite materials. Components were mixed based on various formulations and finally injected [29].

Recently, more importance has begun to be given to fabrics made of banana fiber [30]. Banana fiber can be used in many areas such as clothes, ties, pillowcases, tablecloths, curtains, carpets, mats, coffee and tea bags, bags, ropes, fishing nets and paper [30,2,6]. Banana fiber is used in kimonos in Japan [3]. The fiber can be used in packaging material [6].

CONCLUSION

In this chapter; extraction methods, structure, various properties, and application areas of banana fiber were examined. The demand for natural fibers is increasing to reduce the negative impact on the environment. Banana fiber is one of the natural fibers of plant origin. Banana fiber has tensile strength and tensile modulus above a certain level. The fiber exhibits lower elongation compared to various fibers. The wide application area shows the commercial importance of banana fiber. It was tried to draw attention to obtaining fiber by utilizing wastes after collecting banana fruit. The usage of banana fiber and other biologically degradable and renewable fibers will contribute to a more hopeful future.

REFERENCES

- [1] Elseify, L.A., Midani, M., El-Badawy, A.A., Awad, S., Jawaid, M. (2023) Comparative study of long date palm (*Phoenix dactylifera* L.) midrib and spadix fibers with other commercial leaf fibers. *Cellulose*, 30, 1927–1942.
- [2] Kalkancı, M. (2018) *Tekstil ve Hazır Giyim Sektöründe Çevre Dostu Tekstil Lifleri. Mühendislik Alanında Akademik Çalışmalar*. Hatipoğlu, M., Gündoğan, K. (eds); Gece Kitaplığı, Ankara, Türkiye.
- [3] Karthik, T., Rathinamoorthy, R., Ganesan, P. (2015) Sustainable Luxury Natural Fibers—Production, Properties, and Prospects. *Handbook of Sustainable Luxury Textiles and Fashion*. Gardetti, M.A., Muthu, S.S. (eds); Springer, Singapore.
- [4] Ortega, Z., Morón, M., Monzón, M.D., Badalló, P., Paz, R. (2016) Production of Banana Fiber Yarns for Technical Textile Reinforced Composites. *Materials*, 9, 370.
- [5] Aziz, N.A.A., Ho, L-H., Azahari, B., Bhat, R., Cheng, L-H., Ibrahim, M.N.M. (2011) Chemical and functional properties of the native banana (*Musa acuminata* balbisiana Colla cv. Awak) pseudo-stem and pseudo-stem tender core flours. *Food Chemistry*, 128, 748–753.
- [6] Subagyo, A., Chafidz, A. (2020) Banana Pseudo-Stem Fiber: Preparation, Characteristics, and Applications. *Banana Nutrition - Function and Processing Kinetics*. Jideani, A.I.O., Anyasi, A.T. (eds.); IntechOpen.
- [7] Assis, F.S., Margem, F.M., Cordeiro, T.C., Figueiredo, A.B-H., Braga, F.O., Monteiro, S.N. (2015) Photoacoustic Thermal Characterization of Banana Fibers. *Materials Research*, 18(2), 240–245.
- [8] FAO (2023) <https://www.fao.org/faostat/en/#data/QCL/visualize> [Accessed 4 November 2023].
- [9] Mumthas, A.C.S.I., Wickramasinghe, G.L.D., Gunasekera, U.S.W. (2019) Effect of physical, chemical and biological extraction methods on the physical behaviour of banana pseudo-stem fibres: Based on fibres extracted from five common Sri Lankan cultivars. *Journal of Engineered Fibers and Fabrics*, 14, 1–15.
- [10] Venkateshwaran, N., ElayaPerumal, A., Arwin Raj, R.H. (2012) Mechanical and dynamic mechanical analysis of woven banana/epoxy composite. *Journal of Polymers and the Environment*, 20, 565–572.
- [11] Akatwijuka, O., Gepreel, M.A-H., Abdel-Mawgood, A., Yamamoto, M., Saito, Y., Hassanin, A.H. (2022) Overview of banana cellulosic fibers: agro-biomass potential, fiber extraction, properties, and sustainable applications. *Biomass Conversion and Biorefinery*.

- [12] Deepa, C., Ramesh, M. (2022) Banana fibers, their composites and applications. *Plant Fibers, their Composites, and Applications*. Rangappa, S.M., Parameswaranpillai, J., Siengchin, S., Ozbakkaloglu, T., Wang, H. (eds); Elsevier, Cambridge, USA.
- [13] Ahmad, T., Danish, M. (2018) Prospects of banana waste utilization in wastewater treatment: A review. *Journal of Environmental Management*, 206, 330–348.
- [14] Badanayak, P., Jose, S., Bose, G. (2023) Banana pseudostem fiber: A critical review on fiber extraction, characterization, and surface modification. *Journal of Natural Fibers*, 20(1), 2168821.
- [15] Xu, S., Xiong, C., Tan, W., Zhang, Y. (2015) Microstructural, Thermal, and Tensile Characterization of Banana Pseudo-stem Fibers Obtained with Mechanical, Chemical, and Enzyme Extraction. *BioResources*, 10(2), 3724–3735.
- [16] El-Meligy, M.G., Mohamed, S.H., Mahani, R.M. (2010) Study mechanical, swelling and dielectric properties of prehydrolysed banana fiber – Waste polyurethane foam composites. *Carbohydrate Polymers*, 80, 366–372.
- [17] Idicula, M., Malhotra, S.K., Joseph, K., Thomas, S. (2005) Dynamic mechanical analysis of randomly oriented intimately mixed short banana/sisal hybrid fibre reinforced polyester composites. *Composites Science and Technology*, 65, 1077–1087.
- [18] Idicula, M., Boudenne, A., Umadevi, L., Ibos, L., Candau, Y., Thomas, S. (2006) Thermophysical properties of natural fibre reinforced polyester composites. *Composites Science and Technology*, 66, 2719–2725.
- [19] Elseify, L.A., Midani, M., El-Badawy, A.A., Seyam, A-F.M., Jawaid, M. (2023) Benchmarking automotive nonwoven composites from date palm midrib and spadix fibers in comparison to commercial leaf fibers. *Biomass Conversion and Biorefinery*.
- [20] Unal, F., Avinc, O., Kumartasli, S., Yavas, A. (2021) The use of banana fibers in composite materials. XII International Conference Textile Science and Economy, 10th December, Zrenjanin, Serbia.
- [21] Murali Mohan Rao, K., Mohana Rao, K. (2007) Extraction and tensile properties of natural fibers: Vakka, date and bamboo. *Composite Structures*, 77, 288–295.
- [22] Geethamma, V.G., Thomas Mathew, K., Lakshminarayanan, R., Thomas, S. (1998) Composite of short coir fibres and natural rubber: effect of chemical modification, loading and orientation of fibre. *Polymer*, 39(6-7), 1483–1491.
- [23] Vishnu Vardhini, K.J., Murugan, R. (2017) Effect of Laccase and Xylanase Enzyme Treatment on Chemical and Mechanical Properties of Banana Fiber. *Journal of Natural Fibers*, 14(2), 217–227.

- [24] Pothan, L.A., Oommen, Z., Thomas, S. (2003) Dynamic mechanical analysis of banana fiber reinforced polyester composites. *Composites Science and Technology*, 63, 283–293.
- [25] Subramanya, S.R., Satyanarayana, K.G., Pilar, B.S. (2017) Evaluation of Structural, Tensile and Thermal Properties of Banana Fibers. *Journal of Natural Fibers*, 14(4), 485–497.
- [26] Paul, S.A., Boudenne, A., Ibos, L., Candau, Y. (2008) Effect of fiber loading and chemical treatments on thermophysical properties of banana fiber/polypropylene commingled composite materials. *Composites: Part A*, 39, 1582–1588.
- [27] Teli, M.D., Valia, S.P. (2013) Acetylation of banana fibre to improve oil absorbency. *Carbohydrate Polymers*, 92, 328–333.
- [28] Bledzki, A.K., Faruk, O., Sperber, V.E. (2006) Cars from Bio-Fibres. *Macromolecular Materials and Engineering*, 291, 449–457.
- [29] Joana Rodríguez, L., Ospina, S., Ribeiro, I., Peças, P., Orrego, C.E. (2021) Banana fibre-biocomposite applied to bottle lid case - life-cycle engineering model for material selection. *International Journal of Sustainable Engineering*, 14(5), 1181–1192.
- [30] Grace Annapoorani, S. (2018) Sustainable Textile Fibers. *Sustainable Innovations in Textile Fibres*. Muthu, S.S. (ed.); Springer, Singapore.



PRINT CIRCUIT

*Damla SAĞLAM*¹

*Sevcan AYTAÇ*²

1 *Fırat University, Department of Biotechnology, Elazığ*

e-mail: damlasaglam99@gmail.com

Orcid: 0009-0001-2031-4862

2 *Fırat University, Department of Electronics and Automation, Elazığ*

e-mail: saytac@firat.edu.tr

Orcid: 0000-0001-6689-2337

Introduction

Plates in which electronic circuit elements or electronic components are mounted on the upper side of the copper plate surface and the electrical connection between these circuit elements is provided by means formed on the copper surface, are called printed circuit boards. A part of the printed circuit copper surface in most electronic systems is melted to create copper vias, and the circuit elements are connected to each other via these copper vias.

1. The purpose of the printed circuit

- a) Combining electronic circuit elements,
- b) To ensure electrical connection between circuit elements.

Board insulator is also a non-flexible material. (There are also flexible PCBs) The thin connection paths seen on the board are the part of the conductive copper that covers the surface of the entire board at the very beginning of the production sequence. After determining the exact location of these conductive copper circuit elements, the rest is erased in different ways. A circuit is created from the remaining copper paths. These remaining copper paths are defined as the Conductor Pattern and complete the electrical connection between the electronic circuit elements that will be placed on the printed circuit.

There are masks attached to the printed circuit board in blue, red, green or brown. The mask used is a protective layer that protects the copper paths and prevents the circuit elements where the soldering is done from touching places other than the connection points. Screen printing is done on the solder mask. Printed circuit elements are written and marked on the printed circuit with the locations of various circuit elements to be assembled. It is also expressed as legend.

2. Printed Circuit Structure

Printed circuit board; It is a card with insulating, flat and rigid structures, with layers containing circuit elements and thin copper paths. The layers are solder mask, screen printing, FR4, copper; They were strengthened together with heat and adhesive. Choosing other materials instead of FR4 in low-quality printed circuit types causes the durability of the printed circuit to significantly decrease. Another layer is made of thin copper foil material and a quality printed circuit is located on both sides of the substrate. In order to prevent the copper paths from coming into faulty contact with other circuit elements, the solder mask on the copper plate gives the printed circuit board red or green colors. Thanks to the screen printing

layer, ease of assembly is ensured and indicators such as numbers and symbols are added to the printed circuit board.

3. Things to Consider When Making Printed Circuits

- When making a printed circuit, we must first try to choose a plate that is suitable for the dimensions of the electronic circuit elements that need to be included in the circuit. Because creating the circuit and selecting the plate without measuring the dimensions of the circuit elements would be a wrong choice.
- We must ensure that circuit elements such as diodes and resistors are mounted horizontally, and similar circuit elements such as capacitors, transistors, regulator ICs are mounted vertically on the copper plate.
- Since some circuit elements have three legs, when placing the elements on the copper plate, we must take the necessary measurements, determine the appropriate width and mount them accordingly.
- If it is necessary to use a cooler on the copper plate to prevent the circuit elements mounted on the copper plate from heating up, we must take the necessary measurements and reserve enough space in the cooler on the copper plate.
- The location of the circuit elements to be adjusted, such as potentiometers and trimmer capacitors, must be determined in a way that the adjustment point can be reached and placed accordingly.
- We must take care to make the paths of the circuit elements that draw high current on the copper plate thicker. Otherwise, that path will be damaged and we will not be able to get efficiency from the copper plate.

4. How to Make an Electronic Printed Circuit?

Materials used

- Copper plate in dimensions appropriate to the printed circuit diagram
- Iron
- PNP or coated paper
- sponge
- Liquid soap
- Perhydrol acid

- Salt spirit
- Acetate pen
- Paper tape
- Plastic container in which we can place the plaque horizontally

After obtaining the materials required to perform the printed circuit board process, we can proceed with the process steps carefully and orderly. After deciding where our circuit elements should be and animating them to fit on the plate, the first step is to create a template from the computer with the help of the drawing program. The reverse image of the drawing we created on the computer is printed on coated paper or PNP from a laser printer. The point we need to pay attention to at this stage is that the output is of high quality and error-free. To ensure this, the toner of the printer we use must be of high quality.

In the second step of our printing circuit, the surface of the copper plate prepared in accordance with the size of the circuit diagram is thoroughly cleaned with sponge and liquid detergent. In another step, the front side of the printout printed on coated paper should be aligned with the front side of the copper plate. In this phase, we must adjust the copper plate and coated paper very carefully and regularly. In order to minimize our margin of error in this phase, we can fold the edges of the coated paper to the back of the copper plate and tape them with paper tape. There should be no slipping on the copper plate.

We moved on to the ironing process, which is the most difficult step of the printed circuit board process. It is essential to do the ironing process without adding water. If water is put into the iron, we may damage the coated paper due to the steam. The ironing step should take between 7 or 10 minutes. We should keep the iron on the copper plate wrapped in coated paper by applying pressure for 7 or 10 minutes. If you wait for the plate to cool for 3 minutes after the waiting process is completed, we will achieve a more successful removal result. Then we need to carefully separate the coated paper from the copper plate. We need to be very careful when performing the separation process because in this process, the drawing on the coated paper forms the paths on the copper plate. The paths on the copper plate should not be damaged. Now that we have removed the copper plate and coated paper, we will have to draw the paths that are missing or do not fit on the copper plate ourselves. The printed circuit diagram and the existing printed circuit should be brought side by side and compared, and the missing areas should be completed with an acetate pen. At the same time, if there are unnecessary places and short circuits, we must separate

them. What we need to do now is to erase the copper except for the paths on the copper plate.

5. Use of Acid in Printed Circuit Making

Important points for acid use

1. Acid treatment should not be done in a closed environment.
2. Acid treatment should be carried out in an environment with plenty of air.
3. It is strongly recommended that those with asthma or shortness of breath do not do this.
4. After the plaque is thrown into the acid, it should not be left unattended.
5. Gloves should be used during the acid process.
6. Perhirol or salt spirit should not be touched.
7. If one of these substances accidentally gets on your skin, it should be washed immediately with plenty of water.

When we throw the copper plate in acid while making a printed circuit, we should not leave it longer than necessary. If the copper plate is left in acid for longer than necessary, it may melt on the paths we draw with the acetate pen, which will cause the copper plate to stop working. The moment the copper plate is thrown into the acid should be kept for a minute and it should be removed in a controlled manner within 5-10 minutes. When the copper plate is placed in acid, gently shaking it intermittently allows us to get a more effective result.

When the other coppers, except for the roads on the copper plate, melt, cleaning is done with the help of plenty of water and liquid detergent. After the cleaning process of the copper plate is completed, the places where the circuit elements will be placed are checked, the necessary marks are placed and drilled with a drill.

6. Printed Circuit Board Types

6.1. Single Sided Cards

In this type of board, the components are placed on one surface of the board and the conductor pattern is placed on the opposite surface. Since there is only one conductor pattern, this type of PCBs are called Single-Sided. Copper has a limited ability to create conductor patterns by opening paths (since only one surface is used, the paths cannot intersect and must be routed around each other). This type of boards is used in simple circuits.

6.2. Double Sided Cards

This type of board has a pattern of conductors on both sides. Having two conductor patterns requires a special type of electrical connection between the two. This type of electrical bridges are called “via”. A via is a hole on the PCB that is filled (or coated) with metal and contacts the pattern of conductors on both sides. Double-sided PCBs are much more suitable for complex circuits than single-sided PCBs, as the area allocated to the conductor pattern is twice as large as that of single-sided boards, and because the wire prints can cross each other (directing them to different surfaces). For easy design of Double-Sided PCBs, it is easier to divide one surface into vertical lines and the other surface into horizontal lines. (Signal and Power line)

To attach the components to the PCB, the legs of the components are soldered to the Conductor Pattern. In most simple PCBs (Single-sided boards), components are placed on one side of the board and the Conductor Pattern is placed on the other side. In DIP Materials, there must be holes in the PCB for the component legs to enter the board. Therefore, the legs are soldered to the PCB from the side opposite to where the components are placed. That’s why the top and bottom surfaces of a PCB are referred to as “Component Surface” and “Solder Surface” respectively.

6.3. Printed Circuit Board Advantages and Usage Areas

Printed circuits offer us multiple advantages compared to normal cable circuits. Printed circuits have mechanical advantages such as durability, less heating, and minimal cable usage. The assembly of printed circuit boards is simpler than normal circuits and provides the opportunity to design engineering applications more easily and freely. It also reduces the size of electronic devices by simplifying the circuit elements. It also has advantages such as ease of maintenance and repair and reducing electrical noise in high-frequency circuits. Mass production of electronic devices has also accelerated significantly with the use of printed circuits.

6.4. PCB Drawing Programs

- Proteus (ares+isis)
- Protel
- Eagle
- Altium Desinger
- OrCad

Kaynakça

[https://www.elektrikport.com/makale-detay/baski-devre-karti-\(pcb\)-nedir/23040#ad-image-0](https://www.elektrikport.com/makale-detay/baski-devre-karti-(pcb)-nedir/23040#ad-image-0)

<https://diyot.net/baski-devre/>

<https://teslaakademi.com/baski-devre-nasil-yapilir>



A PRECISION LANDING STUDY ON VERTICAL LANDING ROCKET WITH NEEDLE-VALVE COLD GAS PROPELLANT SYSTEM

*Onur DUMAN*¹

*Engin DEMİRYAY*²

*Umutcan BİLER*³

*Arzum İŞİTAN*⁴

1 Pamukkale University, Faculty of Engineering, Mechanical Engineering Department, 20160, Denizli, Türkiye, onurdumantr@gmail.com , ORCID: 0009-0002-4650-3482,

2 Pamukkale University, Faculty of Engineering, Mechanical Engineering Department, 20160, Denizli, Türkiye, engindmryay@gmail.com , ORCID: 0009-0005-8077-590X,

3 Pamukkale University, Denizli Vocational School of Technical Sciences, Computer Programming, 20160, Denizli, Türkiye, blrumutcan64@gmail.com , ORCID: 0009-0005-7854-9444,

4 Assoc. Prof. Dr., Pamukkale University, Faculty of Technology, Mechanical Engineering Department, 20160, Denizli, Türkiye, aisitan@pau.edu.tr , ORCID: 0000-0002-5228-9788.

1. Introduction

With its recent investments and significant defense industry products, the Republic of Türkiye has advanced significantly. In this context, the manufacturing of rocket and missile systems, the foundation of the space and defense industries, is crucial both domestically and nationally.

When we look at the history of rockets, the first written records of which date back to around 400 BC, we see that it is a phenomenon that has not diminished in interest for mankind for approximately 2000 years. Rockets are still the most important and only resource we must make going to space and traveling in space happen (NASA, 2021; Taylor, 2017). Figure 1 shows the microsatellite launch system developed by Roketsan (Roketsan, 2023).



Figure 1. *A microsatellite launch system developed by Roketsan*

Typically, rockets are machines that shoot hot gas in the opposing direction of motion to accelerate and acquire speed. Rockets are usually cylindrical in shape with a tip designed to reduce air friction. They can reach high speeds thanks to the large thrust they provide. Rocket engines can achieve high speeds due to the large propulsion force they provide. The process steps here can be expressed simply as follows: First, the fuel (solid or liquid) in the engine is ignited by an ignition system or by self-ignition, the chemical energy of the fuel is converted into heat energy to form gases with high pressure and temperature, and these gases are expanded and accelerated in the nozzle at the back of the rocket and expelled from the

system (İçöz, 2010; Arıcan, 2003).

Therefore, the main elements in a rocket can be listed as the fuel, which constitutes 90-95% of the rocket weight and will enable the reaction to occur, the combustion chamber where the fuel burns, the igniter material that will initiate the combustion of the fuel, and the hole (nozzle) from which the gas formed as a result of combustion is sprayed out (Arıcan, 2003).

The factors to be taken into consideration in rocket design and production, together with payload, range, and radius of action, are as listed below (İçöz, 2010):

1. Weight, volume, and power of the rocket fuel,
2. Rocket shape,
3. Weight of the rocket,
4. Weight and volume of the payload,
5. Weight and power of rocket engines,
6. Atmosphere and gravity resistance,
7. Trajectory of the charge.

There could possibly be differences between the military and civilian definitions of a rocket. “*An unguided projectile that is guided by a weapon system to a specific target and flies unguided towards that target*” is the definition of a rocket in the military, nevertheless, in the context of civilian life, anything can be considered a rocket whether it is guided. Rockets launched from land to air, from air to air, from sea to land and into the air have been made for military purposes. To move the required equipment from one location to the intended destination, rockets are utilized. The term “payload” refers to this equipment, which has a variety of uses (e.g., satellite, experimental or scientific research tools, drone transportation, etc.). If a rocket is used for astronautic purposes, it is called a carrier or launcher. If it is used for military purposes, that is, if the payload it carries is for destructive purposes, it is called a missile (Roketsan, 2020).

1.1. Basic Concepts and Definitions

Although rocket and missile elements vary according to their intended use, they most generally consist of fuel, payload/ammunition, and nozzle. In the combustion chamber of the rocket engine, it is theoretically possible to use all chemical elements or compounds as oxidants and fuel (Keskin et al., 2016; Arıcan, 2003). As a result, the four main components of a full-scale rocket can be listed as structural system or frame, payload system, guidance system, and propulsion system. A rocket's propulsion system includes all parts that make up the rocket engine, pumps, propellants, power-head, and rocket nozzle (NASA, 2023).

Rocket engines play the most important role in the use of rockets for various purposes inside or outside the atmosphere by providing high thrust and high speeds. Since a vehicle powered by a rocket engine carries all of its own propellant, it can be used in air, water, or space, regardless of the environmental environment (Lyon, 1991). Rocket engines can be classified according to the type of energy source used (chemical, nuclear, or solar), basic function (aircraft engine, missile engine, assisted take-off engine, spacecraft engine, etc.), size, propellant type, construction type, number of stages, or number of engines used in a vehicle. The most common classification is the types of rocket engines according to their energy source (Lyon, 1991; Arıcan, 2003).

Rocket engines can also be classified as follows (Rao, 1961; Arıcan, 2003; İçöz, 2010):

- a. *Chemical Fuel Rockets (engines using solid and liquid fuel),*
- b. *Electric Rocket Engines (engines designed to convert electrical energy either directly or into other types of energy),*
- c. *Electro Thermal Engines (Powered by electrical energy without an explosion),*
- d. *Electrostatic Motors (Ion Motors) (the atoms ionized by electricity are produced by electric and magnetic fields),*
- e. *Electromagnetic Motors (Plasma Motors) (turning gas into plasma),*
- f. *Solar Radiation Propulsion Engines (engines in which thrust force is obtained by heating hydrogen gas after collecting solar energy and focusing it at a point),*
- g. *Nuclear Engines (engines that are thought to yield energy by converting hydrogen into helium with a proton-proton chain and have not yet been realized),*

h. *Electric Rockets (engines using electric propulsion systems).*

Rocket engines can operate using liquid or solid propellants, or a combination of the two (Haidn, 2008). Engines that use solid and liquid fuel are called *Chemical Engines* (Arıcan, 2003). In *solid fuel rockets*, the oxidizing agent is contained in the fuel. The combustion of solid propellant engines is very complex and the burning rate of the solid fuel is one of the most important design criteria (Yaman et. al, 2014). It is a simple, low-cost, and safe system. Since the chemical and physical phenomena occurring during combustion are not fully understood, and since the combustion of the fuel cannot be stopped in solid propellant rockets, they are not preferred in space missions for now (Arıcan, 2003). *Liquid rockets*, which in many cases have onboard propulsion systems that have a significant impact on the characteristics of space systems and their overall mission performance, are used for a variety of functions in many commercial, military, and NASA space systems (Schneider, 1992). The propellant delivery devices, the propellant injection system, the thrust chamber, the thrust nozzle, the turbines, pumps, and generators of the driving gasses are the essential components of a liquid propellant rocket engine (Chehroudi, 2012). While liquid rocket motors allow simultaneous adjustment of oxidizer and fuel depending on the oxidizer-to-fuel ratio, solid rocket motors require adjustment of the propellant and oxidizer particle configuration. *Hybrid rocket motors*, on the other hand, are a system that has components in both phases, i.e. liquid oxidizer and solid fuel, or vice versa, to achieve the required thrust (Oztan, 2021).

While conventional rocket engines generate thrust by burning chemical fuel, *electric rockets* apply electric or electromagnetic fields to accelerate clouds of charged particles or plasmas to propel the rocket. Chemical rockets are capable of burning large amounts of fuel, quickly generating large amounts of thrust, and reaching high speeds. These characteristics make them more suitable for short-distance travel. Although electric rockets produce much less thrust, they consume less fuel and can reach high speeds over longer distances, especially in the frictionless environment of space. (Choueiri, 2009). Studies on electric thrusters are progressing in two directions (Dale, 2020):

- a. *increasing the specific thrust and longevity of high-power technologies,*
- b. *Improving the efficiency and reliability of low-power technologies.*

If the required electric power provided from *solar energy*, solar radiation propulsion engines can be used for trips to the inner solar system. In long distances where solar energy is weak, the use of *nuclear energy* is almost essential.

In a rocket engine, propellants, fuel, and oxidizer burn at high pressure and temperature to produce thrust. *Rocket thrust* is the reaction force produced by the high-velocity ejection of solid, liquid, or gaseous particles or even radiant energy beams through a nozzle opening. High thrust systems are systems that store energy in the propellant and allow the propellant to be used to overcome gravity, as in a planetary launch vehicle, or to quickly accelerate a vehicle already in space, i.e., for an orbital ejection maneuver (Leishman, 2023). Some high thrust systems are listed below:

- a. *Dual-fuel systems*, which can be gas/liquid, solid, or hybrid, are the fastest way to convert propellant energy (for example, launching the NASA Space Shuttle or SpaceX Falcon 9) (Leishman, 2023).
- b. *Monopropellant engines* produce thrust by flowing unburned propellant gas through a valve into a catalytic decomposition chamber, where the propellant undergoes a high-energy exothermal decomposition process and by acceleration of hot gases through a nozzle (Leishman, 2023).
- c. *Cold gas thrusters*, in which compressed gases such as nitrogen or helium are released from a nozzle to create thrust and there is no combustion, create less thrust than other systems (Leishman, 2023). But the cold gas propulsion system also has many advantages: It is simple in structure, has high reliability, can be operated safely, is small and light, and its useful life in space can be measured in years (Kindracki, 2017).

The concept of *Vertical Landing Rockets* was developed to reduce the cost and time of rocket launch and ensure the reusability of the rocket (Bysani et. al, 2019; Nonaka, 2012). In the very field of space exploration, achieving a precise and well-controlled landing is crucial, especially if the system is accommodating sensitive instruments.

One of the key technologies contributing to this precision is the flow control mechanisms that finely tune the output levels of the system. In this study, a lander with a cold gas thruster system was designed and manufactured to ensure both vertical descent control by regulating velocity and position in space, and a reaction control system to maintain the lander at a vertical attitude to the ground. The cold gas propellant system is quite complex, encompassing subsystems such as software and hydraulics that need to work together and synchronously.

Needle valves are precision flow control devices used to regulate the fluid flows in applications where fine control and accuracy are essential. The valve features a needle-like stem with a tapered tip inserted into a

conical seat in the flow medium. By adjusting the position of the needle, the flow rate of fluid can be precisely controlled without causing any significant changes in the feed pressure. Therefore, if the feed pressure is too high to regulate without causing drastic pressure drops, needle valves can be used to control the entirety of flow properties. Thus, if minimizing the mass of the platform is a concern in the design, this method can be preferred as it significantly reduces pneumatic circuit elements.

The central focus of this study revolves around the utilization of needle valves in cold gas thruster systems, addressing a less emphasized aspect of the subject in the literature. Since many applications of cold gas thruster systems adopt a momentarily switching bang-bang control scheme, using a needle valve in those setups would be inappropriate. However, cold gas thruster systems shouldn't stay limited to reaction control maneuvers since they can be used as efficiently as a liquid propellant rocket (Schulte and Spencer, 2016).

This study focuses on the implementation of needle valves while eliminating the need for pressure regulators at the same time to maintain simplicity, which is central to the efficiency of the cold gas thruster system.

2. Design and Manufacturing of Vertical Landing Rocket

2.1. Introduction

Reusable rockets, Vertical Takeoff, Vertical Landing (VTVL) Reusable Launch Vehicles (RLVs), due to their reusability, are now considered the cheaper and most feasible way to access space, with ongoing work in this field (Fari, 2022; Botelho et. Al, 2022; Nonaka et. Al, 2012; Bojun et. al, 2019; Namera et. Al, 2010).

The concept of reusability, albeit partial, has been technologically and commercially proven by SpaceX with the Falcon 9, followed by companies such as Blue Origin and Rocket Lab (Blackmore, 2016; Hoffman et. al, 2022; Botelho et. al, 2022; Fari, 2022; Dongliang et. al, 2019; Bojun et. al, 2019).

For the rocket to be reusable, it must execute a precise landing. Landing is, therefore, the most critical of all recovery steps. Even minor malfunctions can lead to the landing failure. The landing system can be categorized into several types (Braun and Manning, 2006; Dongliang et. Al, 2019):

- a. *retro-rocket*,
- b. *parachute deceleration device*,
- c. *airbag*

d. *the landing legs mechanism.*

Successful landings using parachute deceleration, such as the Viking and Phoenix Mars Rovers, have been achieved (Braun and Manning, 2006; Dongliang et. Al, 2019). The retro-rocket, firing before ground contact, creates reverse thrust, accelerating the vehicle upwards and slowing it down (Lin, 1996; Dongliang et. al, 2019). Landing with an airbag can achieve low impact acceleration, but has poor stability and is likely to kick, bounce, and roll. The landing leg mechanism using a honeycomb bumper enabled the successful soft landing of the Surveyor lunar probe and the Apollo manned lunar module (Liu, 2013; Dongliang et. al, 2019). Designing systems to reduce landing impact and increase stability is crucial for a precise landing.

The main building blocks of a successful landing not only include the mentioned elements above but also a high-quality Guidance, Navigation, and Control (GNC) system, critical for meeting the performance and reliability requirements of VTVL rockets (Fari, 2022).

In the developing aviation and space industry in Turkey, various activities are carried out in the public and private sectors. Different organizations are established to increase young people's awareness, knowledge, and experience in this field. One such initiative is the Teknofest competitions.

This study focuses on the design and manufacturing of the vertical landing rocket developed for Teknofest 2023, considering the mentioned design elements. Teknofest Aviation, Space and Technology Festival, held annually since 2018, aims to raise awareness about aviation, space, and technology, support young enthusiasts, encourage research on future technologies, and familiarize individuals with professional design processes. The Vertical Landing Rocket competition, held for the first time in 2022, distinguishes itself as the world's first Vertical Landing Rocket Competition propelled by the Cold Gas Propulsion System. Teams in the competition are responsible for connecting their designed rocket to a Suspension System and ensuring its controlled descent to the target area using the Cold Gas Propulsion System after release.

This project's central focus is on the utilization of needle valves in cold gas thruster systems, addressing a less emphasized aspect of the subject. While many cold gas thruster systems use a momentarily switching bang-bang control scheme, using a needle valve in those setups may be inappropriate. However, cold gas thruster systems shouldn't be limited to reaction control maneuvers; they can serve as lightweight and reliable thruster systems.

Pamukkale University Hazar Rocket Team won the first prize from TÜBİTAK SAGE at Teknofest 2023. The subsequent sections explain the design, production, and tests of the rocket (ANKA).

2.2. Methodology

The goal is to determine general system requirements and conduct the design, production, and testing processes with teams specializing in Aerodynamics, Avionics, Structural Integrity, and Cold Gas Propulsion for the Teknofest 2023 Vertical Landing Rocket competition. The vertical landing rocket must be released from at least 7 m, and all subsystems must be recoverable and reusable after launch. This includes missile main computer design, control system design, fin design, vane, and controller determination, etc. Figure 2 represents the vertical landing visualization (Teknofest, 2023)

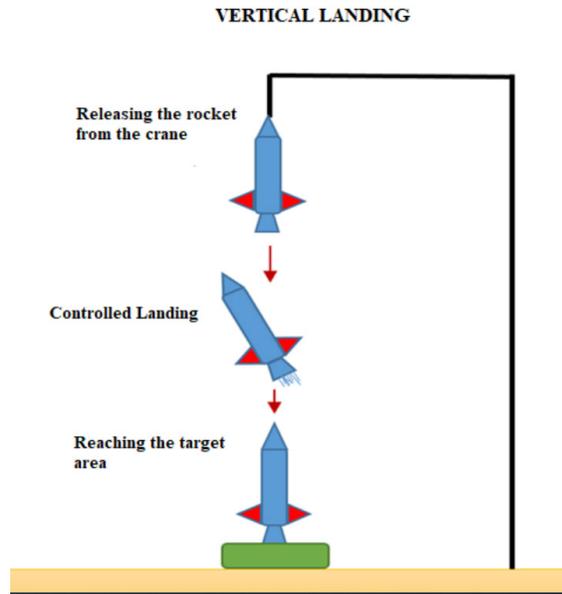


Figure 2. *The vertical landing visualization*

The concept of operation consists for the ANKA rocket involves both pre-flight and flight procedure:

Before the flight

1. Verify that the main supply valves are in the closed position.
2. Check the position of valves in the installation for safe cylinder filling when the rocket is ready.
3. Pressurize the gas cylinder.

4. Set the rocket's main computer to the "ARMED" state.
5. Crane lifts the rocket to the target altitude.

Flight procedure (Figure 3)

1. Release the rocket from the crane (1).
2. Freefall of the rocket (2).
3. Open the valves, provide the first impulse, and control flight (3).
4. Avionics subsystem evaluates the course and actively controls the flight.
5. Gently land in a determined area under a 2 m/s descent velocity (4).

The methodology followed for design and manufacturing includes the following steps:

- Determination of requirements,
- Draft Design aligned with the Operation Concept,
 - o Control Group,
 - o Fluid Group
 - o Landing System,
 - o Body Components,
- Guidance-Navigation-Control Selection,
- Estimated Flight Data and Analysis,
- Propulsion System Determination,
- Creation of Rocket Subsystem Details,
 - o Pneumatic System Design,
 - o Avionics and Actuators Design,
 - o Preliminary Simulations and Design Point Selection,
- Structural Analysis and Structural Tests,
 - o Testing and analysis of mechanical parts,
 - o 6 Degrees of Freedom Flight Simulation,
 - o Guidance Control System,
- Full body integration and assembly.

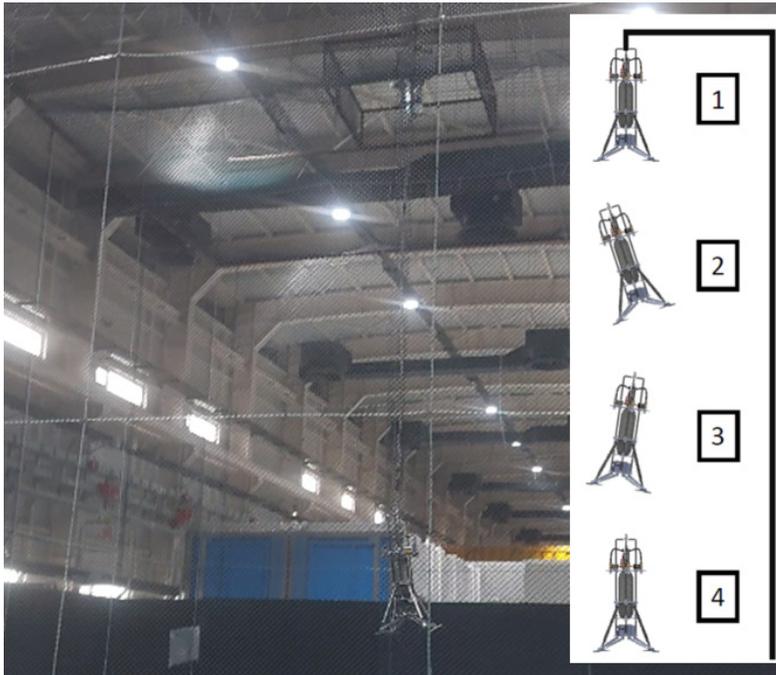


Figure 3. *Flight procedure*

SOLIDWORKS® was utilized for mechanical design, offering easy-to-learn yet powerful functionality to shorten product development time, reduce costs, and improve quality (Solidworks, 2023). Figure 4 represents a draft design of the ANKA. The rocket's chassis was designed with 4 legs for effective landing, considering cylinder tube placement, pneumatic and avionics system placement, and mission requirements. Safety, assembly/disassembly, and changes according to calculations were considered in the design.

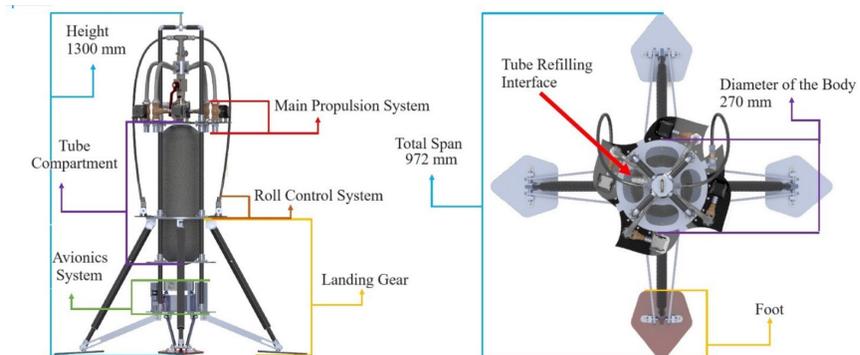


Figure 4. *Draft design of the rocket*

ANKA's guidance, navigation, and control systems were developed based on the 6 Degrees of Freedom Equations of Motion. The initial step

involved defining the Body Fixed Axis Frame and Absolute Axis Frame utilized in the solutions (Figure 5). The body axis frame was established with the center of gravity as the origin, and its axes rotated in tandem with the rocket's movements. The thrust force generated by the nozzles in the simulation was computed within this axis. The algorithm read the values from this axis set and produced outputs, guiding and controlling the rocket's movements accordingly. On the other hand, the absolute axis set considered the initial position and orientation of the rocket as the origin. Environmental factors such as wind, drag, and gravitational acceleration were assumed to act within this set of axes, and the rocket's traveled distance was derived from this frame. To measure changes in altitude, an Inertial Measurement Unit (IMU) sensor and a pressure sensor in the avionics system were employed, utilizing a coupled sensor fusion algorithm. Although it is feasible to calculate displacement solely from acceleration using the IMU, this method is not preferred due to its reliance on moments of motion with noticeable acceleration, posing a higher risk of steady-state error in such scenarios.

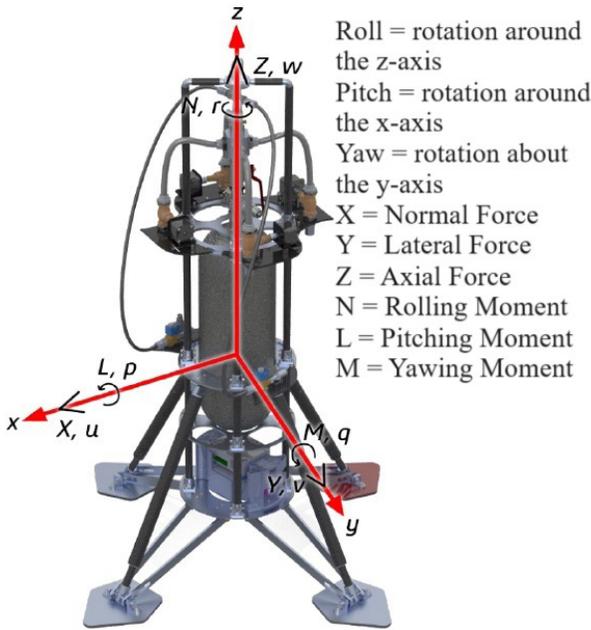


Figure 5. *Coordinate system on the rocket*

The simulation and control were Euler angle-based, and the transformations from the absolute axis to the body axis were achieved through matrix multiplication of the Direction Cosine Matrix from the 6-DOF block and the force vector (Figure 6). The simulation utilized the integral forms of Newton's basic laws of motion as rotational and translational equations of motion. Simulink®, a block diagram environment for multidomain sim-

ulation and Model-Based Design, was employed. It integrates seamlessly with MATLAB®, enabling the incorporation of MATLAB algorithms into models and exporting simulation results to MATLAB for further analysis (MathWorks, 2023).

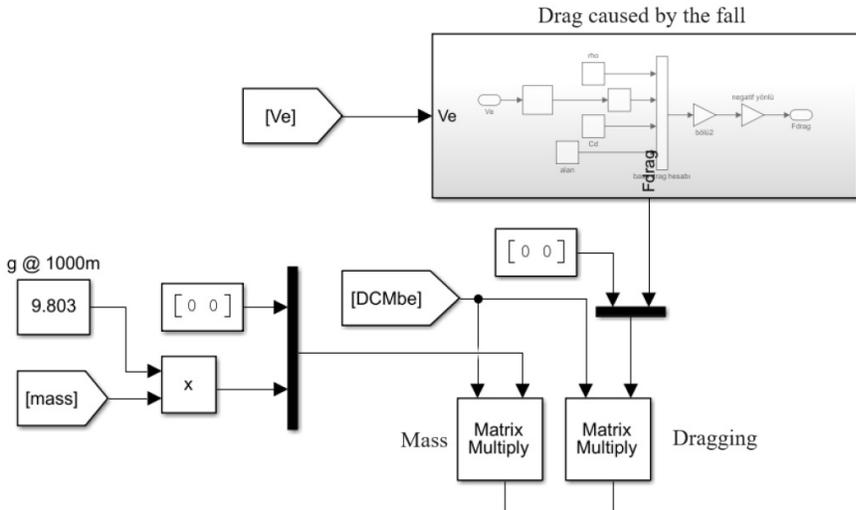


Figure 6. Axis transformation

The forces and moments resulting from environmental effects primarily stem from gravitational acceleration and aerodynamic effects. In the context of aerodynamic effects, these include moments, lateral and normal forces influenced by the angle of attack α and the sideslip angle β . Additionally, the aerodynamic drag force contributes to an axial drag force resulting from a combination of viscous force and a force perpendicular to the rocket's direction. As the competition was specified to occur indoors, no wind or turbulence model was designed. Air density was assumed based on the average altitude of Ankara above sea level. Given that the rocket's mass decreases with each second of gas sprayed through the nozzles to generate thrust, the change in mass is modeled in relation to the opening of the valves. Consequently, the total mass's state is calculated instantaneously in the simulation, with mass flow rates changing based on control orders throughout the flight (Figure 7).

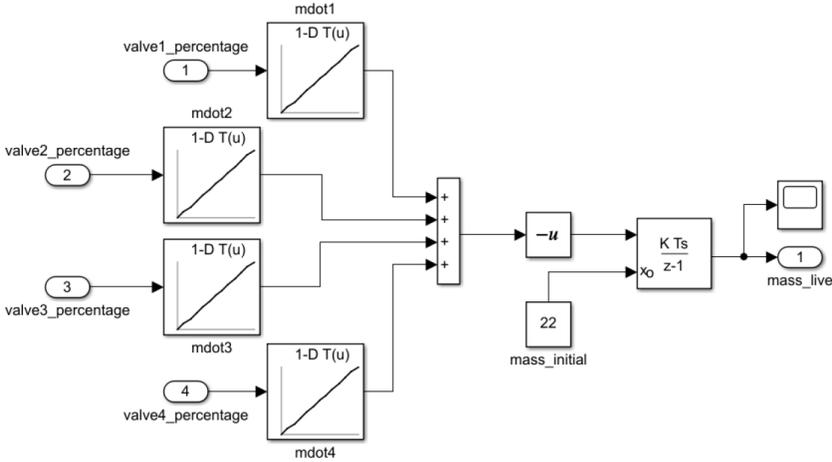


Figure 7. Mass reduction algorithm

2.3. Mechanical Design

The mechanical structure and guidance control system are depicted in Figure 8. In terms of body components, carbon rods were crafted using the pre-preg method, employing carbon fiber. Bulkheads were manufactured from aluminum through CNC machining. CNC-machined aluminum elements were utilized to secure the carbon rod to the bulkhead. The nozzle for the cold gas propulsion system was constructed from aluminum, while the manifold was made of steel. Rubber and sponge materials were employed at points where the tank contacts the chassis, and for sealing, o-rings and Teflon tape were utilized.

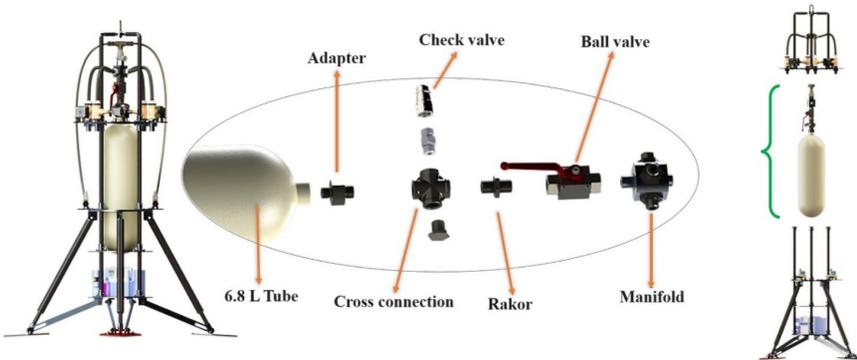


Figure 8. Mechanical structure of ANKA

The mechanical aspect of the landing system is illustrated in Figure 9. The legs comprised a suspension fixed to the upper body and two aluminum rods affixed to the lower body, allowing movement along the ver-

tical axis. The compression amount of the spring in the suspension was calculated, and a channel was cut into the aluminum rod to direct excess force after spring compression to the moving rods. The suspension body was produced by wrapping 1mm thick carbon fiber around a 2-mm wall thickness aluminum tube.

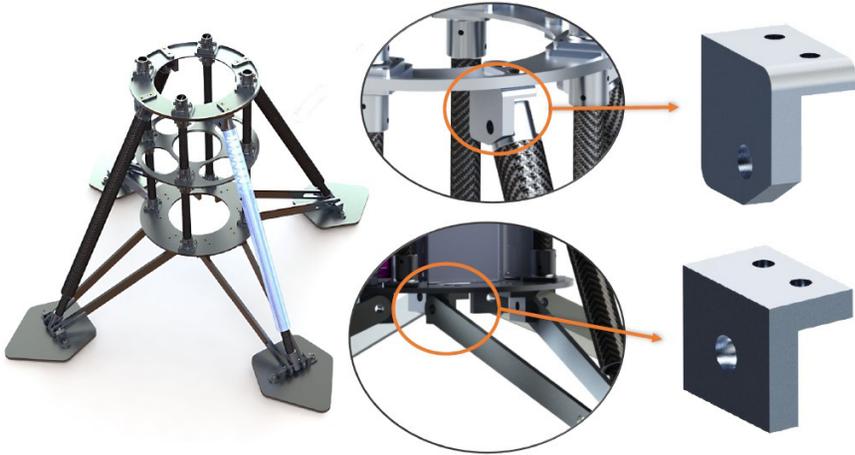


Figure 9. *Landing system mechanical view*

2.4. Guidance Control System

The operating logic of the guidance control system for Pitch and Yaw axes involves throttling or opening the gas to the nozzles through needle valves located at the heads of the four nozzles within the main propulsion system. For the roll axis, only the solenoid valve at the head of the two nozzles isolated to the roll axis is manipulated, being opened and closed with PWM modulation. In the case of the Pitch and Yaw axes, the PID control is saturated to provide a variable torque output ranging between -2.42 and 2.42 Nm (Figure 10). Since a solenoid valve is employed in the roll axis instead of a needle valve, a PI controller was designed instead of PID. Moreover, this controller oversees the roll angular velocity, not the roll angle. Consequently, even if the rocket rotates on the roll axis, it does not attempt to return to the initial position but works solely to reset the angular velocity. This condition is exclusively applicable to the roll axis.

Main Propulsion Control System (Figure 11), Pitch and Yaw controllers (Figure 12), and Roll controller block diagram (Figure 13) were developed using Simulink®.

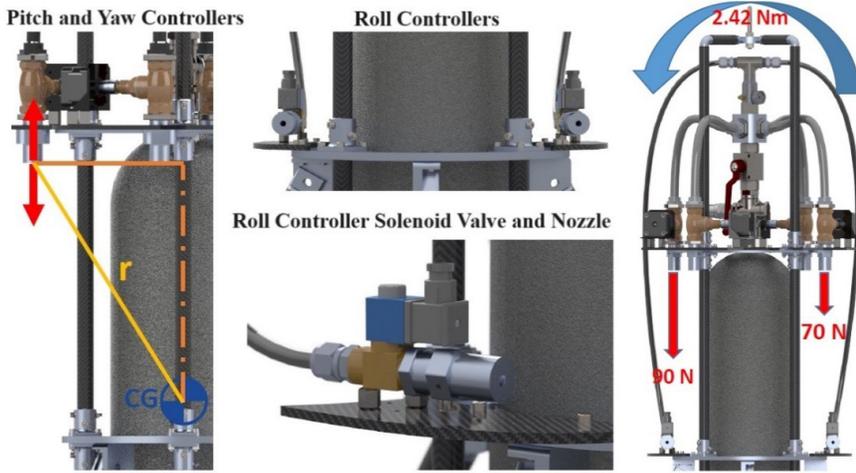


Figure 10. Guidance Control Regarding Axes

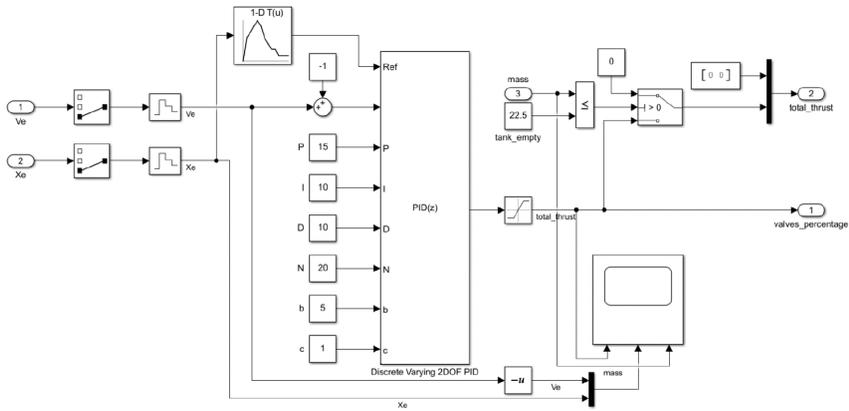


Figure 11. Main Propulsion Control System

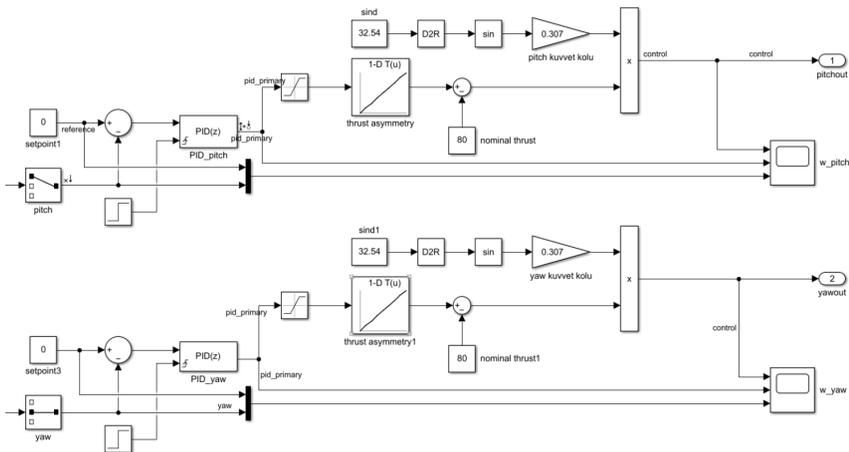


Figure 12. Pitch and Yaw controllers

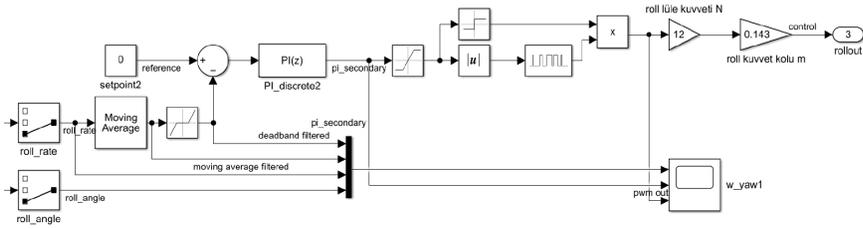


Figure 13. Roll controller

2.5. Cold Gas Thruster System

The cold gas propulsion system, although considered somewhat outdated, has been employed for attitude control and precision maneuvers, finding use even in modern spacecraft like SpaceX’s Falcon 9. In contrast to conventional chemical propulsion systems relying on propellant combustion, cold gas thrusters utilize compressed, inert gases such as nitrogen or dry air. The design adopted in this study eliminates the need for complex fuel combustion procedures, resulting in a simpler and more reliable system under various conditions. However, it’s important to note that cold gas thrusters generally exhibit lower efficiency and performance compared to liquid propellant alternatives. While approaches like using hydrogen can enhance performance, the challenges associated with hydrogen compression diminish its advantage (SpaceX, 2021).

The efficiency of the cold gas thruster system in this study is central to the implementation of needle valves, eliminating pressure regulators simultaneously for the sake of simplicity. Needle valves are precision flow control devices crucial for regulating fluid flows in applications where fine control and accuracy are paramount. Featuring a needle-like stem with a tapered tip inserted into a conical seat in the flow medium, these valves enable precise control of fluid flow rate by adjusting the needle’s position without causing significant changes in feed pressure. When feed pressure is too high to regulate without causing drastic pressure drops, needle valves can be employed to control overall flow properties precisely. This method is advantageous for minimizing platform mass in the design, as it significantly reduces pneumatic circuit elements (Hutton and Boaden, 1986). Figure 14 provides a CAD render of a needle valve (Hyfindr, 2023).



Figure 14. *CAD render of a needle valve, image by Hyfindr*

The description outlines that cold gas propulsion systems are predominantly employed for vehicle orientation control, with limited exceptions for specific projects. The approach in this study aims to develop a vehicle achieving a soft landing solely through the force generated by the cold gas propulsion system. This is intended to evaluate the effectiveness of traditional methods in meeting ANKA's goals and explore alternative capabilities.

In the context of this study, the common structures found in widely used cold gas propulsion systems are elucidated. Typically, these systems comprise a high-pressure gas tank, a pressure regulator, solenoid valves for control, and various sensors. While these systems are commonly utilized in satellites for tasks like orbit adjustments and orientation control, the low thrust levels generated by such configurations are usually adequate for these purposes. It's noted, however, that these conditions are applicable mainly in orbit or microgravity environments.

The primary distinction in ANKA's approach lies in its different objectives compared to traditional satellite systems. While satellite systems aim for long-lasting, economical, and safe mechanisms, ANKA focuses on achieving high thrust levels without combustion. The study begins by investigating the element in the system that restricts thrust to only a few Newton levels. Tests and analyses, starting with the production of replicas of systems used in satellites, reveal that many pressure regulators inherently control the mass flow rate of the gas passing through them. This inherent control limits the achievable thrust, emphasizing the need for a solution related to the regulator to overcome this limitation. The applied force in the system is directly proportional to the amount of mass accelerated, following Newton's laws of motion (U.S. Naval Ordnance Laboratory, 1950).

The challenge with traditional cold gas propulsion systems lies in the fact that regulators providing higher mass flow permeability are bulkier and heavier. As the complexity of the regulator increases to support itself, it also needs to generate more thrust, leading to decreased efficiency and increased system weight. Additionally, regulators with higher flow permeability, beyond a certain point, render the system unusable. This is because the lowest pressure setting of the regulator may surpass the limits of the operating conditions of many solenoid valves, including heavier types. The pressure regulator and solenoid valve combination prove to be a viable approach only in low-thrust systems. Therefore, the development of a new method beyond traditional approaches is crucial to achieving a high thrust-to-weight ratio in cold gas propulsion systems.

As a result of a trial-and-error process, the concept of completely eliminating the pressure regulator from the system was conceived. In this scenario, where the system inevitably reaches a pressure range much higher than solenoid valves can handle, the search for a valve that could be both quickly controlled like solenoid valves and withstand high pressures led to the decision to use needle valves. Needle valves, due to their structure, do not have a pressure resistance limit derived from the mechanism. Operating conditions depend only on the basic pressure resistance of the material they are made of, which, when made from aerospace-grade stainless steel, can easily control flows at a feed pressure of 300 bar.

By simplifying the system significantly and minimizing pressure loss in transitions between elements, this method requires only as many needle valves and actuator sets as the number of thrusters, making it very lightweight. Thus, the thrust-to-weight ratio of the system reaches levels where active controlled vertical descent, and even the application of the suicide burn method, becomes feasible. Meanwhile, since the actuators can operate proportionally, unlike many solenoid valves, precise control is achieved much more effectively. These actuators work by proportionally turning the valve knob according to the control order.

Figure 15 presents the pneumatic circuit design. In line with the operating scenario (main drive system inlet total pressure 63 bar, RKS (ROLL axis) inlet total pressure 30 bar), thrust nozzles were selected. Flow, pressure, temperature, velocity, and thrust formulas for the nozzles were derived, and pneumatic system elements were selected: tube nozzle, sleeve, ball valve, needle valve, interconnection fitting, thermoplastic tubing, etc.

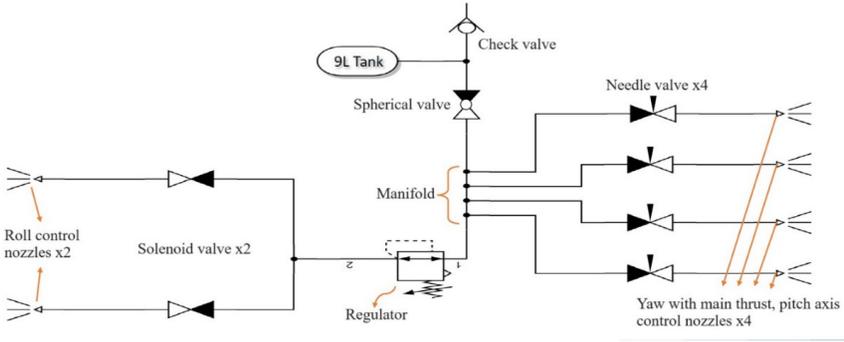


Figure 15. *Pneumatic circuit design*

2.6. Assembly

The carbon rods in the chassis are mounted to the aluminum bulkheads by means of spacers. The assembly of the body components is shown in Figure 16.

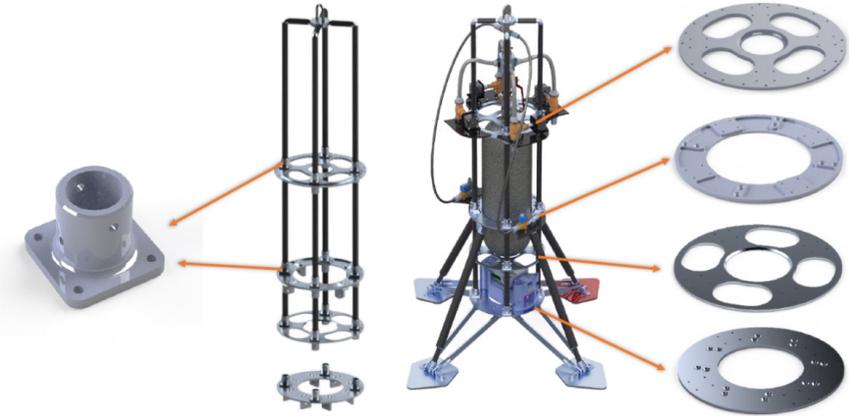


Figure 16. *The assembly of the body components*

The main thrust actuator assembly is presented in Figure 17. After the integral bonnet needle valve is seated on the upper bulkhead, Nema 17 motor and 3/8 thermoplastic hose are attached to the needle valve with coupling, and then the nozzle is mounted to the needle valve.



Figure 17. *The main thrust actuator assembly*

In the positioning of the pneumatic circuit in the rocket, the thrust generating elements are not too far away from the main chassis, thus minimizing unwanted vibration and flexing (Figure 18).

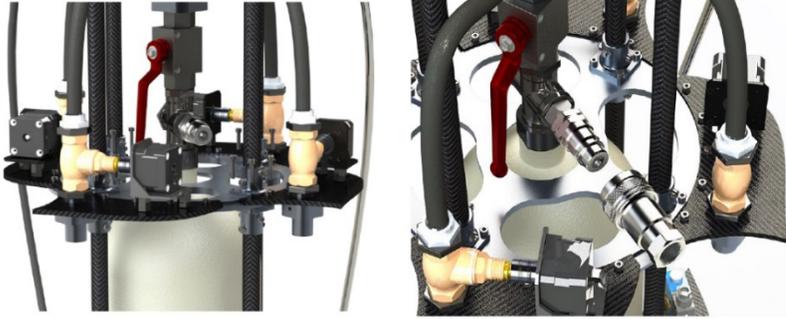


Figure 18. *The pneumatic circuit assembly*

2.7. Tests

Following the assembly, the necessary tests of ANKA were carried out at Hazar Team laboratories and Denizli Municipality Fire Department. An image of the cold gas thruster thrust test at Hazar Laboratories is shown in Figure 19.

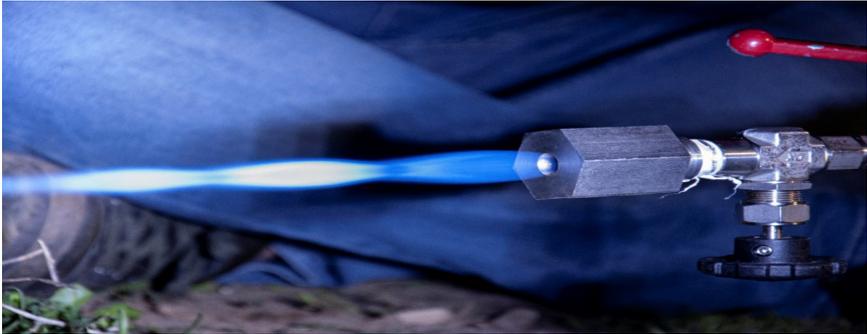


Figure 19. A thrust test of cold gas thruster in Hazar Labs.

Computational Fluid Dynamics Analyses of the Main Propulsion System Nozzles were performed in the ANSYS Fluent program. Ansys Fluent is the fluid simulation software known for its advanced physics modeling capabilities and industry leading accuracy (ANSYS, 2023). Figure 20 shows an image from the analysis of the Velocity contour (top) and Temperature contour (bottom). Figure 21 shows an image from the analysis of the thrust curve based on the valve turn count.

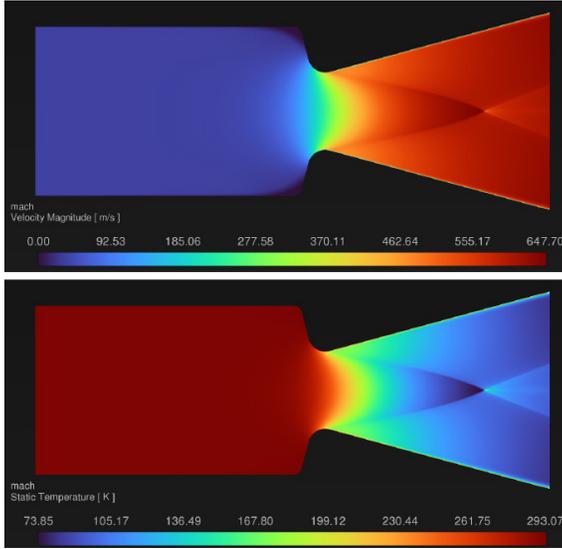


Figure 20. An image related computational fluid dynamics analyses

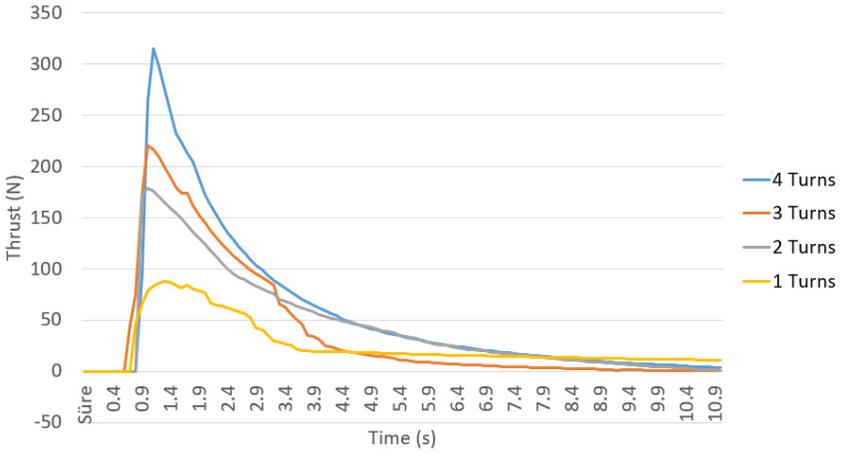


Figure 21. An image of the thrust curve based on the valve turn count analysis

3. Results

The test data shown in Figure 21 presents the thrust obtained from a system containing only a needle valve, directly fed with dry air at 300 bars from a gas tank. As there is only a single nozzle in these test data, essentially supplied with maximum flow, the practical maximum thrust levels of the nozzles are sought to be observed by omitting the manifold used in the actual platform. In this context, needle valves positioned in the open state at different turn counts in different tests are rapidly fed with gas by the quick opening of the preceding spherical valve, and the thrust formation is observed by supplying the flow it can pass to the nozzle. In this test, since mass choking already occurs in the nozzle, the thrust obtained when the flow is divided into 4 nozzles using a manifold remains quite close to the individual nozzle thrust in the graph. Only the duration of this thrust has shortened due to the rapid consumption of gas pressure with the 4-nozzle setup.

As a result of this R&D project, it can be seen that cold gas propulsion systems are not bound to be used only in attitude control but can also be used as main thrusters for a vertically landing rocket.

Acknowledgement

This study was supported by the Scientific Research Coordination Unit of Pamukkale University under project numbers 2023LÖKAP008 and 2022LÖKAP016. The authors thanks the Denizli Municipality Fire Department.

References

- ANSYS (2023). Ansys Fluent Fluid Simulation Software, <https://www.ansys.com/products/fluids/ansys-fluent> Accessed 16 December 2023.
- Arıcan, M.M. (2003). Havayla Çalınan Bir Roket Motoruyla Taşıt Tahriğinin İncelenmesi, Doctoral dissertation, İTÜ Fen Bilimleri Enstitüsü.
- Blackmore, L. (2016). Autonomous precision landing of space rockets. In *Frontiers of Engineering: Reports on Leading-Edge Engineering from the 2016 Symposium* (Vol. 46, pp. 15-20). Washington, DC: The Bridge.
- Bojun, Z., Zhanchao, L., Gang, L. (2019). High-precision adaptive predictive entry guidance for vertical rocket landing. *Journal of Spacecraft and Rockets*, 56(6), 1735-1741.
- Botelho, A., Martinez, M., Recupero, C., Fabrizi, A., & De Zaiacomo, G. (2022). Design of the landing guidance for the retro-propulsive vertical landing of a reusable rocket stage. *CEAS Space Journal*, 14(3), 551-564.
- Botelho, A., Martinez, M., Recupero, C., Fabrizi, A., De Zaiacomo, G. (2022). Design of the landing guidance for the retro-propulsive vertical landing of a reusable rocket stage. *CEAS Space Journal*, 14(3), 551-564.
- Braun, R. D., Manning, R. M. (2006). Mars exploration entry, descent and landing challenges. In *2006 IEEE Aerospace Conference* (pp. 18-pp). IEEE.
- Bysani, S. K. K., Karpur, A., Arun, N. (2019). Vertical Landing Rockets. In *TMAL02 Expert Conference* (Vol. 8, No. 4, pp. 33-34).
- Chehroudi, B. (2012). Recent experimental efforts on high-pressure supercritical injection for liquid rockets and their implications. *International Journal of Aerospace Engineering*.
- Choueiri, E. Y. (2009). New dawn for electric rockets. *Scientific American*, 300(2), 58-65.
- Dale, E., Jorns, B., Gallimore, A. (2020). Future directions for electric propulsion research. *Aerospace*, 7(9), 120.
- Dongliang, W., Qifeng, C., Luohaijun, L. M. (2019). A Landing Buffer System for Vertical Takeoff and Vertical Landing Reusable Launch Vehicle. In *Proceedings of the 8th European Conference for Aeronautics and Aerospace Sciences (Eucass)*, Madrid, Spain (pp. 1-4).
- Falcon User's Guide, SpaceX, September 2021 <https://www.spacex.com/media/falcon-users-guide-2021-09.pdf> Accessed 16 December 2023.
- Fari, S. (2022). The Vertical Landing Vehicles Library (VLVLib): a Modelica-based approach to high-fidelity simulation and verification of GNC systems for reusable rockets. In *Proceedings of the International Astronautical Congress*, IAC.
- Haidn, O. J. (2008). Advanced rocket engines. *Advances on propulsion technology for high-speed aircraft*, 1, 6-1.

- Hoffman, L., Baker, M., Glynn, S., Darley, M., Beck, P. (2022). Reusable Electron: Analysis of Progress Toward the World's First Reusable Commercial Small Rocket.
- Hutton, P., Boaden, R. W. (1986). Performance of needle valves. *British journal of anaesthesia*, 58(8), 919-924.
- Hyfindr (2023). <https://hyfindr.com/marketplace/components/valves/needle-valves/screwed-bonnet-needle-valve-h-99-series/> Accessed 16 December 2023.
- İçöz, G. (2010). Raket ve füzelerin hedefe yönlendirilmesi için gerekli kontrol ve güdümlenme sistemlerinin analitik incelenmesi, Master's thesis, Trakya Üniversitesi Fen Bilimleri Enstitüsü.
- Keskin, H., Dinçkurt, M., Mertcan, M.U.T., Özdamar, A. (2016). Füze ve Raket Teknolojisinde Son Gelişmeler, *Makine Teknolojileri Elektronik Dergisi*, 13(4), 111-129.
- Kindracki, J., Tur, K., Paszkiewicz, P., Mężyk, Ł., Boruc, Ł., & Wolański, P. (2017). Experimental research on low-cost cold gas propulsion for a space robot platform. *Aerospace science and technology*, 62, 148-157.
- Leishman, J. G. (2023). *Rockets & Rocket Propulsion. Introduction to Aerospace Flight Vehicles*.
- Lin, B.H. (1996). Overview of Landing Buffer Technology. *Spacecraft Recovery & Remote Sensing*, 03:1-16.
- Liu, X.Y. (2013). Stability simulation analysis of soft landing buffer for Lander. PhD Thesis. Hunan University
- Lyon, J.M. (1991). Introduction to rocket propulsion. US Army Missile Command.
- MathWorks (2023). Simulink Simulation and Model-Based Design, <https://www.mathworks.com/help/simulink/> Accessed 16 December 2023.
- Namera, Y., Takaki, R., Oyama, A., Fujii, K., Yamamoto, M. (2010). Aerodynamic shape design of the vertical landing rocket vehicle. In 28th AIAA Applied Aerodynamics Conference (p. 4367).
- NASA (2021). Brief History of Rockets, https://www.grc.nasa.gov/www/k-12/TRC/Rockets/history_of_rockets.html#:~:text=The%20date%20reporting%20the%20first,of%20a%20solid%2Dpropellant%20rocket Accessed 16 December 2023.
- NASA (2023). <https://www1.grc.nasa.gov/beginners-guide-to-aeronautics/rocket-parts/#:~:text=There%20are%20four%20major%20systems,system%2C%20and%20the%20propulsion%20system> Accessed 16 December 2023.
- Nonaka, S., Nishida, H., Kato, H., Ogawa, H., Inatani, Y. (2012). Vertical landing aerodynamics of reusable rocket vehicle. *Transactions of the Japan Society for Aeronautical and Space Sciences, Aerospace Technology Japan*, 10, 1-4.

- Oztañ, C., Coverstone, V. (2021). Utilization of additive manufacturing in hybrid rocket technology: A review. *Acta astronautica*, 180, 130-140.
- Rao, G.V.R. (1961). Recent developments in rocket nozzle configurations. *ARS journal*, 31(11), 1488-1494.
- Roketsan (2020). <https://www.roketsan.com.tr/tr/urunler/mikro-uydu-firlatma-sistemi> Accessed 16 December 2023.
- Roketsan (2023). https://www.roketsan.com.tr/uploads/docs/1628594512_20.03.2020model-roketcilik-master-dokumanv04.pdf Accessed 16 December 2023.
- Schneider, S.J. (1992). Advanced liquid rockets. In JANNAP Propulsion Meeting (No. E-6976).
- Schulte, P. Z., Spencer, D. A. (2016). Development of an integrated spacecraft guidance, navigation, & control subsystem for automated proximity operations. *Acta Astronautica*, 118, 168-186.
- Solidworks (2023). Solidworks 3D CAD, <https://www.solidworks.com/tr/product/solidworks-3d-cad> Accessed 16 December 2023.
- Taylor, T.S. (2017). Introduction to rocket science and engineering. CRC Press.
- Teknofest2023 (2023). Vertical Landing Rocket Competition Specifications Document, https://cdn.teknofest.org/media/upload/userFormUpload/Sartname_2023_EN_V10_XyOAz.pdf Accessed 16 December 2023.
- U.S. Naval Ordnance Laboratory (1950). Supersonic Nozzle Design (Project NOL 159).
- Yaman, H., Çelik, V., Değirmenci, E. (2014). Experimental investigation of the factors affecting the burning rate of solid rocket propellants. *Fuel*, 115, 794-803.



RECENT TRENDS IN ADDITIVE MANUFACTURING OF CARBON REINFORCED POLYMER COMPOSITES

Assoc. Prof. Dr. Tuba ÖZDEMİR ÖGE¹

Asst. Prof. Dr. Mecit ÖGE²

Inst. Dr. Firdevs Banu ÖZDEMİR³

1 Bartın University, Bartın University, Faculty of Forestry, Department of Forestry Industry Engineering, Bartın, Turkey. E-mail: tozdemir@bartin.edu.tr, ORCID ID, 0000-0001-6690-7199.

2 Bartın University, Faculty of Engineering, Architecture and Design, Department of Mechanical Engineering, Bartın, Turkey; E-mail: mecitoge@bartin.edu.tr, ORCID ID, 0000-0001-5243-0828.

3 Kütahya Health Sciences University, Simav Vocational School of Health Sciences, Department of Medical Services and Techniques, Kütahya, Turkey; E-mail: firdevsbanu.ozdemir@ksbu.edu.tr, ORCID ID, 0000-0002-7935-2062.

1. Introduction

In the last decades, carbon reinforced polymer composites have received huge interest from both industrial and academic research domains due to the countless new possibilities introduced by the advances in polymer blending as well as integration of various type of fillers to further enhance several properties of polymers and their blends such as mechanical, electrical, thermal, electromagnetic shielding properties and so on (Akin et al., 2014). Recently, this trend is even further boosted by the advent and incorporation of additive manufacturing technologies into the domain of polymers and polymer based composite materials, which has brought a whole new aspect into the production and application of polymer-based materials. Among various types of fillers, which can be roughly categorized in accordance with their natural and synthetic nature, carbon-based fillers might have drawn most of the research interest, due to the outstanding electrical and physical properties attained by the composite materials filled with carbon-based fillers. Thermoplastic polymer composites are initially prepared by methods such as melt compounding, in situ polymerization and intercalation methods. Conventionally, the produced polymer nanocomposites in semi-product form are used to attain the desired shape by plastic injection or compression molding methods. After the additive manufacturing technology was introduced into the realm of polymer blends and composites, 3D printing became the new alternative for forming these types of materials. Thus, the additive manufacturing (AM) or 3D printing technology, has evolved from single material AM, which was mainly concerned with additive manufacturing of single thermoplastic components such as polylactic acid (PLA), polyamides (PA6, PA66, PA12), poly (ethylene terephthalate) (PET-G), etc., into multi-material AM for production of the blends and composites of these and other polymers as the possibility of additive manufacturing of polymer composites was explored. From the early beginnings of additive manufacturing of polymer materials, fused deposition modeling (FDM) or fused filament fabrication (FFF) technique has been the widely adopted method for 3D printing of polymers and their composites.

This study aims to provide an overview of recent research attempts on additive manufacturing of carbon reinforced polymer composites. Prior to introducing the recent works, the readers will be provided with a brief insight into the 3D printing technologies used in the production of polymer-based materials, commercially available polymers for FDM, carbon-based fillers used in 3D printed polymer composites, and finally a literature survey on 3D printed carbon reinforced polymer composites will be introduced.

2. Common 3D Printing Technologies Used in Production of Carbon Reinforced Polymer Composites

The advent of additive manufacturing technologies has gained an unprecedented speed due to its compatibility and integration with Industry 4.0 technologies as it is directly related to data-driven manufacturing. Thanks to the additive manufacturing technologies, Industry 4.0 requirements such as versatility, flexibility and fast supply chains can be easily fulfilled as this technology offers countless possibilities such as rapid product and prototype development, compared to conventional plastic injection and other molding techniques, which is crucial for many key high-tech industries such as aviation, automotive and petrochemistry. Moreover, the application of additive manufacturing technologies has been extended to the production of metal and cement-based materials, which can be deemed as a cornerstone in the advent of industrial revolutions. From the viewpoint of carbon reinforced polymer composites, which is the subject of this work, AM technologies can be listed as follows:

Fused Deposition Modeling (FDM): This technique uses polymers in filament form as feedstock material heated up to their melting point and extruded through a nozzle for layer by layer deposition of the heated material as per its digitized model through a software (Masood, 2014.) The ease of application, and the cost efficiency of the technique and the feedstock material have rendered FDM process the most widely adopted and utilized AM technique in all research fields and industries. The FDM technique is also highly compatible for preparation of carbon reinforced polymer composite samples and products in relatively short periods as compared to conventional molding techniques despite some drawbacks such as inferior mechanical properties. Thus, most of the research on additive manufacturing of CNCs aims to improve the inferior characteristics of 3D printed composites compared to their molded counterparts.

Stereolithography (SLA):

This AM technique is also referred to as vat photopolymerization and it uses a light-emitting device to cure a liquified photopolymer (a light sensitive thermosetting resin) via a UV light, UV laser or visible light, so that the product is formed layer by layer (Najmon, et al., 2019; Shirvan et al., 2021). In this method, as the polymer resin is exposed to the UV or visible light, the monomers and oligomers merge and form a solid structure through layer by layer deposition (Shirvan et al., 2021). The main advantage of this technique is its ability to form fine details with a superior surface finish by eliminating the stepping effect of arising in other methods (Shirvan et al., 2021).

Selective Laser Sintering (SLS): This is a powder-based AM technique which uses a laser source for melting and consecutive fusion of powders, thus layer by layer forming the printed component in accordance with its digital 3D model. In this method, the quality of the printed product mainly relies on the design and preparation of the feedstock powder (Gan et al., 2020). The main advantage of this technique is its capability to produce large components with decent mechanical properties in a relatively cost-efficient way. It has been applied in many fields such as rapid prototyping of non-critical aerospace components, in manufacturing biomedical components (Najmon, et al., 2019), and so on.

Other 3D printing technologies involve Selective Laser Melting (SLM), Liquid Deposition Modeling (LDM), material jetting and binder jetting techniques (Valino et al., 2019). When compared to conventional molding techniques used for manufacturing of polymers, their blends and composites, additive manufacturing techniques are advantageous as they do not require the preparation of a mold which is a costly and a quite time consuming process, whereas conventional molding techniques are advantageous over AM in terms of production speed and the physical properties of the end-products. However, injection molding of polymer nanocomposites has some drawbacks such as inhomogeneous dispersion of the fillers stemming from high viscosity of matrix components, leading to quality issues for the end-products (Valino et al., 2019).

2.1 Commercially Available Polymers for FDM

The most common thermoplastic polymers commercially available for FDM filaments are polylactic acid (PLA), polyamide (Nylon), acrylonitrile butadiene styrene (ABS), polyethylene terephthalate (PET), thermoplastic polyurethane (TPU), acrylonitrile styrene acrylate (ASA), poly-ether-ketone (PEEK) and so on. Although, these materials provide the users with high thermal and mechanical performance, their high temperature processing demands may not be handled by ordinary 3D printing systems, and they are relatively costly. Due to such considerations, researchers from academic and industrial domains have been in search of tailoring and improving the polymer matrix properties by blending with different matrices or incorporating natural or synthetic fillers.

2.2 Carbon-Based Fillers Used in 3D Printed Polymer Composites

Owing to their superior properties such as outstanding electrical conductivity, mechanical attributes stemming from their aspect ratio etc., carbon-based fillers have been the subject of countless academic and industrial research attempts for quite a time. As other fillers used for reinforcement

of polymer matrices, carbon-based or carbonaceous fillers can be roughly categorized as those with and without nano-dimensions. Those at least with one nano-dimension are referred to as carbonaceous nanofillers and their structure can be one, two or three dimensional (Mittal, 2015). Depending on their size, geometry and other physical properties, carbonaceous nanofillers can be listed as fullerene, carbon black (CB), multiwalled carbon nanotube (MWCNT), single-walled carbon nanotube (SWCNT) and graphene nanoplatelets (GNPs). Other carbonaceous fillers involve carbon fiber, graphite and its derivatives such as graphite oxide, graphene, expanded graphite, etc. (Kaşgöz2014). Composites 3D printed by carbonaceous fillers are the subject of several research studies on enhancement of various properties of polymer matrices and blends.

3. Recent Studies on 3D Printing of Carbon Reinforced Polymer Composites

Many considerations such as the directionality of the filler within the 3D printed matrix as well as several 3D printing parameters are effective on the final properties of the printed material, which have been the focus of most research attempts in this field. Aside from these considerations, other design parameters such as the blend ratio, filler ratio, inclusion of modifiers and other additives for toughening or other strengthening purposes are among the other considerations addressed in such works. Some of the recent works involving the additive manufacturing of carbon filler reinforced polymer composites are summarized below.

Das et al. (2023) used graphite particles to reinforce polyvinyl alcohol (PVA) polymer matrix and performed rheological tests to determine the viscosity's effect on the printability of the prepared ink. They employed varying needle/nozzle diameters resulting in varying flow rates to determine its effect on output variables as particle orientation, distribution, mechanical properties, and porosity. They also utilized Discrete Element Method (DEM) and computational fluid dynamics (CFD) analysis to validate the experimental process. They gained a good correlation between the theoretical and experimental results and reported that, a better particle alignment along the flow direction was attained with higher volume flow rates. The authors also report that, 3D printing technique is a promising method compared to conventional manufacturing techniques in terms of enhancing the mechanical properties of the produced materials in a controlled way (Das et al., 2023).

Dickson et al. (2017) conducted a study on evaluation of the performance of continuous carbon, Kevlar and glass fiber filled nylon matrix composites using FDM technique. They evaluated the tensile and flexural performance of the produced samples and reported that the composites

filled with carbon fiber demonstrated the highest increase in mechanical strength and further reported that, the tensile strength of the reinforced samples were up to 6.3 times higher than that of the neat samples. Reportedly, the increase in carbon and glass fiber filler ratio induced the inclusion of air into the matrix, and consequently, the highest efficiency in terms of tensile strength was achieved in the case of glass fiber inclusion (Dickson et al., 2017).

Gao et al. (2023) investigated the relation between the rheological properties and the structure of a polymer matrix (polyetherketoneketone (PEKK)) composite reinforced with a 2D filler (mica). In their work, they systematically studied the effect of various filler attributes such as filler size and content, shear rate and surface chemistry. Reportedly, stronger interaction between the matrix and the filler increases the shear stress between the constituents which resulted in a higher viscosity. They concluded that, controlling the rheology of polymer-2D filler systems via modifying the surface chemistry of the filler is a promising method for designing innovative feedstocks for extrusion based AM. (Gao et al., 2023).

Karaş et al (2022) presented a novel approach for manufacturing of discontinuous fiber reinforced polymer composites with mechanical properties superior to those achieved with modern AM techniques. Reportedly recent AM approaches generally suffer from high porosity with up to 25% which is a major drawback when compared to conventionally manufactured products that feature 1% porosity. Their technique (composite fiber additive manufacturing (CFAM)) involves controlled deposition of binder and polymer powder onto the sheets of discontinuous fiber, followed by compressing, heating and post-processing to attain the final shape. They report that, the composite samples manufactured in this way contained 1.5% porosity at a filler ratio of 15%, with 8.9 GPa elastic modulus and 97 MPa tensile strength (Karaş et al., 2022).

Le et al. (2023) produced 3D printed carbon fiber reinforced polymer (CFRP) composites having bioinspired Bouligand structures mimicking Coelacanth fish scales. Reportedly, such bioinspired structures have been promising candidates to improve the mechanical properties of CFRPs. In this regard, the authors prepared single and double Bouligand meso-structures and examined their flexural and fracture behavior, and concluded that, the twist angle within the Bouligand configurations affected the extent of fracture toughness. Moreover, twist angles of the bioinspired configurations also affected the flexural behavior of the specimens to a large extent. Also, when compared with the quasi-isotropic meso structure, the Bouligand meso-structures did not lead to an increase in elastic fracture and fracture toughness energies for crack initiation (Le et al., 2023).

Huang et al. (2020) proposed a 3D printing-based approach for CFRP recycling which involved recycling of CFRPs by reclamation of carbon fibers using supercritical n-butanol, and processing the reclaimed carbon fibers with 3D printing after mixing them with poly-ether-ketone (PEEK) powder and extruding to obtain composite filaments. They compared the mechanical and electrical performance of the 3D printed samples with those of neat PEEK samples and reported that, additive manufacturing approach for recycling CFRPs had a great potential for reutilization of waste CFRPs and rapid fabrication of reclaimed CF reinforced polymer composites (Huang et al., 2020).

As an attempt for predicting fiber orientation in 3D printed strand in for extruded polymer composites, Kermani et al. (2023) developed a computational fluid dynamics (CFD) model for the material extrusion process. For this purpose, they simulated the deposition process of both fiber and the polymer suspension from nozzle tip of the printer in a layer by layer fashion. To assess the effects of printing parameters they varied the nozzle-substrate distance, gap size, nozzle head speed, the suspension's shear thinning behavior, initial fiber orientations and fiber interactions. After comparing the simulation results with previous experimental results, they concluded that CFD simulation could be used as a potential slicing tool for enhancement of strand-strand adhesion and the resulting mechanical properties (Kermani et al., 2023).

Another attempt for recycling of polymer composites by additive manufacturing approach was made by Korey et al. (2023) who recycled additively manufactured carbon fiber reinforced acrylonitrile butadiene styrene (CF-ABS) used for concrete castings by an industrial scale shredding/granulating system. They found that, the mechanical properties of the recycled composites were reduced due to the loss of carbon fiber while during the printing process degradation of the polymer matrix was also observed induced by the thermomechanical nature of the extrusion process. Nevertheless, they reported that, the recycled composite feedstock retained enough mechanical properties for its reutilization as concrete casting molds in the field. (Korey et al., 2023).

Lian et al. (2023) studied the printing parameters for CFRP composites 3D-printed under magnetic field control (MFC) which enables the controlling of fiber orientation for optimizing the structural performance of CFRPs. They assessed the mechanical properties and fiber orientations of the produced samples by varying the printing speeds and layer thicknesses. They reported the optimum MFC assisted printing parameters for composites with 10% fiber content as 40 mm/s and 0.2 mm, respectively (Lian et al. 2023).

Liu et al. (2023) proposed a novel method additive manufacturing of chopped carbon fiber reinforced SiC (Cf/SiC) composites, a key high temperature resistant structural material for military and aerospace applications, by introducing an innovative direct ink writing (DIW) technique through incorporation of pyrolysis and polymer infiltration processes. Reportedly, the Cf/SiC samples with 30 wt% Cf content exhibited a high bending strength with negligible linear shrinkage, and the pyrolysis process enabled the filling of structural defects leading to an about 30 times higher bending strength for Cf/SiC samples as compared to the non-reinforced SiC matrix (Liu et al, 2023).

Peng et al. (2022) investigated the deformation and compression behaviors of innovative FDM printed triply periodic minimal surface (TPMS) gyroid structures made of FRP composites. After theoretically and experimentally examining the effect of printing direction, unit cell quantities, and the relative density on the printed samples' mechanical properties, they reported that the gaps between the printed layers led to reduced elastic modulus values when the FRP gyroid structures were loaded in parallel to the printing direction. The authors concluded based on the obtained results that, 3D printing of TPMS gyroid structures are promising candidates for future applications demanding functional lightweight structures (Peng et al., 2022).

Saeed et al. (2022) examined the properties of FDM printed continuous carbon fiber reinforced polyamide-based composites with different fiber ratios. They held the samples under pressure and temperature in a platen press and evaluated the synergistic effect of short and continuous CFs, as well as the effect of pressing process on the tensile and flexural behaviors of the 3D-printed samples. They concluded that, increasing fiber content significantly improved the mechanical properties, and hot pressing after 3D printing also contributed to the enhancement of mechanical properties by reduction of voids (Saeed et al., 2022).

Wang et al. (2021) proposed a finite element method (FEM) based approach the relationship between non-Newtonian melt flow of polymers and orientation of fibers during the 3D printing of polymer composites. Reportedly, the fully-coupled solution for flow fields differed significantly from the weakly-coupled results, and concluded that the calculated results revealed the significance of examination of fully-coupled flow-fiber orientation interactions in polymer composite deposition additive manufacturing (PCDAM) processes (Wang and Smith., 2021).

Yap et al. (2023) examined the tensile and fracture behavior, crystallinity, fiber orientation and fiber length and porosity of polyaryletherketone (PAEK) composites reinforced with short carbon fibers 3D-printed with

material extrusion (ME) and laser powder bed fusion (L-PBF) methods. They reported after their examinations that, PAEK samples 3D printed via FFF method exhibited anisotropic properties to a higher extent than those of the selective laser sintering (SLS) printed samples. Reportedly, the most significant roles of fibers for both ME and L-PBF printed samples was enhancement of the sample's stiffness along the printing direction. They also concluded that, their results would aid designers in manufacturing high performance components with complex shapes using different 3D printing technologies (Yap et al., 2023).

4. Conclusion

The above brief overview of recent attempts on investigating the various properties of 3D printed carbon filled composite materials show that, the majority of the research studies focus on 3D printing of carbon fiber reinforced polymer composites (CFRPs) either with novel 3D printing approaches or innovative material design considerations, and either by varying the composite content or by altering the printing parameters. Few studies on 3D printing of polymer nanocomposites are encountered and none of these used the FDM technique for deposition of nanofiller reinforced polymer composites. This can be ascribed to the thermomechanical requirements of the process for the feedstock material for its deposition at high temperature, as well as the agglomeration, dispersion and homogeneity related issues for polymer nanocomposites which might be a limiting factor in terms of rheological considerations for 3D printing process. Nevertheless, this unexplored area is likely to be visited when the attempts on eliminating such drawbacks are initiated by scholars. There is also an emerging trend towards validation of the experimental data with theoretical CFD computations, application of post-processing techniques to eliminate the defects such as voids arising from 3D printing processes, and in-depth examinations such as establishing relationship between the melt flow and orientation of fillers. Overall, the recent studies show that, the research domain of additive manufacturing of carbon reinforced polymer composites is yet to be fully explored, with countless possibilities and gaps in the literature. The great potential of additive manufacturing combined with the extensive knowledge on polymer nanocomposites attained so far is likely to put this subject in the focus of academic and industrial interest in the near future.

REFERENCES

- Akın, D., Kasgoz, A., Durmuş, A. (2014). “Quantifying microstructure, electrical and mechanical properties of carbon fiber and expanded graphite filled cyclic olefin copolymer composites”, *Composites: Part A*, 60, 44-51.
- Das, M., Mishra, R., Das, P., Kashyap, S., K., Panda, S. K., Mitra, R., Owuor, P.S., Arora, A., Tiwary, C., S. (2023). “Controlled directionality in 3D printing of graphite-reinforced polymer composite with enhanced mechanical properties”. *Composite Science and Technology*, 235, 109955.
- Dickson, A.N., Barry, J.N., McDonnell, K.A., Dowling, D.P. (2017). “Fabrication of continuous carbon, glass and Kevlar fibre reinforced polymer composites using additive manufacturing”. *Additive Manufacturing*, 16, 146-152.
- Gan, X., Fei, G., Wang, J., Wang, Z., Lavorgna, M., Xia, H. (2020). “Powder quality and electrical conductivity of selective laser sintered polymer composite components” in Structure and Properties of Additive Manufactured Polymer Components, *Woodhead Publishing*, 149-185.
- Gao, P., Muller, S.E., Chun, J., Zhong, L., Kennedy, Z.C. (2023). “Effects of 2D filler on rheology of additive manufacturing polymers: Simulation and experiment on polyetherketoneketone-mica composites”. *Polymer*, 269, 125722.
- Huang, H., Liu, W., Liu Z. (2020). “An additive manufacturing-based approach for carbon fiber reinforced polymer recycling”. *CIRP Annals-Manufacturing Technology*, 68, 33-36.
- Karaş, B., Smith, J.P., Fairclough, J.P.A., Mumtaz, K. (2022). “Additive manufacturing of high density carbon fibre reinforced polymer composites”. *Additive Manufacturing*, 58, 103044.
- Kaşgöz, A., Akın, D., Ayten, A., İ., Durmuş, A. (2014). “Effect of different types of carbon fillers on cyclic olefin copolymer (COC) composites.” *Composites: Part B*, 66, 126-135.
- Kermani, N.N., Advani, S.G., Ferec, J. (2023). “Orientation predictions of fibers within 3D printed strand in material extrusion of polymer composites”. *Additive Manufacturing*, 77, 103781.
- Korey, M., Rencheck, M.L., Tekinalp, H., Wasti, S., Wang, P., Bhagia, S., Walker, R., Smith, T., Zhao, X., Lamm, M.E., Copenhaver, K., Vaidya, U., Ozcan, S. (2023). *Composites Part B*. “Recycling polymer composite granulate/regrind using big area additive manufacturing”. *Composites Part B*, 256, 110652.
- Le, H., Yavaş, D., Wu, D. (2023). “Flexural and fracture behavior of additively manufactured carbon fiber reinforced polymer composites with bioinspired Bouligand meso-structures”. *Composite Structures*, 323, 117436.

- Lian, K., Yang, L., Zhu, D., Gong, X., Zhang, H., Wang, K., Li, J., Yu, W. (2023). "Effect of printing parameters on 3D-printed carbon fiber-reinforced polymer composites under magnetic field control." *Journal of Manufacturing Processes*, 101, 1443-1452.
- Liu, J., Yu, M.-Y., Yu, Z.-Z., Nicolosi, V. (2023). "Design and advanced manufacturing of electromagnetic interference shielding materials". *Materials Today*, 66, 245-272.
- Masood, S. H. (2014). "Advances in Fused Deposition Modeling" in: Reference Module in Materials Science and Materials Engineering: Comprehensive Materials Processing. *Elsevier*. 10, 69-91.
- Mittal G., Dhand, V., Rhee, K. Y., Park, S.-J., Lee, W. R. (2015). "A review on carbon nanotubes and graphene as fillers in reinforced polymer nanocomposites." *Journal of Industrial and Engineering Chemistry*. 21, 11-25.
- Najmon, J.C., Raeisi, S., Tovar, A. (2019). "Review of additive manufacturing technologies and applications in the aerospace industry" in: Additive Manufacturing for the Aerospace Industry. *Elsevier*. 7-31.
- Peng, C., Tran, P., Mouritz, A.P. (2022). "Compression and buckling analysis of 3D printed carbon fibre-reinforced polymer cellular composite structures". *Composite Structures*, 300, 116167.
- Saeed, K., McIlhagger, A., Harkin-Jones, E., McGarrigle, C., Dixon, D., Shar, M.A., McMillan, A., Archer, E. (2022). "Characterization of continuous carbon fibre reinforced 3D printed polymer composites with varying fibre volume fractions". *Composite Structures*, 282, 115033.
- Shirvan, R.S., Nouri, A., Wen, C. (2021). "Structural polymer biomaterials" in: Structural Biomaterials: Properties, Characteristics and Selection. *Woodhead Publishing*. 395-439.
- Valino, D.V., Dizon, J.R.C, Espera Jr., A., H., Qiyi, C., Messman, J., Advincula, R. C. (2019). "Advances in 3D printing of thermoplastic polymer composites and nanocomposites". *Progress in Polymer Science*, 98, 101162.
- Wang, W., Smith, D.E. (2021). "Finite element modeling of fully-coupled flow/fiber-orientation effects in polymer composite deposition additive manufacturing". *Composites Part B*, 219, 108811.
- Yap, T., Heathman, N., Phillips, T., Beaman, J., Tehrani, M. (2023). "Additive manufacturing of polyaryletherketone (PAEK) polymers and their composites". *Composites Part B*, 266, 111019.



3D SURFACE PROFILOMETRY AND ITS APPLICATION IN TRIBOLOGICAL STUDIES

Assoc. Prof. Dr. Tuba ÖZDEMİR ÖGE¹

Asst. Prof. Dr. Mecit ÖGE²

Inst. Dr. Firdevs Banu ÖZDEMİR³

1 Bartın University, Bartın University, Faculty of Forestry, Department of Forestry Industry Engineering, Bartın, Turkey. E-mail: tozdemir@bartin.edu.tr, ORCID ID, 0000-0001-6690-7199.

2 Bartın University, Faculty of Engineering, Architecture and Design, Department of Mechanical Engineering, Bartın, Turkey; E-mail: mecitoge@bartin.edu.tr, ORCID ID, 0000-0001-5243-0828.

3 Kütahya Health Sciences University, Simav Vocational School of Health Sciences, Department of Medical Services and Techniques, Kütahya, Turkey; E-mail: firdevsbanu.ozdemir@ksbu.edu.tr, ORCID ID, 0000-0002-7935-2062.

1. Introduction

Tribological studies require in-depth knowledge from various disciplines such as mechanical engineering, materials science, chemistry, and physics. Tribological studies' main focus is friction, wear, and lubrication, and their relationship with each other. The primary objective of tribological studies is reducing friction and wear while enhancing the efficiency and endurance of mechanical systems. It has a wide range of applications including automotive, aerospace, and manufacturing industries and any other application that is affected by friction and wear induced losses.

Studies on wear has a vital role in material production and provide various advantages related to material choices, production techniques, end-product efficacy, and expenditures. Tribology and materials science often collaborate to engage in exploring the effects of wear-related issues to enable the development of more durable materials. Wear can be defined as material degradation or removal from surfaces due to mechanical interaction with other surfaces (Zum-gahr, 1988). Another description of wear is the material erosion from a surface due to contact with another material's surface (Kato, 1990). Coefficient of Friction (COF) is a measure of friction existing between two surfaces. It quantifies the resistance a surface against sliding or moving on another surface with relative motion. Aside from COF, the other measures to quantify wear performance are wear loss and specific wear rate. Wear loss can be quantified as weight loss or volume loss, which is the weight or volume difference between the start and end of the wear process. Specific wear rate is obtained by normalizing the worn volume with the sliding distance and the normal load, which is a way to eliminate the direct effect of load and sliding distance, to make a comparison between the wear performance of materials worn under diverse loading and sliding conditions. In tribological studies, pin-on-disc tests are conducted as per ASTM G99 standard either with reciprocating or rotating motion to evaluate wear performance under various conditions such as dry, lubricated, room temperature, high temperature, corrosive etc. conditions. The ASTM G99 standard is the commonly adopted procedure for evaluation of the abrasive wear resistance of materials. This method involves controlled rubbing of dry abrasive particles on the subject material's surface, which is followed by measuring the material loss using different methods (ASTM, 2000).

Numerous studies have been published on diverse type of wear on various materials. Oge et al. (2023) investigated the impact of boriding on the high temperature tribological performance of CoCrMo alloy. They reported that extended boriding periods resulted in enhanced wear resistance, as evident from reduced average COF values and specific wear rates. In another study on tribological evaluation of polymer nanocomposite mate-

rials, Karteri et al. (2023) investigated the effect of graphene nano-platelets (GNP) addition on the tribological properties of polypropylene (PP)-acrylonitrile butadiene styrene (ABS) blends (Karteri et al., 2023). As indicated by the literature works, tribological studies can be conducted on a wide range of material types.

The present work aims to provide brief information on how to compute COF and specific wear rate values as output data of sliding wear tests. The importance and application of 3D optical profilometry in recent tribological studies are also addressed.

2. Pin-on-disc wear tests and calculation of COF and specific wear rate data

2.1 Pin-on-disc wear tests

Pin-on-disc wear tests are conducted on test devices called tribometers designed specifically for this purpose in accordance with DIN50324-07, ISO 18535 and ASTM G99 test standards. In pin-on-disc tests, a material with a relatively higher hardness than the subject material is moved (with sliding motion) along a circular (on test rigs with rotating motion) or a linear (on test rigs with reciprocating motion) path, under a predefined normal load condition. The type of the sliding wear test and the corresponding testing device depends on the ambient testing condition such as room temperature, high temperature, dry sliding, lubricated, or corrosive environment. The counter material, also referred as the abrader is generally a small ball with 6 mm diameter made of a hard material such as Al_2O_3 (aluminum oxide), WC (wolfram carbide) to evaluate the wear performance of materials with high hardness or under high temperature. For metals, alloys, or coatings with lower hardness as well as polymer materials, grades of AISI 52100 high carbon chromium alloy steel are also used.

Two types of wear data can be derived from pin-on-disc tests. One is the coefficient of friction (COF) and the other is wear loss (weight or volume loss) calculated based on the measured wear profile. The contact geometry and information such as maximum contact pressure and the depth under which the maximum shear stress arises can be calculated theoretically in accordance with Hertzian Contact Theory, and these data can be also used for interpreting the wear data. A pin-on-disc wear test apparatus equipped with a high temperature chamber for high temperature wear tests is shown in Figure 1.



Figure 1. *Wear device with high temperature chamber*

Prior to almost all wear tests, an identical surface roughness with up to $R_a \approx 0.02 \mu\text{m}$ is ensured for all test specimens for standardizing the initial frictional force that arises upon first contact with asperity tips of the counter-materials during wear testing, thereby attaining more precise results. The testing setups qualified for testing under high temperature are equipped with components such as main shaft, ball holder, moment arm, sample table, sample holding apparatus, and screws made of high temperature resistant materials such as stainless-steel grades. The parameters for wear tests can be listed as the normal load, sliding distance, sliding speed and the ambient temperature for dry sliding tests. Sliding distance can be calculated by calculating the wear track circumference and multiplying it with the rotational speed of the main shaft (in rev/min) and testing time. Sliding speed can be calculated by dividing the sliding distance with the total testing time. For determining the rotational speed of the main shaft, a mobile laser speedometer can be used, or if no such device is at hand, the number of shaft rotations can be manually counted for a period of sixty seconds at lower rotational speeds, and once the current value for a specific rotational speed is determined, then the required rotational speed can be adjusted by increasing or reducing the calculated current value for the desired rotational speed. In some setups, once the specimen is fastened on the sample holder, the diameter of the wear track can be adjusted by linear motion of the motorized moment arm. A workflow diagram showing the data acquisition and utilization during wear tests is shown in Figure 2. Calculation of COF and specific wear rate is explained in the following sub-sections.

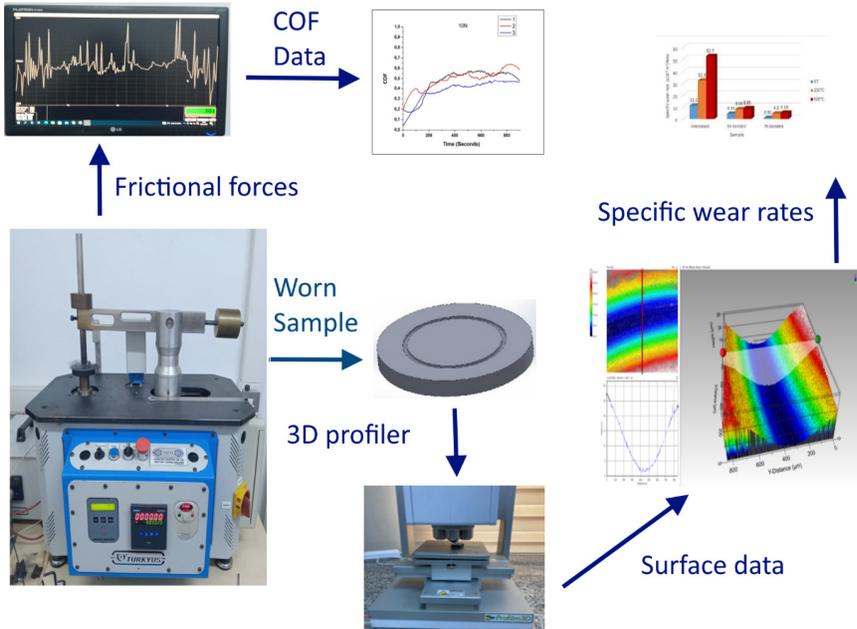


Figure 2. Workflow diagram showing the data acquisition and utilization during wear tests (Oge et al., 2023).

2.2 Calculation of COF

In both rotational and reciprocating tests, the sample is fastened and fixed firmly on a sample holder as shown in the Figure 1. If the motion is rotational, the pin is stationary, and the sample holder turns in accordance with a predefined rotational speed (in rev/min). If the motion is reciprocating, the pin is stationary, and the sample holder reciprocates in with a frequency which also depends on the spindle speed (rev/min). Tribological test rigs are equipped with a load cell which instantaneously records the frictional forces and displays it on the test rig’s software interface. The frequency of the stored data (1 datum per second, two data per second, etc). can be defined during setup. Aside from the displayed data, all tribological data (frictional force in grams) is recorded in a log file which is initiated with the start of the test and terminated with the end of the test. The COF values can be calculated using the following Equation 1 (Gupta et al., 2008):

$$F_s = F_N \times \mu \tag{1}$$

where, F_s is the frictional force, F_N is the normal load applied during the test, and μ is the coefficient of friction.

If F_s is recorded in grams and the applied normal load is defined in

Newtons, the required unit conversion is made between force values and a COF vs. time graph is obtained for the respective wear test. These graphs can be used to evaluate and make comparison between the wear performance of diverse samples. A COF vs time graph is shown in Figure 3.

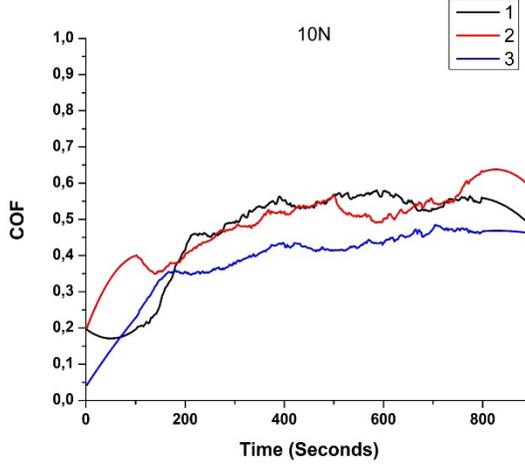


Figure 3. A COF vs time graph showing COF value of 3 samples worn under 10N load for a period of 900 seconds.

1.3. Calculation of Specific Wear Rate

To obtain the specific wear rate data, the first step is to obtain the surface morphology of the wear track by using any kind of profilometer. 3D optical profilometers obtain a 3D model of the surface by taking images between predefined upper and lower height limits. Upon taking these images, the software merges the images taken from each height from the surface and thus gives a 3D model of the surface. This way the surface profile or morphology can be obtained without physical contact with the sample. In the case of wear tests, the subject morphology is the wear track which has a semi-circular like wear profile. When the wear profile is obtained through the software interface, the cross-sectional area of the wear profile can be computed by the software. Upon obtaining sufficient data, it can be averaged and multiplied by the wear track diameter to obtain the worn volume. Worn volume can be then normalized by the sliding distance and the normal load in accordance with the below equations (Kucuk et al., 2022), to eliminate the direct effect on these parameters and make a more precise comparison between the wear loss data of the worn samples.

$$V = \pi \times D_w \times A_C \quad (2)$$

$$W_s = \frac{V}{F \times S} \quad (3)$$

In Equation 2, V denotes the theoretical volumetric loss in mm^3 , D_w denotes the diameter of the worn in mm, and A_c denotes the average of the cross-sectional areas of the wear track obtained through measurement with the optical 3D profiler. In Equation 3, W_s denotes the specific wear rate, F denotes the normal load applied during the test, and S denotes the total sliding speed which can be calculated by multiplying the sliding speed with the total test time.

2. 3D Optical Profilometry

An optical profilometer is an electro-mechanical device used for the examination and measurement of material surface morphologies, three-dimensional height disparities, and surface topographies. Optical profilometers operate based on optical principles such as light scattering, reflection, and focusing. To provide the user with surface details, the device takes 2 dimensional snapshots of the surface at various heights from the surface between predefined upper and lower limits. Afterwards, these two-dimensional images are merged to obtain a three-dimensional model of the surface topography. 3D profilers' applications involve determination of surface characteristics such as height disparities, roughness, transverse, and longitudinal sections on material surfaces, surface defects, and surface roughness. In industrial use, the process quality of manufactured products can be monitored accordingly, and in academic use topographies of tested samples can be obtained after various characterization tests such as wear tests.

Wear can be identified as material loss or alterations in material quantity on the surface. Optical profilometers are used to quantify wear losses and assess the topographic alterations on the wear surface. It is a powerful tool that provides in-depth information about worn surfaces, providing valuable data for tribological studies related to the durability of materials. A 3D optical profiler and its software interface is shown in Figure 4.

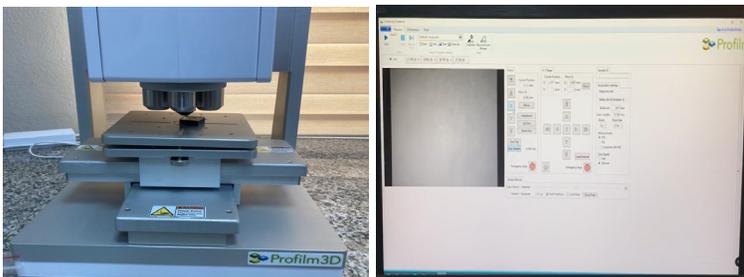


Figure 4. A 3D optical profiler and its software interface

Key considerations during the utilization of an optical profilometer are:

- Prior to the measurements and during the setup step, accurate placement and meticulous calibration are prerequisites for acquisition of precise data.
- It is also required to eliminate any contaminant such as dirt, oil, or particles as these could impact the measurement accuracy.
- The device collects data by scanning the material surface, capturing details such as surface asperities, wear tracks, and other relevant surface features.
- In the analysis phase, the obtained data can be analyzed by various analysis tools specific to the brand and the model of the device. Worn surface features such as wear loss, surface roughness, and wear track depths on wear profiles can be obtained.
- Data obtained by 3D profiler measurements serve multiple purposes such as understanding wear mechanisms and overseeing wear processes. In industrial use, the obtained wear data can contribute to attempts to enhance product quality and detect undesired surface conditions such as wear losses and topographical alterations.
- Surface roughness is a measure of microstructural surface undulations, and irregularities. It quantifies deviations from a median value by evaluating data obtained during scanning. Roughness stands as a critical factor in quality control concerning surface engineering or production processes.

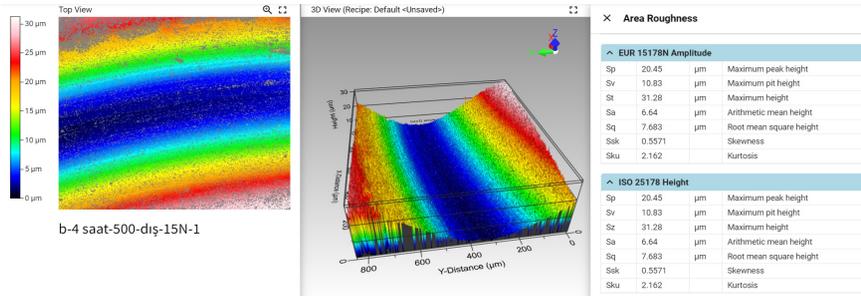


Figure 5. Area roughness measurement on a profilometer

The area roughness measurement interface of a 3D profiler is shown in Figure 5. For area roughness measurements, the subject area to be evaluated is determined on the 2D image and the corresponding roughness values are collectively shown in a column.

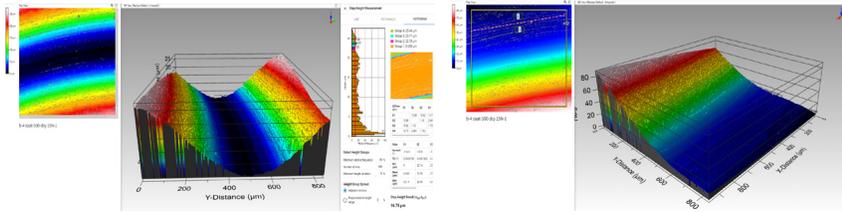


Figure 8. *Step-height measurement*

The propriety software of 3D optical profilers also involves various image processing tools to process and modify surface images for ease of utilization.

3. Conclusion

As an important subject for academic and industrial studies, wear causes various alterations in surface morphologies of products and materials. Profilometry plays a crucial role in monitoring and analyzing such surface alterations in various domains of academic and industrial fields. This study aims to provide brief information on sliding wear tests, the test setups employed in sliding wear tests, acquisition, and calculation of test outputs, as well as the role of 3D optical profilometry on the acquisition and the use of wear data. Tools and features of optical 3D profilers such as line, area roughness acquisition and height and distance measurement are also briefly explained. The current work is believed to provide useful information for academic and industrial users interested in quantification and investigation of tribological phenomena.

References

- Gupta, B.S., Ajayi, J.O., Kutsenko, M. (2008). “Experimental methods for analyzing friction in textiles” in Friction in Textile Materials. *Woodhead Publishing*. pp-174-221.
- Karteri, İ., Öge, M., Küçük, Y., Öge, T.Ö., Özdemir, F.B., Karataşlı, M., Çulha, M. A., Babacan, T. (2023) Investigation of tribological properties of polypropylene (PP)—Acrylonitrile butadiene styrene (ABS) blends reinforced with graphene nano-platelets (GNPs)., *Tribology International* 183 (2023) 108419.
- Kato, K. (1990), “Tribology of ceramics”, *Wear*, 136 (1): 117–133.
- Küçük, Y., Döleker, K.M., Gök, M.S., Dal, S., Altınay, Y., Erdoğan, A. (2022). Microstructure, hardness and high temperature wear characteristics of boronized Monel 400, *Surface and Coatings Technology*, 436, 128277.
- Öge, M., Küçük, Y., Öge, T.Ö., Günen, A., Kanca, Y., Gök, M.S. (2023) Effect of boriding on high temperature tribological behavior of CoCrMo alloy., *Tribology International* 187 (2023) 108697.
- Standard Test Method for Wear Testing with a Pin-on-Disk Apparatus, ASTM 2000, https://tribotest.ru/images/1_STM-G99.pdf, Accessed: 16.12.2023
- Zum-Gahr, K. H. (1988). “Microstructure and Wear of Materials”, *Journal of the Society of Materials Science*, 37(412): 1-16.



**ENHANCING CUSTOMER
SATISFACTION AND COST EFFICIENCY:
A VALUE ENGINEERING APPROACH
TO IMPROVING THE CHAIR
MANUFACTURING PROCESS**

Lect. Seymen iftci¹

Assoc. Prof. Dr. Abdullah Cemil Ilce²

Prof. Dr. Kadir zkaya³

1 Duzce University, Duzce Vocational School, Department of Design,
Duzce. ORCID:0000-0002-9802-7812

2 Abant İzzet Baysal University, Faculty of Engineering, Department of In-
dustrial Engineering, Bolu, ORCID: 0000-0001-5133-683X

3 Pamukkale University, Denizli Vocational School of Technical Sciences,
Department of Design, Interior Design Program, Denizli, ORCID: 0000-0002-
6740-0178

1. Introduction

Idea generation, product design and engineering can be combined as a path towards new product development, which is a preliminary step in development of a product or service (Julian et al., 2012). These steps may not always be successful for the transformation into a new product (Maguire, 2001). An unsuccessful design both affects the views of the user towards the manufacturing company and also paves the way for the company to be forced to endure subsequent additional costs for these products. Consequently, carrying out the product design process in accordance with the user expectations is an important subject (Akay and Kurt, 2008). Also, there is no different situation in the designs of furniture. Initially, it is difficult to predict the consumer's expectations. It is important from this aspect to listen the voice of customer during the design process. Carrying out this process in accordance with the user expectations, while it will satisfy the consumer, bring respect and profits to the company; it will also increase the competitive strength of the company. With these thoughts, companies, which want to provide for superiority over their competitors, use various management and cost systems. One of these systems is known with the name of value analysis (value engineering-VE) and is a design analysis tool whose foundations were set forth by Lawrence D. Miles (Miles, 1972).

VE is a professionally applied, function-oriented, systematic team approach used to analyze and improve value in a product, facility design, system or service -a powerful methodology for solving problems and/or reducing costs, while improving performance/quality requirements (Starbek et al., 2010).

Some researchers identify VE as a cost reduction tool (Dlugatch, 1973; Heggade, 2002; Kılıçoğulları and Akman, 2005; Duran, 2007; Tohidi, 2011), while others echo the cost effectiveness without neglecting performance (Dlugatch, 1973; Benstin et al., 2011). In fact, VE is not just a cost reducing but a decision-making, consensus-based problem solving and value improvement (Wao, 2014).

It was stated in the literature that VE was used in studies for different sectors and they benefited from value analyses: Kaplanoğlu (2012), in the electronics sector, Albayrak, (2012) in the field of education, Deniz (2012) in an erosion control project, Shu et al. (2010) in district cooling and heating systems, Wao (2014), Ranjbaran (2013), Tohidi (2011), Dönmezler (2003), Şenel (2003), Austin and Thomson (1999) in the construction sector, Tang and Bittner (2014) in marine construction projects.

When the studies made are examined, it has been determined that this method can be used as a technique for lowering costs on present products and this has been given as examples in many fields, but not many studies have been made and detailed in the furniture sector. This study was planned to determine the applicability of the value analysis method in the

furniture sector. It was aimed to develop the value of a dining chair model, which lowered the sales figures of a furniture company.

1.1. Material

The sample of a dining chair manufactured by the Sancaklı Furniture Corporation in Duzce. The legs-frame of chair mentioned in this study had a laminated veneer structure, and the seating part was covered with fabric material. The dimension of the chair was 95 cm in height, 52.5 cm in width and 45 cm in depth (Figure 1).



Figure 1. General appearance of the chair.

2. Methods

This section presents the methods used throughout the study.

2.1. Value analysis

Value methodology creates a structured procedure called a Job plan for improving value. Problems were recognized and tackled based on their functions in the job plan (Miles, 1972). It was organized in a five-step process: Information phase, analysis phase, creative phase, judgment phase, development phase. Brainstorming, nominal group technique, cause-and-effect analysis pareto charts etc. could be used at various stages of this technique (Ranjbaran, 2013).

The above stages were used in this study. In the information phase, dissatisfaction was measured through customer questionnaires about the chair whose sales were decreasing. The analysis phase started by evaluating the basic functions of the product or process from the user's point of view. In addition, the relationship between the product's functions and technical parameters and structural features is analyzed. The physical quantities that contribute to the performance of each function are determined and, if necessary, sub-functions are defined. Furthermore, the cost elements of the product are determined to increase cost-effectiveness, and the required resources and costs are optimized. Design changes are made to achieve a balance between cost and performance (Creative phase).

Finally, potential improvements to the product or process and its performance are tested on a prototype to determine the results of the improvement, and a decision is made about the product (judgement phase). (Ranjbaran, 2013, Kaplanoğlu 2012, Albayrak, 2012, Deniz 2012, Shu et al. 2010, Ranjbaran 2013, Tohidi 2011, Dönmezler 2003, Şenel 2003).

2.2. Linear regression

The single variable analysis of regression was an analysis technique that examined the relationship between a dependent variable and an independent variable. That a correct equation was formulated according to the analysis based on the least squares method, represented the linear relationship between the dependent and independent variables. Just as in analysis of correlation, the relationship dwelled upon in the analysis of regression was the linear relationship whereas the calculation of correction was conducted with the assistance of the least squares method. The mathematical expression of linear relationship between the dependent (y) and independent (x) variable is as follows (Hocking, 2005).

$y_i = \beta_0 + \beta_1 x_i + \varepsilon_i$	(1)
---	-----

Where the abbreviations of β_0 and β_1 are unknown parameters of model. ε_i shows the error term when the parameters of y_i and x_i are dependent and independent variables, respectively.

2.3. Estimation of Parameters

The parameters for the regression model were estimated with respect to the least squares method, where the β_0 and β_1 parameters in the regression equation should be estimated so that the sum of error squares was the smallest. In this case, we can calculate the dependent values of y from the following equations based on the values of x (Chatterjee and Hadi, 2012).

$y_i = \beta_0 + \beta_1 x_i$	(2)
$\beta_1 = \frac{n(\sum_{i=1}^n x_i y_i) - (\sum_{i=1}^n x_i)(\sum_{i=1}^n y_i)}{n(\sum_{i=1}^n x_i^2) - (\sum_{i=1}^n x_i)^2}$	(3)
$\beta_0 = \frac{\sum_{i=1}^n y_i - b \sum_{i=1}^n x_i}{n}$	(4)

Where,

$$i = 1, 2, 3, \dots, n$$

y = Response or dependent variable

x = Auxiliary or independent variable

β_1 = The slope of the best fit plot (parameter)

β_0 = y -intercept (parameter)

2.4. finite element analysis

The finite element analysis method was a method used frequently in the analysis of engineering problems whose solutions were difficult. The Solid187 element was used from the element types included within the structure of the ANSYS® 14 in the modeling of the chair.

The geometric measurements of the models in the program, the modulus of elasticity, the Poisson's ratio values and the values of the forces that would be applied were entered for being able to solve problems with the finite element method. Loadings (Figure 2) were made according to the EN 1728 standards.

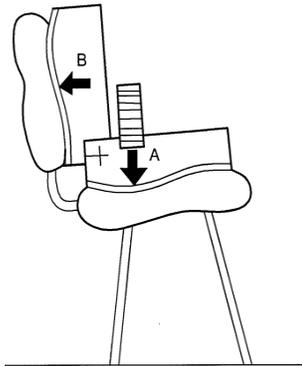


Figure 2. View of chair loading.

3. Applying the proposed model numerically

At this stage, applications were made in the manner specified for the method proposed for a sample dining chair model that was determined. First, the team that would make the value analysis was determined. The team was composed of five persons, including the company owner, chiefs of marketing, production and design and an academician from the Düzce University.

Next, the order of importance of the qualifications was determined by using the priority matrix (Table 1). The relationships of the qualifications to each other were cross-examined in the filling of the matrix. Making a joint decision through brainstorming by the team filled this matrix. The cri-

teria weights were determined by giving 1 to those who thought there was a relationship and 0 to those who thought there was no relationship in the dual comparisons. Qualifications were considered to have a relationship with them, and they were shown as +1 in the matrix.

Table 1. Chair priority value matrix.

	G	M S	A	U C	S	Total	Importance Rate (%)	Ordering
GQ		1	1	1	1	4+1	33	1
MSQ	1		0	1	1	3+1	27	2
AQ	1	0		0	1	2+1	20	3
UBCQ	0	1	0		0	1+1	13	4
BS	0	0	0	0		0+1	7	5

3.1. Calculate dining chair satisfaction

1. **Guarantee Qualification (G):** It was mandatory for dining chairs to have a two-year guarantee as a requirement of the laws. Whereas, a company was not encountered in the market, which gives a guarantee of over five years. It was accepted that when a two-year guarantee was given to a chair, the level of customer satisfaction would be at a medium degree (5) and when a five-year guarantee was given to a chair, the level of customer satisfaction would be at the highest level (10). Accordingly, the formula for the guaranteed qualification was calculated as given below (x: the period of guarantee given to chairs on the basis of years).

Firstly, data points were identified.

i	x (year guarantee)	y (satisfaction value)
1	2	5
2	5	10

Secondly, the essential calculations were made.

$$\sum_{i=1}^2 x_i = 2 + 5 = 7$$

$$\sum_{i=1}^2 y_i = 5 + 10 = 15$$

$$\sum_{i=1}^2 x_i y_i = (2 \otimes 5) + (5 \otimes 10) = 60$$

$$\sum_{i=1}^2 x_i^2 = 4 + 25 = 29$$

$$\left(\sum_{i=1}^2 x_i\right) \left(\sum_{i=1}^2 y_i\right) = 7 \otimes 15 = 105$$

Thirdly, the slope of the best fit plot (b) and y-intercept (a) were calculated (Eg. 3 - 4).

$$b = \frac{n(\sum_{i=1}^n x_i y_i) - (\sum_{i=1}^n x_i)(\sum_{i=1}^n y_i)}{n(\sum_{i=1}^n x_i^2) - (\sum_{i=1}^n x_i)^2} = \frac{(2 \otimes 60) - (7 \otimes 15)}{(2 \otimes 29) - 49}$$

$$b \cong 1.67$$

$$a = \frac{\sum_{i=1}^n y_i - b \sum_{i=1}^n x_i}{n} = \frac{15 - (1.67 \otimes 7)}{2}$$

$$a \cong 1.65$$

Finally, the slope and y-intercept was used to form the equation of the line of best fit.

$y_i = \beta_0 + \beta_1 x_i = 1.65 + 1.67 x_i$	(5)
---	-----

All other calculations belonging to the current work were done in a similar way. However, we do not need to give all the computations performed in the paper to avoid excess numbers of pages.

2. Measurement Suitability Qualification (MS): It was accepted that a manufacturing defect (unplanned defect) of 0 cm to 0.2 cm could be overlooked for the pieces and entire chair. It was accepted that when a 0.2 cm manufacturing defect of the chair was determined that the level of customer satisfaction would be at a medium degree (5) and when a 0.0 cm manufacturing defect of the chair was determined that the level of customer satisfaction would be at the highest level (10). Accordingly, the formula for the measurement suitability qualification was calculated as given below (x: dimensional deviation that could be observed in the chair on the basis of cm).

$y_i = 10 - 25 x_i$	(6)
---------------------	-----

3. Assembly Qualification (A): The fact that the chair could be separated into pieces or be dismantled and attached provides benefits for transport. Customers were able to bring the chairs to dimensions that are easier when moving goods or that could be stored when they were not used temporarily. However, the greatest benefit of chairs being separable was for wholesale customers. If a chair was made in one piece, then 320 each would be transported in a 40m³ container and if a chair is separable, then 1,200 each can be transported in a 40m³ container. It was accepted that if 320 each chairs were transported in a 40m³, then the level of customer satisfaction would be at a medium degree (5), and if 1,200 each chairs were transported, then it would be at the highest level (10). Accordingly, the linear equation for the assembly qualification was calculated as given below (x: the number of chairs that could be transported in a 40m³ container).

$y_i = 3.16 + 0.0056x_i$	(7)
--------------------------	-----

4. Upholstery Comfortable Qualification (UC): The used of foam between 1 cm and 4 cm, which was used on the seating font, was an important component for seating comfort. It was accepted that if the 1 cm foam were used in the chair that the level of customer satisfaction would be at a medium degree (5) and that if the 4 cm foam were used in the chair that it would be at the highest level (10). Accordingly, the linear equation for the upholstery being comfortable was calculated as given below:

$y_i = 3.33 + 1.67x_i$	(8)
------------------------	-----

5. Sturdy Qualification (S): The finite element analysis strengthened with the safety factor value was used to calculate for the satisfaction level of being sturdy qualification. Throughout the computations, the maximum safety factor was used as a value of 15. Additionally, it is to be strongly mentioned here that the values of safety factor smaller than 1 represents the unsafe regions before the completion of their lifespan (Chaush, 2008).

The safety factor value was calculated for both the back leg and back frames of the chair. The small parameter (among two parameters computed) was preferred for the satisfaction in the calculations performed due to the correspondence to much more unsafe situation of small value as compared to the high one. Moreover, that the first deformation at the endurance tests made in the chairs begins at the back legs of a chair makes us compute for only the back legs. It was accepted that if the safety factor in the chair was raised to one, then the level of satisfaction would be at a medium degree (5) and if it were raised to 15, then the level of satisfaction would be at the highest level (10). Accordingly, the linear equation for being able to measure the back leg side frame sturdiness value has been calculated as given below:

$y_i = 4.64 + 0.357x_i$	(9)
-------------------------	-----

3.6. Determination of the levels of satisfaction for the chair qualifications

The equations explained in the Methods section were utilized in the determination of the level of satisfaction of the qualifications. A three-year guarantee was given for the sample chairs. Accordingly, by utilizing Eq. 5, the level of satisfaction was 6.66 for the guaranteed qualification.

$$y_i = 1.65 + 1.67x_i = 1.65 + (1.67 \otimes 3) = 6.66$$

An 0.2 cm manufacturing defect was determined in the sample chair model. Accordingly, by utilizing Eq. 6, the level of satisfaction was calculated to be 5.

$$y_i = 10 - 25x_i = 10 - (25 \otimes 0.2) = 5.00$$

Providing that the sample chair model was assembled, 320 chairs were moved in a container. Accordingly, by utilizing Eq. 7, the level of satisfaction was calculated to be 5.

$$y_i = 3.16 + 0.0056x_i = 3.16 + (0.0056 \otimes 320) = 5.00$$

In the sample chair model, 32 DNS foam with a thickness of 1 cm was used. Accordingly, by utilizing Eq. 8, the level of satisfaction was calculated to be 5.

$$y_i = 3.33 + 1.67x_i = 3.33 + (1.67 \otimes 1) = 5.00$$

The safety coefficient value was utilized in the finite element analysis program for being able to calculate the sturdiness level of satisfaction for the sample chair. In the loadings made according to the EN 1728 standards (Figures 2), it was determined that the safety coefficient for the back leg side frame was 1,296 and for the back leaning frame was 4,142. For the small one of these values, the level of satisfaction obtained was calculated to be 5.10 by utilizing Eq. 9.

$$y_i = 4.64 + 0.357x_i = 4.64 + (0.357 \otimes 1.296) = 5.10$$

3.7. Determination of the benefit function level qualifications of chairs

The priority function of the dining chairs and the secondary functions, which supported this function, were determined for calculating the benefit functions of the chair qualifications. These functions determined have been given below.

The primary functions of the dining chairs: 1. Realization of seating with the objective of eating.

Secondary functions: 1.1 Enough back support (EBS), 1.2 Ergonomic (E), 1.3 Aesthetic (A), 1.4 Safety (S), 1.5 Lightweight (L), 1.6 Easy-clean (EC), 1.7 Multi-used (MU).

The qualification function matrix was constituted by evaluating according to the qualifications of the functions determined and the benefit was calculated by multiplying the importance and satisfaction levels (Table 2).

According to Table 2, the highest function benefit was determined in

its safety function. This was followed by the functions of its ergonomic, it's enough back support, its aesthetic, its lightweight, its multi-used and its easy-clean, respectively.

Table 2. Qualification function matrix for the sample chair.

Qualifications	I/S/B	Functions 1							Total
		1.1 EBS	1.2 E	1.3 A	1.4 S	1.5 L	1.6 EC	1.7 MU	
Guarantee	Importance	10	10	0	10	0	3	0	33
	Satisfaction Level	2	2	0	2	0	1	0	7
	Benefit	20	20	0	20	0	3	0	63
Measurement Suitability	Importance	5	9	6	7	0	0	0	27
	Satisfaction Level	1	1	2	1	0	0	0	5
	Benefit	5	9	12	7	0	0	0	33
Assembly	Importance	4	0	0	6	5	0	5	20
	Satisfaction Level	1	0	0	2	1	0	1	5
	Benefit	4	0	0	12	5	0	5	26
Upholstery Comfortable	Importance	0	7	5	0	0	1	0	13
	Satisfaction Level	0	1	3	0	0	1	0	5
	Benefit	0	7	15	0	0	1	0	23
Sturdy	Importance	2	2	0	3	0	0	0	7
	Satisfaction Level	1	1	0	3	0	0	0	5
	Benefit	2	2	0	9	0	0	0	13
Function Benefit		31	38	27	48	5	4	5	

3.8. Determination of the chair costs

Table 3 shows the total amount excluding VAT by calculating the unit cost of the sample chair.

Table 3. Detailed cost account of the sample chair model.

Name of the Part / Material / Size	Material Expense	Material Cost for One Piece	Material Cost (€)	Production Cost (€)	Total (€)
Back Leg (2 pieces) / Fagus LVL / 910*40*25 mm	0,00180 m ³	862,07 €/m ³	1,55	1,55	3,10
Front Leg (2 pieces) / Fagus LVL / 455*40*25 mm	0,00092 m ³	862,07 €/m ³	0,79	0,59	1,38
Side Beam (2 pieces) / Fagus LVL / 375*50*25 mm	0,00116 m ³	862,07€/m ³	1,00	0,90	1,90

FrontBeam (1 piece) / Fagus LVL / 365*60*25 mm	0,00046 m ³	672,41€/m ³	0,31	0,34	0,65
Back Beam (1 piece) / FagusEdging Strip / 310*60*25 mm	0,00050 m ³	672,41€/m ³	0,34	0,28	0,62
Backward Leaning Beam (4 pieces) / Fagus LVL / 310*35*20 mm	0,00088 m ³	862,07 €/m ³	0,76	0,93	1,69
Backward Leaning Top Beam(1 piece) / Fagus LVL / 425*70*25 mm	0,00075 m ³	862,07 €/m ³	0,65	0,34	0,99
Seating Part (1 piece) / Fagus LVL / 460*410*9 mm	0,00275 m ³	431,03 €/m ³	1,19	1,24	2,43
Loaf (4 pieces)	4 pieces	0,10 €/piece	0,40	0,06	0,46
Fabric (1 piece) / 460*410*9 mm	0,17000 m Tulle	2,76 €/m Tulle	0,47	0,53	1,00
Sponge 32 DNS / 460*410*9 mm	0,00310	102,41 €/m ³	0,32	0,17	0,49
Buckram 70g/m ² / 460*410*9 mm	1 m Tulle	0,03 €/m Tulle	0,03	0,34	0,37
Bolt Imbus M6*40 (1 adet)	4 pieces	0,02 €/piece	0,07	0,00	0,07
Pulspring lock washer/ 6,5*11*1,5 mm	4 pieces	0,01 €/piece	0,03	0,00	0,03
Varnish / 150 gr for m ² and 3 times	0,77000 m ²	5,17 €/m ²	3,98	1,79	5,77
Box / 2 chairs are put in 1 box	1 pieces	0,22 €/piece	0,11	0,17	0,28
(1€= 2,9 TL) TOTAL					21,23

3.9. Constituting the cost/benefit graph for the chair

The cost-benefit values for the functions were presented in Table 4. Accordingly, a cost-benefit graph was constructed for the functions (Fig. 3).

Table 4. Cost/benefit table for the sample chair.

The Parts of Dining Chair	Function Costs (€)							Total Cost (€)
	1.1 EBS	1.2 E	1.3 A	1.4 S	1.5 L	1.6 EC	1.7 MU	
Back Leg	1,03	0,69	0,35	0,35	0,34	0,34	0,00	3,10
Front Leg	0,00	0,69	0,35	0,17	0,17	0,00	0,00	1,38
Side Beam	0,17	0,35	0,35	0,68	0,35	0,00	0,00	1,90
Front Beam	0,00	0,34	0,00	0,17	0,14	0,00	0,00	0,65
Back Beam	0,00	0,28	0,00	0,17	0,17	0,00	0,00	0,62
Backward Leaning Beam	0,69	0,35	0,00	0,48	0,00	0,00	0,17	1,69
Backward Leaning Top Beam	0,44	0,21	0,00	0,34	0,00	0,00	0,00	0,99
Seating Part	0,00	0,76	0,76	0,69	0,17	0,00	0,05	2,43
Loaf T	0,46	0,00	0,00	0,00	0,00	0,00	0,00	0,46
Fabric A	0,00	0,00	0,50	0,00	0,00	0,50	0,00	1,00
Sponge 32 DNS	0,00	0,28	0,00	0,00	0,00	0,21	0,00	0,49
Buckram 70g/m ²	0,00	0,00	0,37	0,00	0,00	0,00	0,00	0,37
Bolt Imbus M6*40	0,07	0,00	0,00	0,00	0,00	0,00	0,00	0,07
Pulspring lock washer	0,03	0,00	0,00	0,00	0,00	0,00	0,00	0,03
Top Surface Process	0,00	0,00	3,44	0,00	0,00	2,07	0,26	5,77
Box	0,00	0,00	0,00	0,17	0,11	0,00	0,00	0,28
Total Cost								21,23
Function Cost	2,89	3,95	6,12	3,22	1,45	3,12	0,48	
Function Benefit	31	38	27	48	5	4	5	
Value=Benefit/Cost	10,73	9,62	4,41	14,91	3,45	1,28	10,42	

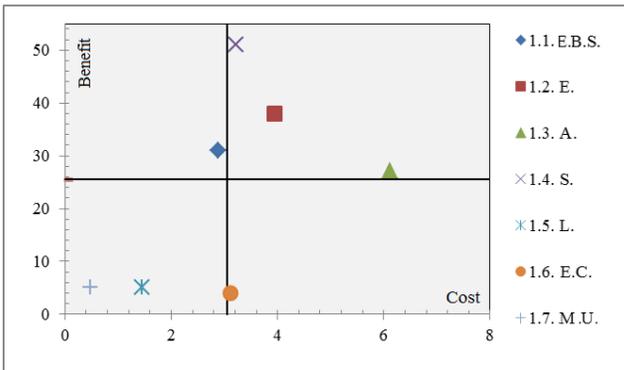


Figure 3. Cost - benefit graph for the sample chair.

According to Figure 3, the most beneficial functions were safety, ergonomic and aesthetic. However, of these functions, the costs were also very high for its aesthetic. The function of its safety and its ergonomic had a medium degree cost. The function of enough back support was a function with a medium degree for cost and benefit. The benefit was very low for easy-clean, and its cost was a high function at a medium degree. The costs and benefits for the functions of its lightweight and multi used were low functions.

In the value analysis studies made on chairs, Aktan et al. (1997) stated that the five factors that set forth the value of a product are functionality, reliability, sturdiness, safety and aesthetic. Whereas Kılıçoğulları and Akman (2005), stated that the sturdy connection and safety functions are important. These results, by treating the seven functions, show a similarity to the results in this study.

At the conclusion of the studies by Aktan et al. and Kılıçoğulları and Akman (2005), by making a new design, they compared the cost of this with the first situation costs. Accordingly, savings were provided for costs in both studies. However, the levels of customer satisfaction were not calculated. They did not mention the subject of how the cost gains changed the level of customer satisfaction. Whereas, in this study, the level of customer satisfaction became accountable with mathematical methods.

4. Conclusion

The most important objective of value analysis is to lower the costs and/or to realize the functions in a more successful manner and to increase the product value by these means.

The function analysis of sample dining chair is performed in this work. The seating feature should be the primary function whereas the properties of back support, ergonomic, aesthetic, safety, lightweight, easy-clean and multi-used features point out the supplementary functions for the dining chair.

According to the results deduced from the analyses of dining chair, the function values of sample dining chair were a total value of 54.82 units with 10.73, 9.62, 4.41, 14.91, 3.45, 1.28, 10.42 for the enough back support, ergonomic, aesthetic, safety, lightweight, easy-clean and multi-used features, respectively. The cost price to the company of the sample chair was 21.23€.

A new design can be made with the data obtained in this study by passing through the idea development steps. Accordingly, increasing the period of guarantee given for the dining chair, if dimensional errors are not

made in manufacture, if the chair is produced disassembled, if the thickness of foam is increased, and if the leg-frame joining's are made sturdier, then the customer satisfaction will be at a maximum level. However, these factors can have a positive or negative effect on the cost. Consequently, it is necessary to set forth more than one design by making the changes in steps that would be made in the factors. In this manner, it can be cross-examined which design will be more productive from the aspect of cost and level of satisfaction and the most suitable design can be selected.

Acknowledgments

This study is a part of a master's thesis written by Seymen Çiftçi at the Düzce University, Institute of Science and Technology, Düzce, Turkey. ANSYS® 14 package program used in Department of Forest Industrial Engineering at Süleyman Demirel University.

References

- Akay, D., Kurt, M.A. 2008. Literature review on user centered design and product usability. *Journal of the Faculty of Engineering and Architecture of Gazi University*; 23(2):295–304.
- Aktan, F.C., Türkay, A., Burdurlu, E. 1997. Mobilya endüstrisinde değer analizi ve bir uygulama (Value analysis in furniture industry and an implementation). I. Ulusal Mobilya Kongresi, Ankara, Turkey, (in Turkish).
- Albayrak, G. 2012. Türkiye’de inşaat mühendisliği eğitiminin değer mühendisliği kavramları açısından istatistiksel olarak incelenmesi (Civil engineering education in Turkey in terms of statistical concepts of value engineering study). Master’s thesis, Eskişehir Osmangazi Üniversitesi, Fen Bilimleri Enstitüsü, Eskişehir, Turkey, (in Turkish).
- Austin, S.A., Thomson, DS. 1999. Integral value engineering in design. *Proceedings of COBRA 99 Conference, RICS, Salford, September.*
- Benstin, MS, Benston, DP., Haraburda, SS. 2011. Using value engineering to reduce life cycle cost. *Defense AT&L*; 31–4.
- Chatterjee, S., Hadi, A.S. 2012. *Regression Analysis by Example. Fifth Edition, John Wiley Inc. Publication.*
- Chaus, Y.I. 2008. Finite element analysis “The fatigue analysis with workbench.” Dokuz Eylül University, Department of Mechanical Engineering Lecture Notes.
- Deniz, T. 2012. Erozyon kontrolü çalışmalarında değer analizi (Value analysis in erosion control activities). PhD Dissertation, İstanbul Üniversitesi, Fen Bilimleri Enstitüsü, Orman Ekonomisi Programı, İstanbul, Turkey, (in Turkish).
- Dlugatch, I. 1973. Methodology for value engineering. *Journal of IEEE Transactions on Reliability*; R-22(1):20–3.
- Dönmezler, S. 2003. Önyapım sistem seçiminde, değer mühendisliği uygulaması (Application of value engineering in the selection of pre-construction systems). Master’s thesis, Mimar Sinan Güzel Sanatlar Üniversitesi, Mimarlık Anabilim Dalı, Yapı Bilgisi Programı, İstanbul, Turkey, (in Turkish).
- Duran, C. 2007. Değer analizinin uygulama süreci (The implementing process of value analysis or engineering). *Kamu-İş*; 9(3):81–96 (in Turkish).
- Heggade, V.N. 2002. IT propelled value engineering in construction. *The Indian Concrete Journal*; 222–6.
- Hocking, R.R. 2005. *Methods and Applications of Linear Models: Regression and the Analysis of Variance, Wiley Series in Probability and Statistics.*
- Julian, F., Méndez, J.A, Espinach, F.X, Verdaguer, N., Mutje, P., Vilaseca, F. 2012. Bio-based composites from stone groundwood applied to new product development. *BioRes*; 7(4):5829–42.

- Kaplanoğlu, E. 2012. Değer mühendisliği, hedef maliyetleme ve kaizen karmasının elektronik sektöründe uygulaması (Value engineering, target costing and kaizen mixed application in electronic sector). PhD Dissertation, Ege Üniversitesi, Sosyal Bilimler Enstitüsü, İzmir, Turkey (in Turkish).
- Kılıçoğulları, P. and Akman, G. 2005. Değer analizinin ürün tasarımındaki rolü: Bir uygulama (The role of value analysis in product design: a case study). V Ulusal Üretim Araştırmaları Sempozyumu, İstanbul Ticaret Üniversitesi, 25-27 Kasım 2005, İstanbul, Turkey, (in Turkish).
- Maguire, M. 2001. Methods to support human-centred design. *International Journal of Human- Computer Studies*; 55:587–634.
- Miles, L.D. 1972. *Techniques of value analysis and engineering*. 2nd ed. New York: McGraw Hill,
- Ranjbaran, Y. 2013. Integrated computational model in support of value engineering. Master's thesis, Applied Science (Building Engineering), Concordia University, Department of Building, Civil and Environmental Engineering, Montreal, Quebec, Canada.
- Şenel, G. 2003. İnşaat projelerinde maliyet azaltmak için sistematik yaklaşımlar “değer mühendisliği” (Systematical approaches for cost minimizing in construction project value engineering). Master's thesis, Mimar Sinan Güzel Sanatlar Üniversitesi, Yapı Mühendisliği Anabilim Dalı, Yapım Proje Yönetimi Programı, İstanbul, Turkey (in Turkish).
- Shu, H, Duanmu, L, Zhang, C, Zhu, Y. 2010. Study on the decision-making of district cooling and heating systems by means of value engineering. *Renewable Energy*; [35\(9\)](#):1929–39
- Starbek, M., Grum, J., Brezovar, A., Kusar, J. 2010. *Techniques and Analyses of Sequential and Concurrent Product Development Processes*, Kluwer Academic Publications, *Intelligent Knowledge-Based Systems*, Edited by Cornelius T. Leondes, Volume 2 Information Technology, 123-177.
- Tang, P., Bittner, R. 2014. Use of value engineering to develop creative design solutions for marine construction projects. *Pract Period Struct Des Constr*; 19, special issue: Construction Engineering: Leveraging Project and Career Success, 129–36.
- Tohidi, H. 2011. Review the benefits of using value engineering in information technology project management. *Procedia-Computer Science Journal*; 3: 917–24.
- Wao, J.O. 2014. Value engineering methodology to improve building sustainability outcomes. PhD Dissertation, University of Florida, USA.



**SURROGATE MODEL ASSISTED
OPTIMIZATION OF MULTIBAND
ANTENNA**

Mehmet Ali BELEN

Introduction

The significance of antennas in wireless communication is paramount. They play a crucial role in the operation of wireless gadgets, which have gotten progressively smaller and more versatile. The advancement of portable electronics necessitates the incorporation of small, lightweight antennas into radio frequency (RF) packages. With the rapid advancement of wireless communication technology, antennas have emerged as an indispensable component of our civilization, facilitating connectivity with space and playing a pivotal role in electronic realm. The constant advancement of antenna technology is imperative due to the indispensability of personal wireless devices such as mobile phones, Wi-Fi, and laptops in our everyday lives [1].

The inclusion of multi-band antenna designs is crucial because of the wide variety and continuous growth of wireless communication standards [2-3]. These regulations necessitate that antennas encompass many communication frequencies inside a single framework. Multi-band antennas have notable benefits, including the capacity to accommodate many bands, which is essential due to the wide range of frequencies utilised in contemporary wireless communication systems. This functionality is especially advantageous for devices such as multi-band wireless phones that are capable of supporting many networks, enabling the simultaneous transmission of audio, video, and data [4]. The capacity to accommodate several bands on a singular antenna platform significantly boosts the adaptability and efficiency of wireless communication systems.

The design of multi-band antennas is a crucial yet intricate undertaking. With the growing desire for compact and versatile wireless devices, antenna engineers encounter several obstacles in creating antennas that fulfil these changing demands [5]. One such problem is the need to address size limitations and ensure coverage across different frequency bands. Attaining a compact antenna size that can effectively operate throughout the frequency ranges of existing 2G/3G/4G/5G communication protocols, including LTE, GSM, DCS, PCS, UMTS, and WLAN, poses a considerable difficulty. As the frequency bands widen to encompass a broader spectrum, the task of creating antennas that can support these frequencies without growing in size becomes progressively more challenging. (II) Contemporary wireless communication protocols require antennas capable of operating across several frequency bands inside a single platform. The task at hand is to create antennas that are both efficient and flexible, with a small size and low cost. Additionally, it is important to ensure that these antennas have enough capacity to support various frequency bands. The complexity is heightened by the requirement for intricate antenna design with a large number of design options, necessitating the use of time-do-

main electromagnetic techniques and parametric analytic optimisation to obtain enhanced performance. (III) There exists an inherent contradiction between attaining a small antenna size and achieving a wide bandwidth. When the size of the antenna decreases or the frequency decreases, the radiation properties typically worsen. The trade-off between antenna size and bandwidth is a significant challenge in antenna development. The crucial objective is to build small antennas that maintain a wide range of frequencies without compromising on bandwidth. (IV) The design process of multi-band antennas includes multiple geometrical and material characteristics, which are typically subject to limits on their permitted values. These parameters have complex functional interdependencies. Modifying a single design variable can have a negative impact on another, resulting in a decline in performance. This balancing endeavour is similar to seeking a generalized solution in multidimensional solution space. Methods such as genetic algorithms have been utilised to efficiently navigate these intricate interactions.

As it can be seen designing multi-band antennas presents several challenges, in which engineers must create antennas that are efficient, conformable, compact, low-profile, cost-effective, and have sufficient bandwidth to support various bands, while try to answer this problem in a computational efficient manner [6-8].

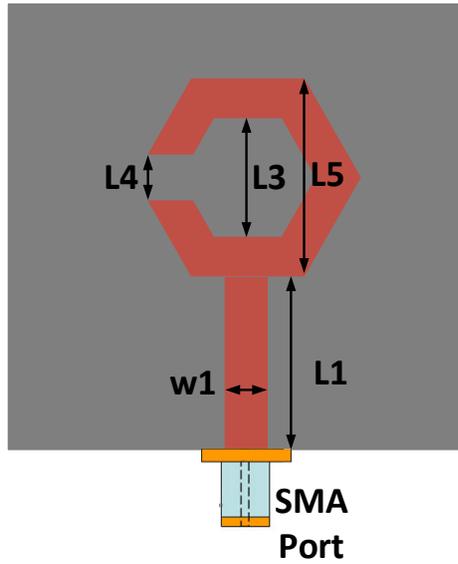
The recent advancements in Machine Learning (ML) algorithms have revolutionized various scientific and engineering domains, providing innovative solutions to complex modeling challenges [9-16]. Particularly in the field of microwave engineering, ML has demonstrated exceptional capabilities in surrogate modeling of components such as antennas [17-20]. Surrogate modeling, essentially a form of approximation modeling, has been a critical tool in microwave engineering for simplifying the design and analysis of complex systems. Traditional methods, while effective, often require extensive computational resources and time. ML algorithms, including neural networks, support vector machines, and decision trees, have emerged as powerful alternatives. These algorithms can learn from data, capturing intricate relationships between design parameters and performance metrics, thus facilitating more efficient and accurate models [21].

In microwave engineering, ML has found applications in various areas. For instance, neural networks have been employed to model complex behaviors in microwave transistors [22-25], providing insights that traditional analytical models struggle to capture. Support vector machines have been used for optimizing the design of frequency selective surfaces, allowing for faster and more efficient design cycles [26]. Decision trees, on the other hand, have aided in the quick classification and analysis of different microwave circuits [27-29].

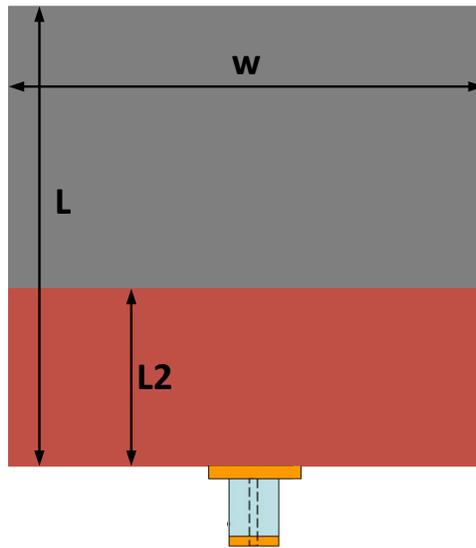
The modeling of multi-band microstrip antennas, in particular, presents a unique challenge due to their multifaceted nature, involving intricate geometrical configurations and diverse material properties. ML algorithms offer a promising solution here. By training on datasets that encompass a wide range of antenna geometrical designs and their respective performance metrics, ML models can effectively predict the behavior of new antenna designs [30-31]. This capability significantly reduces the need for extensive full-wave electromagnetic simulations, which are typically time-consuming and computationally intensive. Moreover, ML-based surrogate models can assist in optimizing antenna designs for specific performance criteria, such as bandwidth, gain, and radiation pattern, by quickly evaluating a large design space. This is especially beneficial in multi-band antenna designs, where trade-offs between different bands must be carefully balanced.

Split Hexagon-Shaped Ring Resonator based Multi-Band Microstrip Antenna

In this work, a split hexagon-shaped ring resonator (SHRR) design presented in Fig. 1 is taken as a study case example of this work. The following specifications should be considered as crucial factors in 3D electromagnetic modelling of the SHRR antenna. (i) The design needs to possess an input impedance of 50Ω . (ii) The length specifications dictate the minimum operating frequency. (iii) The upper working frequency is established by considering the dimensions of the radiating element and the properties of the substrate material, such as its height, thickness, and dielectric constant. Latin Hyper-cube sampling is used for generating 1000 samples to be used as training (80%) and test (20%) with respect to the limitations in Table 1. The EM response of each sample is studied between 1-10 GHz with step size of 0.1 GHz.



(a)



(b)

Fig. 1. Schematic of SHRR Antenna (a) Top, (b) Ground, Layer.
 Table 1. boundaries of SHRR antenna in [mm]. $W=30$, $L= 30$ [mm], $L1=L2$,
 $W1=L4$.

W	30	L2	5-50
W1	1-5	L3	3-10
L	30	L4	0.5-5
L1	5-20	L5	10-30

Data Driven Surrogate Modeling of SHRR Antenna

In this section, series of artificial intelligence regression models that shown great performance in literature is used for modelling of the surrogate of SHRR antenna. Each model undergoes training using k-fold cross validation, with a 4- fold. Additionally, two hundreds (20%) of the entire dataset is withheld as a test (holdout) dataset to evaluate the models' performance in terms of overfitting. Deep Neural Network (DNN) demonstrated superior performance characteristics in hold-out data sets, as measured by the Relative Mean Error (RME) metric. The hyperparameters and results presented in Table 2 were achieved by a straightforward optimization procedure known as grid search. This process was performed on each model, which was implemented in the MATLAB environment. The subsequent phase will involve utilizing the acquired DNN surrogate model to aid in a meta-heuristic optimization procedure for designing a range of antenna models for various operational frequencies.

Table 2. Regression performance of algorithms for the holdout data set obtained after 10 different runs. All not mentioned hyper-parameters are taken as default values in MATLAB environment.

Model and Hyper-Parameter configuration	RME [%]
Multi-Layer Perceptron with single hidden layer consist of 30	10.1±1.1
support Vector Regression Machine with radial kernel function and epsilon of 0.05	7.6 ±0.4
Gaussian process Regression with ard-matern (3/2); Block-coordinate Prediction; and block size of 750	8.1±0.9
Deep Neural network with 4 Hidden layer, Hidden neuron configuration of [128 256 512 1024], batch normalization of 500 and activation function of Relu	4.8±0.3

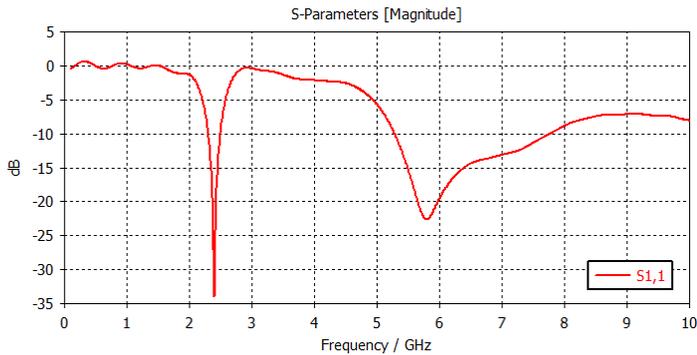
Data Driven Surrogate Model Assisted Optimization of SHRR Antenna for Multiband Applications

Utilizing a data-driven surrogate modeling technique can greatly enhance the computational efficiency of antennas, as opposed to using 3D EM simulators. The optimization of microwave antenna designs is a critical area of research, primarily due to the increasing complexity and performance demands of modern communication systems [32-36]. Metaheuristic optimization algorithms have emerged as pivotal tools in addressing these design challenges [37-39]. These algorithms, characterized by their ability to efficiently navigate large, complex search spaces, offer several advantages over traditional optimization methods. Metaheuristic algorithms are inherently flexible, capable of adapting to various types of antenna design problems without the need for extensive modifications. This adaptability is crucial in microwave antenna design, where the optimization landscape can vary significantly based on factors like frequency range, bandwidth, and physical constraints. In this context, employing meta-heuristic opti-

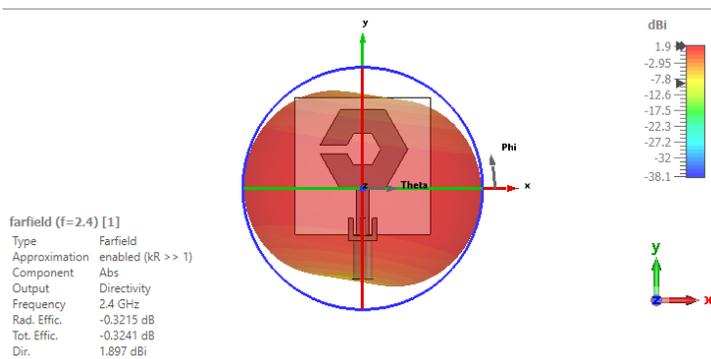
mization algorithms proves to be a feasible solution for optimizing of multi-band antenna designs. Despite the existence of various high-performance optimization approaches that are based on different species and their hunting, mating, or other behaviors, the impact of the convergence speed of these algorithms can be disregarded due to the substantial acceleration provided by surrogate modeling. Particle Swarm Optimization (PSO) [40] is employed to do the optimal design parameter search using the given cost function. Equation (1),

$$x^* = \arg \min_x [\bar{u} \quad \{|S_{11}(x, f_r)|\}] \quad (1)$$

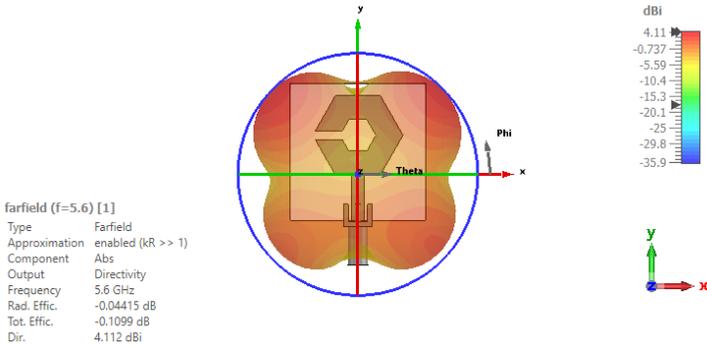
x is the input vector of variables, $[f_r]$ targeted operating frequency. The study case target criteria's and its optimally obtained geometrical design variables are as follows: Antenna operates 2.4 GHz. The optimally selected design variables are $[W1 \ L1 \ L3 \ L5] = [2.8 \ 9.9 \ 6.9 \ 17.3]$ all in [mm]. The 3D EM simulated results and the surrogate model response of optimal design are presented in Fig. 2. The figure demonstrates that the proposed surrogate modelling approach successfully identifies the desired geometrical design factors to produce the desired design response. Furthermore, the obtained results closely align with the results obtained from 3D EM simulations.



(a)



(b)



(c)

Fig. 2. 3D EM Simulated responses of optimal designed obtained from DNN Assisted optimization (a) Scattering parameter; (b) Radiation pattern @ 2.4 GHz; (c) Radiation pattern @ 5.6 GHz.

Conclusion

In this study, we present an advanced methodology for optimizing the design of a SHRR based microstrip antenna utilizing data-driven surrogate modeling techniques, renowned for their computational efficiency. This approach leverages data samples derived from 3D electromagnetic (EM) simulations to establish a surrogate model that accurately represents the antenna design challenge at hand. A comprehensive evaluation of various regression algorithms revealed that Deep Neural Networks (DNN) offered the most effective solution for this specific design optimization. To validate our proposed method, we conducted three distinct case studies, treating each as an optimization problem to be resolved through our surrogate model. The outcomes of these cases were then meticulously compared with results from full-wave 3D EM simulations. The findings clearly demonstrate that our surrogate modeling technique not only successfully identifies the necessary geometrical design parameters to achieve the desired antenna response but also ensures a high degree of congruence with the results from detailed 3D EM simulations.

Acknowledgment

This work has been supported by Project 121N412 of TUBITAK (Scientific and Technological Research Council of Turkey). We would like to express our special thanks of gratitude to the Aktif Nesor Elektronik and DataRobot, for providing researcher licenses for CST and DataRobot.

REFERENCES

- [1] Venu, Dr Nookala, A. Arun Kumar, and Karthik Kumar Vaigandla. "Review of Internet of Things (IoT) for Future Generation Wireless Communications." *International Journal for Modern Trends in Science and Technology* 8, no. 03 (2022): 01-08.
- [2] Ramahatla, Kebonyethebe, Modisa Mosalaosi, Abid Yahya, and Bokamoso Basutli. "Multiband reconfigurable antennas for 5G wireless and CubeSat applications: A review." *IEEE Access* 10 (2022): 40910-40931.
- [3] Mietzner, Jan, Robert Schober, Lutz Lampe, Wolfgang H. Gerstacker, and Peter A. Hoehner. "Multiple-antenna techniques for wireless communications-a comprehensive literature survey." *IEEE communications surveys & tutorials* 11, no. 2 (2009): 87-105.
- [4] Khalilabadi, Amirreza Jalali, and Ata Zadehgo. "Multiband antenna for wireless applications including GSM/UMTS/LTE and 5G bands." In *2018 International Applied Computational Electromagnetics Society Symposium (ACES)*, pp. 1-2. IEEE, 2018.
- [5] Boukarkar, Abdelheq, Xian Qi Lin, Yuan Jiang, and Yi Qiang Yu. "Miniaturized single-feed multiband patch antennas." *IEEE Transactions on Antennas and Propagation* 65, no. 2 (2016): 850-854.
- [6] Kannadhasan, S., R. Nagarajan, and Kanagaraj Venusamy. "Performance, Metrics, and Challenges of Multiband Antenna for Wireless Communication." In *2022 6th International Conference on Trends in Electronics and Informatics (ICOEI)*, pp. 478-481. IEEE, 2022.
- [7] Jamil, Atif, Mohd Zuki Yusoff, and Noorhana Yahya. "Current issues and challenges of MIMO antenna designs." In *2010 International Conference on Intelligent and Advanced Systems*, pp. 1-5. IEEE, 2010.
- [8] Kurniawan, Adit, and Salik Mukhlisin. "Wideband and multiband antenna design and fabrication for modern wireless communications systems." *Journal of ICT Research and Applications* 7, no. 2 (2013): 151-163.
- [9] Reich, Yoram. "Machine learning techniques for civil engineering problems." *Computer-Aided Civil and Infrastructure Engineering* 12, no. 4 (1997): 295-310.
- [10] Yurt, Reyhan, Hamid Torpi, Ahmet Kizilay, Slawomir Koziel, Anna Pietrenko-Dabrowska, and Peyman Mahouti. "Buried object characterization by data-driven surrogates and regression-enabled hyperbolic signature extraction." *Scientific Reports* 13, no. 1 (2023): 5717.
- [11] Yurt, Reyhan, Hamid Torpi, Peyman Mahouti, Ahmet Kizilay, and Slawomir Koziel. "Buried object characterization using ground penetrating radar assisted by data-driven surrogate-models." *IEEE Access* 11 (2023): 13309-13323.
- [12] Kuwajima, Hiroshi, Hirotooshi Yasuoka, and Toshihiro Nakae. "Engineering problems in machine learning systems." *Machine Learning* 109, no. 5 (2020): 1103-1126.

- [13] Uluslu, Ahmet. "Application of Artificial Neural Network Base Enhanced MLP Model for Scattering Parameter Prediction of Dual-band Helical Antenna." *Applied Computational Electromagnetics Society Journal* 38, no. 5 (2023).
- [14] Panchal, Jitesh H., Mark Fuge, Ying Liu, Samy Missoum, and Conrad Tucker, eds. "Machine learning for engineering design." *Journal of Mechanical Design* 141, no. 11 (2019): 110301.
- [15] AKYOL, Habil Akansel, and Ahmet KIZILAY. "Design optimization of railgun's electromagnetic force using surrogate modelling." *Sigma: Journal of Engineering & Natural Sciences/Mühendislik ve Fen Bilimleri Dergisi* 41, no. 5 (2023).
- [16] Lu, Stephen CY. "Machine learning approaches to knowledge synthesis and integration tasks for advanced engineering automation." *Computers in Industry* 15, no. 1-2 (1990): 105-120.
- [17] Piltan, Onur Can, Ahmet Kizilay, Mehmet A. Belen, and Peyman Mahouti. "Data driven surrogate modeling of horn antennas for optimal determination of radiation pattern and size using deep learning." *Microwave and Optical Technology Letters* (2023).
- [18] Mahouti, Peyman, Ahmet Kızılray, Ozlem Tari, Aysu Belen, and Mehmet A. Belen. "Design optimization of ultra wide band vivaldi antenna using artificial intelligence." In *2021 International Applied Computational Electromagnetics Society Symposium (ACES)*, pp. 1-4. IEEE, 2021.
- [19] Khan, Mohammad Monirujjaman, Sazzad Hossain, Puezia Mozumdar, Shamima Akter, and Ratil H. Ashique. "A review on machine learning and deep learning for various antenna design applications." *Heliyon* 8, no. 4 (2022).
- [20] Patel, Shobhit K., Jaymit Surve, Vijay Katkar, and Juveriya Parmar. "Machine learning assisted metamaterial-based reconfigurable antenna for low-cost portable electronic devices." *Scientific Reports* 12, no. 1 (2022): 12354.
- [21] Mahouti, Peyman. "Design optimization of a pattern reconfigurable microstrip antenna using differential evolution and 3D EM simulation-based neural network model." *International Journal of RF and Microwave Computer-Aided Engineering* 29, no. 8 (2019): e21796.
- [22] Mahouti, Peyman, Filiz Güneş, Salih Demirel, Ahmet Uluslu, and Mehmet Ali Belen. "Efficient scattering parameter modeling of a microwave transistor using generalized regression neural network." In *2014 20th International Conference on Microwaves, Radar and Wireless Communications (MIKON)*, pp. 1-4. IEEE, 2014.
- [23] Calik, Nurullah, Filiz Güneş, Slawomir Koziel, Anna Pietrenko-Dabrowska, Mehmet A. Belen, and Peyman Mahouti. "Deep-learning-based precise characterization of microwave transistors using fully-automated regression surrogates." *Scientific Reports* 13, no. 1 (2023): 1445.
- [24] Şenel, Bilge, and Fatih Ahmet Şenel. «Novel neural network optimization approach for modeling scattering and noise parameters of microwave transistor.» *International Journal of Numerical Modelling: Electronic Networks, Devices and Fields* 35, no. 1 (2022): e2930.

- [25] Mishra, Ashutosh, Samriddhi Raut, Khushwant Sehra, Raghvendra Pratap Singh, Shweta Wadhwa, Poonam Kasturi, Geetika Jain Saxena, and Manoj Saxena. "Multilayer perceptron-random forest based hybrid machine learning-neural network model for GaN high electron mobility transistor's parameter estimations." *International Journal of RF and Microwave Computer-Aided Engineering* 32, no. 7 (2022): e23191.
- [26] Prado, Daniel R., Jesus A. Lopez-Fernandez, Guillermo Barquero, Manuel Arrebola, and Fernando Las-Heras. "Fast and accurate modeling of dual-polarized reflectarray unit cells using support vector machines." *IEEE Transactions on Antennas and Propagation* 66, no. 3 (2018): 1258-1270.
- [27] Fontoura, Leidiane CMM, Hertz Wilton De Castro Lins, Arthur S. Bertuleza, Adaildo Gomes D'assunção, and Alfredo Gomes Neto. "Synthesis of multiband frequency selective surfaces using machine learning with the decision tree algorithm." *IEEE Access* 9 (2021): 85785-85794.
- [28] Pavithran, Shilpa, Sanoj Viswasom, and J. Asha. "Designing of a 5G multiband antenna using decision tree and random forest regression models." In *2021 8th International Conference on Signal Processing and Integrated Networks (SPIN)*, pp. 626-631. IEEE, 2021.
- [29] Kalayci, Hakan, Umut Engin Ayten, and Peyman Mahouti. "Ensemble-based surrogate modeling of microwave antennas using XGBoost algorithm." *International Journal of Numerical Modelling: Electronic Networks, Devices and Fields* 35, no. 2 (2022): e2950.
- [30] Wu, Qi, Yi Cao, Haiming Wang, and Wei Hong. "Machine-learning-assisted optimization and its application to antenna designs: Opportunities and challenges." *China Communications* 17, no. 4 (2020): 152-164.
- [31] Sarker, Nayan, Prajoy Podder, M. Rubaiyat Hossain Mondal, Sakib Shahriar Shafin, and Joarder Kamruzzaman. "Applications of Machine Learning and Deep Learning in Antenna Design, Optimization and Selection: A Review." *IEEE Access* (2023).
- [32] Uluslu, Ahmet. "Fitting nonlinear mathematical models to the cost function of the quadrafilar helix antenna optimization problem." *Analog Integrated Circuits and Signal Processing* 115, no. 3 (2023): 307-318.
- [33] Uluslu, Ahmet. "Chameleon Swarm Algorithm assisted optimization of U-slot patch antenna for quad-band applications." *IEEE Access* 10 (2022): 74152-74163.
- [34] Güneş, Filiz, Ahmet Uluslu, and Peyman Mahouti. "Pareto optimal characterization of a microwave transistor." *IEEE Access* 8 (2020): 47900-47913.
- [35] Mechenova, V. A., and V. V. Yakovlev. "Efficiency optimization for systems and components in microwave power engineering." *Journal of Microwave Power and Electromagnetic Energy* 39, no. 1 (2004): 15-30.
- [36] Yu, Yang, Zhen Zhang, Qingsha S. Cheng, Bo Liu, Yi Wang, Cheng Guo, and Terry Tao Ye. "State-of-the-art: AI-assisted surrogate modeling and optimization for microwave filters." *IEEE Transactions on Microwave Theory and Techniques* 70, no. 11 (2022): 4635-4651.

- [37] Abualigah, Laith, Mohamed Abd Elaziz, Ahmad M. Khasawneh, Mohammad Alshinwan, Rehab Ali Ibrahim, Mohammed AA Al-Qaness, Seyedali Mirjalili, Putra Sumari, and Amir H. Gandomi. "Meta-heuristic optimization algorithms for solving real-world mechanical engineering design problems: a comprehensive survey, applications, comparative analysis, and results." *Neural Computing and Applications* (2022): 1-30.
- [38] Toktas, Abdurrahim. "Multi-objective design of multilayer microwave dielectric filters using artificial bee colony algorithm." *Nature-Inspired Metaheuristic Algorithms for Engineering Optimization Applications* (2021): 357-372.
- [39] Güneş, Filiz, Salih Demirel, and Selahattin Nesil. "Design Optimization of LNAs and Reflectarray Antennas Using the Full-Wave Simulation-Based Artificial Intelligence Models with the Novel Metaheuristic Algorithms." In *Simulation-Driven Modeling and Optimization: ASDOM, Reykjavik, August 2014*, pp. 261-298. Springer International Publishing, 2016.
- [40] Shi, Yuhui. "Particle swarm optimization." *IEEE connections* 2, no. 1 (2004): 8-13.